UNIVERSITY OF CALIFORNIA,
IRVINE

3D-In-Vivo-like Tissues with Bioelectronic for Studying Disease Progression and Therapeutics In-Vitro

DISSERTATION

submitted in partial satisfaction of the requirements
for the degree of

DOCTOR OF PHILOSOPHY

in Electrical Engineering

by

Sahar Najafikhoshnoo

Dissertation Committee:
Assistant Professor Rahim Esfandyarpour, Chair
Assistant Professor Quinton Smith
Assistant Professor Hamidreza Aghasi

2024

DEDICATION

To

My family and friends

in recognition of their unconditional love and unending support.

Table of Contents

LIST OF FIGURES

ACKNOWLEDGMENTS

I wish to extend my sincerest thanks and recognition to the chair of the committee, Prof. Rahim Esfandyarpour, whose constant encouragement inspired me to be innovative and aimed at evoking my best performance. His unwavering support, mentorship, and continuous assistance were crucial to the completion of this dissertation. The time spent in his laboratory was educational, teaching me numerous facets of scientific inquiry, knowledge that will surely benefit my future endeavors.

My deepest appreciation also goes to my committee members, Prof. Quinton Smith, and Prof. Hamidreza Aghasi, for their invaluable insights regarding my dissertation and research projects. Furthermore, I am grateful to my peers at the Integrated Nano Bio Electronics Innovation (INBE) lab and Smith lab, especially Dr. Prativa Das, Dr. Mozhgan Keshavarz, and fellow PhD students, Jorge Tavares-Negrete, and Xiaochang Pei, for their essential research advice and assistance in solving issues during experimental work. A special thanks to the Department of Electrical Engineering and Computer Science at UCI for awarding me the initial fellowship funding, which played a significant role in my success on this journey.

I gratefully acknowledge the use of BioRender.com for the creation and preparation of some of the figures presented in this thesis. Portions of Chapter 3 are an adaptation of the material as it appears in "An in-vivo-mimicking 3D lung cancer-on-a-chip model to study the effect of external stimulus on the progress and inhibition of cancer metastasis" in Bioprinting, used with permission from Elsevier B.V. The co-authors listed in this publication are Prativa Das, Jorge A. Tavares-Negrete, Qian Yi, and

Rahim Esfandyarpour. Rahim Esfandyarpour directed and supervised research which forms the basis for the dissertation.

Lastly, this research was made possible thanks to the startup funds allocated to Prof. Rahim Esfandyarpour by the Henry Samueli School of Engineering and the Electrical Engineering department at the University of California, Irvine.

VITA

Sahar Najafikhoshnoo

Education

2014-2019 B.S. in Electrical Engineering,
University of Tehran

2020-2023 M.S. in Electrical Engineering,
University of California, Irvine

2024 Ph.D. Electrical Engineering,
University of California, Irvine

Selected Peer-Reviewed Journal Publications (* co-first author)

Najafikhoshnoo, S., Kim, T., Tavares-Negrete, J., Pei, X., Das, P., Lee, S., Rajendran, J., and Esfandyarpour, R., "A 3D-nanomaterials printed wearable, battery-free, biocompatible, flexible, and wireless pH sensor system for real-time health monitoring" Adv. Mater. Technol. 2023, 8, 2201655.

Das, P.*, **Najafikhoshnoo, S.***, Tavares, A. J., Yi, Q., Esfandyarpour, R., "An in-vivo-mimicking 3D lung cancer-on-a-chip model to study the effect of external stimulus on the progress and inhibition of cancer metastasis" Bioprinting, 28, e00243.

Yi, Q., **Najafikhoshnoo, S.**, Das, P., Noh, S., Hoang, E., Kim, T., Esfandyarpour, R., "All-3D-printed, flexible, and hybrid wearable bioelectronic tactile sensors using biocompatible nanocomposites for health monitoring," Adv. Mater. Technol. 2021, 2101034.

Das, P., Tavares, A. J., **Najafikhoshnoo, S.**, Esfandyarpour, R., "Recent advances in Lung on a chip to model respiratory diseases," Bio-des. Manuf. 6, 563–585 (2023).

Tavares, A. J.,Babayigit, C., **Najafikhoshnoo, S.**, Boyraz, O., Esfandyarpour, R., "A novel 3D-bioprinting technology of orderly extruded multi-materials via photopolymerization" Adv. Mater. Technol., 8: 2201926.

Under Preparation Publications

Najafikhoshnoo, S., Tavares-Negrete, J., Das, P., Keshavarz, M., Smith, Q., and Esfandyarpour, R.," Functional Colon Reconstruction Using 3D-Bioprinted Native-Like Tissue Architecture for Disease Modeling" To be submitted.

ABSTRACT OF THE DISSERTATION

3D-In-Vivo-like Tissues with Bioelectronic for Studying Disease Progression and Therapeutics In-Vitro

by

Sahar Najafikhoshnoo

Doctor of Philosophy in Electrical Engineering

University of California, Irvine, 2024

Assistant Professor Rahim Esfandyarpour, Chair

This dissertation marks a significant advancement in the realm of in vitro disease modeling and drug screening, addressing the critical gap in existing methodologies that fail to replicate the refined microenvironment of human tissues with high fidelity. By addressing the critical limitations of traditional two-dimensional cultures and simpler 3D constructs, our work introduces novel, physiologically accurate models that replicate the complex microenvironments of organ tissues. The focus on developing organ-specific 3D bioprinted models for colorectal and lung cancer reflects a targeted approach to tackling two of the most challenging forms of cancer, highlighting the urgent need for more sophisticated and accurate disease models.

Chapter 2 reveals a pioneering functional, three-dimensional colon model, utilizing the cutting-edge Freeform Reversible Embedding of Suspended Hydrogels (FRESH) 3D bioprinting technology. This innovation represents magnificent improvements in simulating the colon's mechanical, physical, and biological complexities. Our dual-layered construct not only matches the 3D luminal curvature and macrostructures of native colon tissue but also replicates the subepithelial and epithelial interaction through co-culture of 3T3 fibroblast cells with Caco-2 epithelial cells in 3D tissue geometry. Our in-vivo-mimicking colon model facilitates the formation of mini-colonic crypt structures, increasing the surface area, and therefore improving the absorption functionality. This mirrors the colon's natural architecture and enhances functionality in vitro. This model serves as a highly physiologically relevant platform, enabling an in-depth exploration of colorectal cancer mechanisms and the evaluation of therapeutic responses. Through comprehensive and novel drug efficacy analyses focusing on colorectal cancer treatments, we have demonstrated the model's unprecedented performance, showcasing its significant superiority in drug response assessments over traditional 2D cultures and other existing 3D constructs.

Chapter 3 introduces the in-vivo mimicking 3D-lung-cancer-on-a-chip (IVM3DLCOC) model, developed and characterized to more precisely represent lung pathogenesis in vitro. The model innovatively co-cultures A549 lung cancer cells with human lung fibroblasts within 3D hydrogels, engineered to mirror the lung's extracellular matrix. This setup replicates essential mechanical and biological cues for cell adhesion, proliferation, and an accurate study of disease progression, particularly lung cancer metastasis. The inclusion of fluidic channels intersecting air channels via

a porous membrane atop the lung epithelial cells establishes an air-liquid interface, simulating the lung's inhalation and exhalation cycles and reproducing the dynamic physiological microenvironment. The efficacy of this model was underscored through studies examining the impact of cigarette smoke extract (CSE), preserving metastatic characteristics and revealing translational properties crucial for understanding disease progression and the validation of drug efficacy.

Both models showcase a transformative shift in the landscape of in vitro disease modeling and drug screening, offering a more accurate and physiologically relevant lens through which to view the complexities of cancer mechanisms and the development of effective therapies. This work not only challenges the limitations of traditional methodologies but also significantly contributes to the fields of biomedical engineering and personalized medicine. It lays the groundwork for future innovations in cancer research, with the potential to dramatically enhance the precision and effectiveness of cancer treatments.

Chapter 1

1.1 Introduction

The advancement of in vitro tissue and disease models marks a significant milestone in the exploration to unravel the complexities of disease mechanisms and progression[1]. These bioartificial constructs are designed to replicate the structural and functional complexities of human tissues and organs, thereby providing an invaluable framework for conducting fundamental research[2]. Such research endeavors are aimed at shedding light on the physiological and molecular difficulties that govern disease initiation and development[3], [4]. In doing so, these models not only deepen our understanding of disease dynamics but also pave the way for the innovation of novel diagnostic and therapeutic modalities.

There is a significant shift towards the adoption of human disease models. This shift is underscored by the challenges confronting the drug development landscape, characterized by high failure rates. The urgency for this transition is further magnified by the financial landscape of pharmaceutical research and development. The development of new pharmaceutical compounds is a costly endeavor, marked by significant challenges in both time and financial investment[5], [6]. The journey from conception to Food & Drug Administration (FDA) approval is not only lengthy, spanning 10 to 15 years, but also excessively expensive[7]. This process is jammed with inefficiencies, largely due to the limitations of current preclinical models that frequently fail to predict clinical responses accurately. As a result, around ninety

percent of the drug candidates fail in clinical trials, primarily due to toxicity issues, leading to post-marketing withdrawals or limited usage owing to adverse drug effects[8], [9]. The scenario compellingly advocates for a strategic pivot towards more predictive human-based models, which promise a more reliable foundation for drug discovery and development.

1.1.1 Introduction to pre-clinical models

Preclinical studies, which employ a variety of models like in vitro, in vivo, ex vivo, and in silico, are foundational in assessing a drug candidate's safety and biological efficacy before human testing. In this context, in vitro assays serve as a vital initial step. They offer a simple, quick, and cost-effective method to evaluate basic drug effects[10]. The earliest in vitro studies were growing cell lines, special types of cells which will continually divide in a process called proliferation, on 2-dimensional (2D) materials such as plastic or glass [11]

Cell lines have the capacity to proliferate indefinitely and to be propagated for long periods of time. They are amenable for high throughput screenings, and panels of cell lines with defined mutations are available for controlled in vitro experiments, such as the ones from the National Cancer Institute [12]. Cell lines, however, have intrinsic limitations. First, they have to be adapted to specific culture conditions and this favors clone selection thus crashing on cell heterogeneity. cell lines do not recapitulate certain in vivo conditions such as cell–cell and cell–matrix interactions. There is no tumor stroma involved and, as a consequence, cell lines lose the signals coming from their niches. Furthermore, cells in 2D are constantly exposed to high

levels of nutrients and oxygen, parameters that, in vivo, are subject to variability imposed by the 3D architecture [13], [14], [15]. This approach is still the standard procedure for in vitro cell culture, however the environment of 2D culture flasks and plates cannot replicate any of the 3-dimensional (3D) mechanical and chemical cues necessary for organogenesis. Furthermore, the nature of these 2D surfaces will alter the cells' morphology and behavior. Studies have demonstrated that these surfaces induce morphological changes such as a flattened shape and forced apical-basal polarity in cells, as well as loss of differentiation. These alterations highlight the gap between in vitro conditions and the complex reality of living organisms.

The next crucial bridge between in vitro studies and human clinical trials are animal preclinical studies, where different species of animals are used to provide a model of how the new therapeutic compound may impact a human subject [16]. Traditionally, the most commonly used animal models are rodents, as they mirror human architecture in many ways. Animal models mimic the physiological, metabolic, and cellular interactions of human bodies more closely than 2D cultures, allowing for a more comprehensive assessment of a drug's efficacy and safety. Through these models, researchers can study systemic effects, investigate disease mechanisms in a whole-body context, and evaluate the pharmacokinetics and pharmacodynamics of new therapeutic agents. However, In vivo animal models are limited due to many reasons including being expensive, time-consuming, variability among animal responses which can lead to reproducibility issues, or ethically controversial. Ethical concerns arise regarding the welfare of animals used in research, leading to strict

regulatory guidelines and ethical debates [17]. Furthermore, the main obstacle of in vivo animal models is the imprecise representation of human responses due to their differential pathophysiological responses [18]. Despite these challenges, animal models remain indispensable in certain areas of research, particularly where alternative methods are yet to fully replicate the complexity of living organisms.

Efforts to develop and refine alternative methods, like in-vivo-mimicking organ models and computational models, are ongoing and aim to reduce the reliance on animal models. These alternatives seek to address both ethical concerns and biological limitations, offering more accurate models for human diseases [19]

1.1.2 Introduction to Tissue Engineering for In Vitro Models

Within the realm of tissue engineering (TE), a synergistic fusion of engineering and life sciences methodologies are employed to fabricate bioartificial analogs of human organs and tissues. This interdisciplinary approach facilitates the application of these engineered tissues across a spectrum of fields, including pharmaceutical development, diagnostic studies, regenerative medicine, and foundational biological research. Central to this application is the potential of these bioartificial constructs to provide critical insights into in vivo cellular functionalities, and to demonstrate the underlying mechanisms that govern disease initiation, and progression, thereby advancing scientific understanding and therapeutic interventions [20]. To construct functional models of organs, careful selection of the cells, methods, and materials is essential, aiming to closely mimic their natural behavior and environment. In practical terms, the extent to which in vivo conditions are replicated in vitro typically represents

a compromise between achieving accuracy, managing complexity, and maintaining feasibility. In the complex three-dimensional (3D) environment found in vivo, cells are organized, facilitating interactions among diverse cell types and between cells and the extracellular matrix [21], [22]. This matrix's composition is notably dynamic, varying in response to the specific tissue type, its maturation state, and prevailing health conditions. Within such a framework, three-dimensional (3D) in vitro models present a more authentic replication of tissue or organ structure and function compared to traditional two-dimensional (2D) models. Furthermore, to address the limitations inherent in current drug-screening methods and to diminish animal usage, extensive research is being conducted on three-dimensional (3D) models, aiming to enhance their reliability and sophistication [23], [24]. Distinct from animal models, 3D in vitro systems offer the capability to independently identify and modulate cellular and molecular factors implicated in disease initiation and progression. This allows for detailed exploration of the role of each factor in specific disease development, thereby revolutionizing the study of tissue physiology and pathophysiology. The integration of these models into biomedical research promises multiple benefits, including reduced reliance on animals, overcoming the constraints of traditional models (such as animal and 2D cell cultures), and generating more reproducible data. This is achieved through precise control over experimental parameters, which also leads to cost and time efficiencies.

1.1.2.1 Approaches to 3D Tissue Engineering

Current strategies in the field of tissue engineering for in vitro 3D models

encompass various techniques. These methods notably include: i) the seeding of cells onto prefabricated, porous, and biodegradable scaffolds, ii) the process of decellularizing and then recellularizing pre-existing extracellular matrix (ECM), and iii) the encapsulation of cells within a supportive hydrogel matrix [23], [25], [26]. Among these approaches, the utilization of biopolymer materials as scaffolds for cell loading is particularly prevalent. This method involves the development and fabrication of biopolymer structures to emulate the native ECM, which is the natural environment of cells.

Another layer of complexity that characterizes the tissues and organs of higher organisms in vitro is their geometry and macro-structure. Tissue geometry and curvature influence cell behavior, tissue formation and function, and therefore the (patho)physiological relevance of in vitro models [27]. For instance, the intestinal crypts and alveolar sacs contribute significantly to an expansive epithelial surface area, thus determining the absorption rates of nutrients and gases. Replicating these features precisely in vitro presents a challenge due to the complexities involved in controlling the formation, dimensions, and shapes of geometric structures relevant to tissue, which frequently leads to substantial variability in models and constrained biomimetic fidelity[28]. There are several methods that have been incorporated to enable fabrication of complex geometry of organ models.

1.1.2.2 3D Printing and bioprinting

Additive manufacturing, often referred to as 3D printing, is characterized by the precise, computer-controlled deposition of materials in a layer-by-layer approach to construct assembled structures[29]. This technology, first developed in 1986 by C. Hull

through a process called "stereolithography," which used layers of ultraviolet (UV) curable resin, has significantly impacted various fields including engineering, manufacturing, art, education, and medicine [30]. It democratizes precision manufacturing, enabling users with basic knowledge of computer-aided design (CAD) to prototype and manufacture objects with diverse material properties at a lower cost and with greater ease. The CAD program allows the user to design an object digitally, which is then translated into layer-by-layer instructions for the printer. These instructions, formatted in standard g-code (ISO 6983), guide the printer's 4-axis movements (x, y, z, and extrusion) to create the object. Advanced systems monitor both the material and the object during printing, making real-time adjustments to ensure successful outcomes.

In tissue engineering, additive manufacturing first found application in creating synthetic scaffolds for cell seeding [31]. However, this approach has limitations in terms of homogenous cell distribution and precise cellular positioning. To address this, researchers have developed 3D bioprinting, a process that concurrently places biological material and scaffold material in a layer-by-layer fashion to create 3D structures. Tissue engineers must carefully select the bioprinting method and bioink to optimize cell survival and spatial control. Current bioprinting techniques include inkjet, extrusion, and laser-assisted bioprinting, each with its unique advantages, limitations, and application based on the material properties and the forces applied to the cells [32], [33], [34].

Inkjet bioprinters excel in printing low viscosity materials and precise cell patterning, although they often struggle with mechanical properties and z-axis

resolution due to the viscosity constraints of the hydrogels [35]. Extrusion bioprinters, suitable for large 3D tissues, face challenges in cell viability due to shear forces [36]. Laser-assisted bioprinting, free from nozzle constraints, is ideal for shear-sensitive cells but is limited in resolution and often cost-prohibitive[37].

The evolution of 3D bioprinting includes initial studies focused on biocompatible scaffold printing, followed by scaffold-free cell aggregate deposition, mirroring morphogenesis. Current extrusion bioprinting techniques can handle single cells, aggregates, organoids, and cell strands with various hydrogels [38], [39]. The balance in extrusion bioprinting lies in selecting a hydrogel that is viscous enough for high-resolution printing yet gentle on cell viability. The bioink flow depends on the hydrogels rheological properties and dispensing parameters, including nozzle diameter, height, printhead speed, flow rate, and substrate adhesion[40].

Advanced extrusion bioprinters, like those developed by S. Shrike's group, use a range of materials from hydrogels to synthetic polymers and can create complex 3D tissues like trachea and lung [41], [42]. J. Lewis' group leads in developing complex structures using Pluronics as sacrificial materials for creating perfusable channels. This approach, while not incorporating cells into the 3D matrix, has significant implications for tissue engineering, though it is more time-consuming and lower in throughput compared to other bioprinting methods[43], [44]. Lee et al. demonstrated successful 3D printing of five components of the human heart spanning capillary to full-organ scale, which they validated for tissue and organ function, printing collagen using freeform reversible embedding of suspended hydrogels (FRESH) method [45]. Several organs such as heart, trachea, lung have been 3D printed in different scales to study

tissue maturation and different disease progression[41], [42], [45]. However, there is more room to study different organs and improve the printing scale to be able to print all organs in full size and enable other mechanical cues and functionality of each organ.

1.1.2.3 Organ on a chip: Bridging the Gap in In Vitro Models

The inception of organ-on-a-chip technology represents a paradigm shift in tissue engineering, marking a pivotal advancement beyond conventional in vitro cell culture models. This innovative approach harnesses the principles of micro-engineering, microfluidics, and biomimetics to create microenvironments that closely mimic the physiological and mechanical properties of living organs. By accurately replicating the microarchitecture, extracellular environments, and the cell-cell interactions characteristic of human organs—all within a compact, chip-based platform—organ-on-a-chip technology offers a more refined and physiologically relevant tool for exploring the complexities of both healthy and diseased organ states.

Transitioning from the broader context of tissue engineering, where the focus has been on overcoming the limitations of traditional 2D and 3D models, organ-on-a-chip technology emerges as a critical evolution. It directly addresses the urgent need for models that not only embody the structural and functional complexity of human tissues but also provide dynamic control over the biochemical and mechanical environment. Such capabilities are instrumental for in-depth studies of disease mechanisms, drug responses, and even the progression of complex pathological conditions over time.

In the realm of pharmaceutical research and drug development, the promise of

organ-on-a-chip technology is particularly compelling. The conventional pathway for drug development, as outlined by regulatory agencies like the U.S. Food & Drug Administration (FDA), involves a series of rigorous steps, from initial laboratory research to extensive clinical trials before a drug can be deemed safe and effective for market release. However, this process is lengthy, costly, and jammed with high rates of failure, often due to unforeseen toxicological issues that emerge during clinical trials. Such setbacks underscore the limitations of existing preclinical models, including animal studies and traditional in vitro assays, which frequently fall short in accurately predicting human responses.

Organ-on-a-chip devices, by virtue of their design, offer a more reliable and ethically sound alternative. These systems enable the precise simulation of organ-specific functions and physiological responses within a controlled microfluidic environment. The result is an enhanced capability for assessing drug toxicity and efficacy with a level of detail and accuracy that was previously unattainable. For instance, liver and kidney chips can provide invaluable insights into a drug's metabolism and clearance, while lung, heart, or bone marrow chips can reveal potential toxicities and therapeutic effects with remarkable specificity.

The strategic development and application of organ-on-a-chip technology is poised to revolutionize the drug development process. By offering a means to conduct more predictive toxicity screenings and efficacy assessments, these devices have the potential to significantly streamline the development pipeline, reducing both the time and cost associated with bringing new therapeutic agents to market. Furthermore, by diminishing the reliance on animal testing, organ-on-a-chip technology aligns with a

growing ethical imperative for more humane research methodologies.

As research continues to expand the capabilities and applications of organ-on-a-chip technology, the potential benefits for drug development, disease modeling, and personalized medicine become increasingly evident. This technology stands as a testament to the power of interdisciplinary collaboration, bridging the gap between engineering, biology, and medicine to forge new pathways in understanding and treating human diseases.

1.2 Organization and content

This thesis comprises two main chapters (chapters 2 and 3), each presenting a distinct research project. These chapters can be read independently. Each chapter begins with an 'introduction' that emphasizes the specific problem, its scientific and practical importance, and includes an overview of relevant literature. Certain terms are shortened for simplicity and are explained upon their first use. Following the introduction, the 'results' section shares crucial experimental outcomes. This is succeeded by a 'discussion' that deliberates the importance and significance of the results and the potential for future research. Next, the 'Materials and Methods' section details the experimental process. Key results from chapters 2 and 3 are summarized in the subsequent paragraphs.

Chapter 2: Functional Colon Reconstruction Using 3D-Bioprinted Native-Like Tissue Architecture for Disease Modeling.

In addressing the critical need for more accurate disease models and drug screening platforms, our research introduces a pioneering three-dimensional colon

model employing the innovative Freeform Reversible Embedding of Suspended Hydrogels (FRESH) 3D bioprinting technology. Traditional experimental models, including in vivo animal models, in vitro 2D and 3D cultures, and bioengineered systems, have played crucial roles in understanding disease mechanisms and evaluating therapeutic responses. However, these models often fall short in accurately replicating the complex microenvironment of human tissues, limiting their effectiveness in predicting drug efficacy and toxicity. Our study aims to bridge this gap by developing a functional, three-dimensional colon model that offers an unmatched level of fidelity in simulating the mechanical, physical, and biological properties of the human colon.

This novel colon model for the first time features a sophisticated dual-layered construct that replicates the intricate architecture of the human colon, including 3D luminal curvature and native-like tissue macrostructures. This design not only mirrors the colon's natural architecture but also provides a physiologically relevant platform for the in-depth exploration of colorectal cancer mechanisms and the evaluation of therapeutic responses. By integrating this model into our research, we have conducted extensive drug efficacy analyses, particularly focusing on colorectal cancer treatments. The results underscore the exceptional performance of this model in drug response assessments, showcasing its significant superiority over traditional 2D cultures and other existing 3D constructs. Our work marks a significant step forward in the development of advanced models for preclinical research, offering a highly accurate and scalable solution for studying disease progression and therapeutic interventions.

Chapter 3: An in-vivo-mimicking 3D Lung cancer-on-a-chip model to study the effect of external stimulus on the progress and inhibition of cancer metastasis.

Metastatic lung cancer ranks as a primary cause of mortality globally, necessitating innovative research models for better understanding and treatment. In response, this study introduces, develops, and comprehensively characterizes an in-vivo mimicking 3D-lung-cancer-on-a-chip (IVM3DLCOC) model. This model is meticulously designed to more accurately replicate lung pathogenesis in vitro. It encompasses the mechanical and biological properties of the human lung through a co-culture system involving lung cancer cells (A549) and human lung fibroblasts embedded within 3D hydrogels. These hydrogels are engineered to have mechanical properties akin to the native lung extracellular matrix, providing essential biological cues for cellular adhesion and proliferation.

A critical aspect of this model is the replication of physical cues at multiple levels, particularly in the z-axis. This includes fluidic channels that connect to air channels via a porous membrane positioned above the lung epithelial cells. This configuration establishes an air-liquid interface, crucial for simulating inhalation and exhalation cycles. Additionally, the model intricately controls the diffusion of media through the physical barrier of stromal cells, thereby emulating the dynamic physiological microenvironment of the lung.

The IVM3DLCOC model proves to be a better platform for conducting precise studies on disease progression, specifically lung cancer metastasis, and for validating the efficacy of therapeutic agents. To demonstrate its utility, the model was employed

to investigate the impact of cigarette smoke extract (CSE). Findings indicated the preservation of metastatic characteristics (e.g., N-Cad expression) and translational properties (such as IL-6 secretion), underlining the model's effectiveness in mimicking in vivo conditions. Furthermore, the model facilitated dose-dependent drug efficacy testing, observing the cellular response to various anti-cancer agents, thus proving its potential in preclinical drug evaluation.

Importantly, the comprehensive IVM3DLCOC model, incorporating cell constructs along with the lung's representative air and fluid compartments, was efficiently and rapidly prototyped using the 3D extrusion bioprinting technique. This approach facilitated the creation of an all-inclusive, lung-representative unit, enhancing the model's applicability and reliability. Envisioned as a powerful preclinical tool, the IVM3DLCOC model holds promise for detailed studies on the effects of potential chemotherapeutic drugs and toxins on the metastatic progression of lung cancer cells in vitro. Its development marks a significant advance in the field of lung cancer research, offering a sophisticated and accurate platform for exploring the intricacies of lung cancer pathogenesis and treatment efficacy.

Chapter 2 : Functional Colon Reconstruction Using 3D-Bioprinted Native-Like Tissue Architecture for Disease Modeling

2.1 Introduction

To investigate disease progression mechanisms and assess drug efficacy in non-human settings, a variety of experimental models have been developed. These encompass in vivo animal models, which are instrumental for their biological congruence with human systems, allowing for comprehensive studies on disease pathology and therapeutic responses[46]. In vitro models, including two-dimensional (2D) cell cultures, offer a simplified platform for observing cellular interactions and pharmacological effects[47], [48]. Three-dimensional (3D) cultures, such as organoids and spheroids, more accurately recapitulate the intricate cellular microenvironment, offering enhanced fidelity in modeling human tissue dynamics[49], [50], [51]. Additionally, bioengineered systems like microfluidic chips and in silico models leverage advanced technologies to simulate physiological conditions, providing alternative approaches for precision medicine research. These models collectively contribute to our understanding of disease and the development of novel therapeutics, each offering unique advantages and limitations in translational research[52], [53], [54], [55], [56]. The primary limitations of current models lie in their simplified representation of the human body's complexity. 2D monolayers, while

useful for high-throughput screening, lack the three-dimensional structure crucial for understanding cell-to-cell interactions and tissue dynamics, resulting in inaccurate predictions of a drug's efficacy or toxicity[57], [58], [59], [60], [61], [62]. 3D organoids offer a more physiologically relevant environment by providing a three-dimensional context; however, they often lack the full spectrum of cell types found in native tissues[63], [64], [65], [66], [67]. This absence can skew results, especially in studies where immune responses or multicellular interactions play a significant role. Furthermore, organoids' reliance on matrices like Matrigel for structural support introduces variability, as these matrices cannot fully replicate the complex composition of the extracellular matrix in human tissues. Microphysiological systems (MPSs), or "organ-on-a-chip" models, attempt to address some of these issues by integrating fluid flow to mimic blood circulation and by using microfabrication techniques to create more accurate tissue and organ architectures[68], [69], [70], [71], [72]. Despite these advances, MPSs often struggle to maintain long-term cellular viability and functionality, partly due to challenges in simulating the full range of physiological mechanical forces and biochemical gradients present in vivo[73], [74], [75], [76].

These limitations underscore the gap between current in vitro models and the intricate reality of human biology. Misleading outcomes from these models stem from their failure to accurately replicate the mechanical stimuli, oxygen gradients, and multicellular complexity of human tissues, leading to a critical need for the development of more advanced models[77], [78], [79], [80], [81].

Recently, the utilization of 3D bioprinting, combining cells, biomaterials, growth factors, and microfabrication techniques, offers a novel solution to overcome limitations seen in traditional models[82], [83], [84], [85], [86], [87], [88], [89]. However, this technology faces challenges, notably the lack of fabrication methods compatible with a wide range of bioinks to ensure printability, biocompatibility, and the mechanical properties needed for various cell types[90], [91], [92], [93]. To address the challenges associated with traditional models and fabricate an identical tissue model, we employed the Freeform Reversible Embedding of Suspended Hydrogels (FRESH) 3D bioprinting technique. This method facilitated the construction of complex tissue structures, allowing for precise placement of cells and bioinks[94], [95]. There has been a huge effort to replicate in-vivo-mimicking organ models including heart, lung, and trachea through different 3D printing methods[94], [96], [97]. However, there is still a need for fabrication of other in-vivo-mimicking organ such as intestine.

As a result, we successfully for the first time developed a superior in vivo mimicking organ model of the colon that closely mimics the real colon and suitable for in vitro studies while capturing the essential mechanical, physical, and biological properties of real tissue. The choice of the colon as our study model is primarily due to its crucial functions in digestion and nutrient absorption, and its vulnerability to diseases, notably colon cancer—a major health challenge. Our research employs FRESH to create a biofabricated functional colon model. This model is designed based on precise dimensions and morphology from CT scans, achieving an exact replica of the human colon, albeit 10 times smaller. For tissue engineering applications,

recreating the heterogeneity of tissues is essential for developing constructs that functionally and structurally resemble native tissues. This includes the spatial organization of different cell types and ECM components. Heterogeneous models are vital for dissecting the complex interactions and mechanisms underlying various pathologies, including the tumor microenvironment in cancer, where cellular diversity plays a critical role in tumor progression and response to treatment[98], [99], [100], [101], [102]. Therefore, we have facilitated the design of epithelium and subepithelium layers in our in-vivo-mimicking colon model, coupled with tumor spheroid models for our colon cancerous model. This innovative approach addresses the need for advanced preclinical models, providing a highly accurate and scaled-down version of the colon to enhance the study of disease progression and therapeutic interventions.

2.2 Results

2.2.1 Design and Fabrication of colon structure.

The colon, constituting the initial segment of the large intestine, is a muscular tube approximately 1.5 meters (5 feet) long and 5 centimeters (2 inches) in diameter, essential for water and electrolyte absorption and feces elimination. Structurally, all segments of the human intestine, including the colon, are composed of four distinct layers: the intestinal epithelium, subepithelium, muscle layer, and serosa. The epithelium is intricately connected to a mesenchymal stroma network, consisting of fibroblasts, myofibroblasts, endothelial cells, pericytes, immune cells, and neural cells[103], [104], [105]. In this study, we utilized a 3D colon model derived from

human colon Computed Tomography (CT) data, provided by the National Institute of Health (NIH) for research purposes[106]. The model was scaled down to approximate dimensions of 10 mm in length and 5 mm in diameter, reflecting the physiologically relevant geometry of the native intestine, as illustrated in Figure 2.1A. This downscaled model features an inner hollow lumen that facilitates the in vitro reconstruction of a functional 3D intestinal epithelial interface. Concurrently, the outer layer is designed to support fibroblasts, serving as stromal cells that promote intestinal epithelial differentiation and functionality.

To accurately replicate the colon's structure, we've advanced our approach by incorporating the FRESH technique into 3D bioprinting. Hydrogels, resembling the extracellular matrix, stand out for their potential in mimicking soft tissue mechanics and supporting cell growth. However, the direct printing of low-viscosity hydrogels, such as collagen or GelMA, presents challenges due to their inadequate mechanical stability, leading to deformation upon extrusion. Attempts to improve this with thickeners like Alginate only partially addressed the issue, as structural support remained insufficient. FRESH, an innovative method in 3D bioprinting, provides the necessary support during printing, enabling the use of these hydrogels to create complex, stable structures. This technique revolutionizes the fabrication process by reinforcing bio-ink extrusion, thus offering a significant advancement in accurately modeling biological structures (Figure 2.1C).

Building on our printing experiments, we evaluated four bioink formulations: 5% and 7.5% GelMA, a mix of 7.5% GelMA with 0.25% Alginate, and 7.5% GelMA with 0.5% Alginate, aiming to achieve optimal printability, structural integrity, mechanical

strength, and cell growth in our 3D models. All bioinks exhibited shear-thinning properties essential for 3D printing, with increased GelMA concentration and Alginate addition enhancing viscosity, demonstrated through rheological tests (Supporting Information Note 1 and Figure 2.6) However, for superior structural integrity, particularly in free-standing models, viscosity alone is insufficient. Notably, the 7.5% GelMA with 0.5% Alginate bioink excelled in maintaining its shape within the support bath, attributed to synergistic crosslinking. The GelMA, activated by LAP (a biocompatible photoinitiator), undergoes UV photocrosslinking, forming a covalent network. Alginate's ionic crosslinking, triggered by calcium ions in the support bath, further stabilizes the structure[107], [108]. This dual-crosslinking mechanism, utilizing a biocompatible bioink, significantly improves post-printing shape retention. Our optimized protocol leverages both composition and crosslinking strategies for tailored applications.

To assess how well our printing protocol could create complex, heterogeneous colon tissues involving multiple cell types or bioinks, we undertook a double-layer 3D printing approach for the colon. This method involved using two distinct bioink compositions to replicate different functional layers of the colon's structure. Our construction process entailed printing a total of 100 layers, starting with the outer layer and then adding the inner layer. Following the printing process, we used UV light (405 nm) for 1 minute to photo-cross-link the structure, ensuring its stability. Finally, the construct was placed in an incubator for 30-40 minutes. This step allowed the support bath to fully dissolve, freeing the 3D printed colon structure (Figure 2.1D). We've documented this process visually, providing a side view and top view of the

completed construct in Figure 2.1B and 2.1C, with further details available in Movie S1 in the Supporting Information.

Moreover, we aimed to quantitatively evaluate the fidelity of 3D printed constructs against their corresponding 3D models using a set of image comparison metrics. Through image processing and comparison techniques, including conversion to HSV color space and color-specific thresholding, we generated binary masks for a precise analysis of the constructs against their backgrounds. This preparation allowed us to apply the Structural Similarity Index (SSIM) and Mean Squared Error (MSE) metrics to evaluate the visual and structural fidelity of the printed colon to its 3D model counterparts. Our findings, highlighted by high SSIM values (0.9401 and 0.9521 for back and front views, respectively) and low MSE values (0.0447 and 0.0266 for back and front views, respectively), demonstrated a strong alignment and minimal pixel-wise discrepancies between the printed constructs and the 3D models, underscoring the precision of our 3D printing process. These results are further detailed and visually represented in Supporting Information Note 2, Figure 2.7A, and Figure 2.7B.

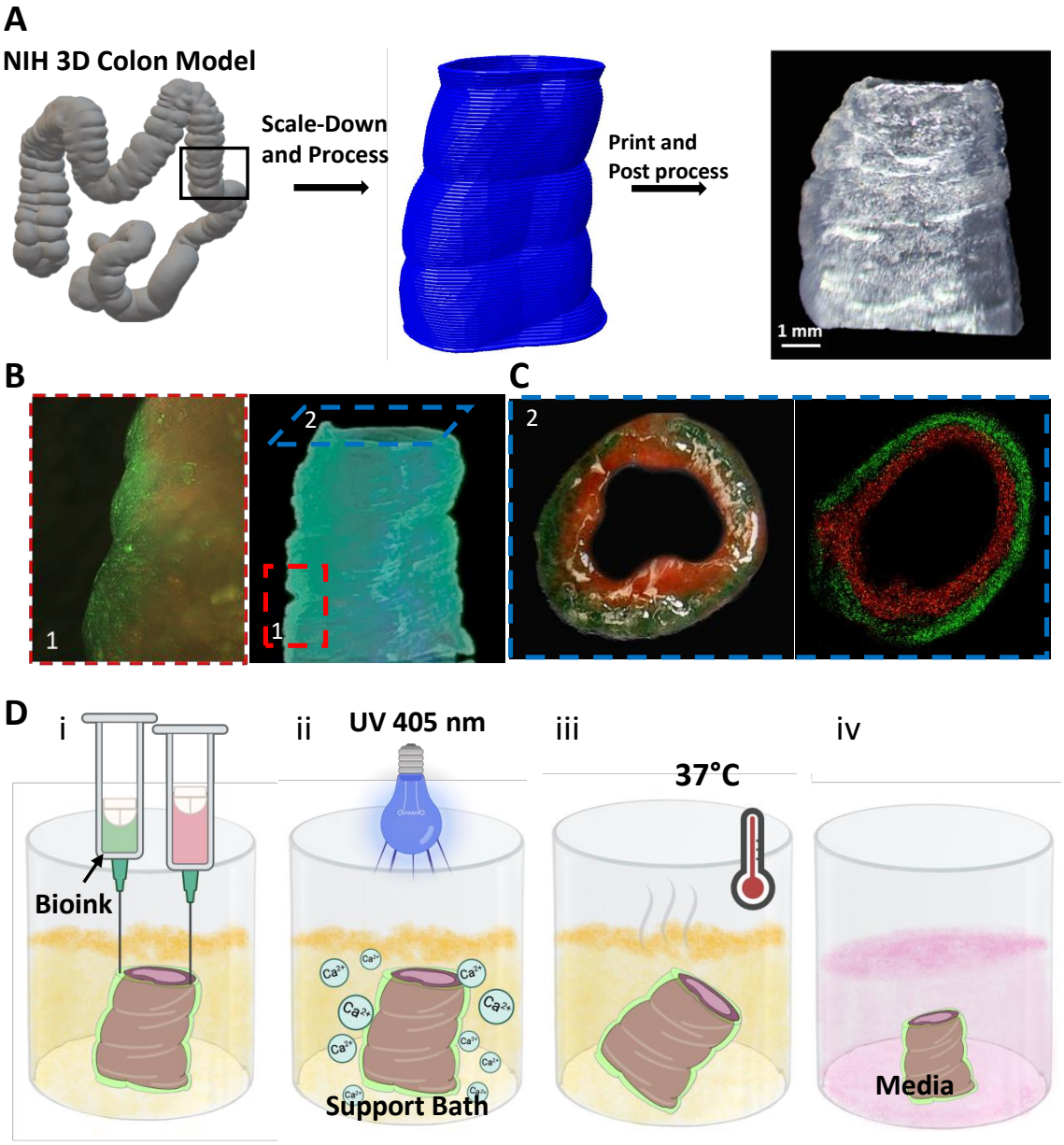

Figure 2.1. Fabrication and analysis of 3D colon structure. (A) Schematics presenting a human colon from NIH 3D colon model is scaled down and processed for printing. (B) Side view images of the dual-layer 3D printed colon after photo-cross-linking and washing steps, using green and red fluorescence to distinguish the layers for imaging purposes. (C) Top view of the same structure, highlighting the stratification with fluorescent markers. (D) Schematic of dual-material FRESH printing using cell-laden hydrogel bioinks

2.2.2 Characterization of the 3D-printed colon structure

To determine if our hydrogel formulations mimic the mechanical properties of native soft tissues, we conducted compression tests on four bioinks: GelMA at 5% and 7.5%, and GelMA 7.5% mixed with 0.25% and 0.5% Alginate, respectively, using an Instron system (Figure 2.8, Supporting Information). Results showed a progressive increase in the Young's modulus (E) with Alginate addition, from 15.8 ± 0.2 kPa for GelMA 7.5%, to 43 ± 2.4 kPa and 65 ± 8.5 kPa for mixtures with 0.25% and 0.5% Alginate, respectively (Figure 2.2A). These findings, aligning with in vivo soft tissue mechanics (with E ≈ 1-100 kPa) suggest our hydrogels' suitability for physiologically relevant colon tissue modeling.

Furthermore, we explored various GelMA and Alginate volume ratios to optimize 3T3 fibroblast adhesion, proliferation, and elongation. Embedding 3T3 fibroblasts in differing hydrogel mixes, we assessed cell growth through monitoring them by phase contrast microscopy images. The findings revealed that higher GelMA concentrations coupled with lower Alginate percentages favored the formation of a more dispersed and elongated fibroblast network, as opposed to dense cell aggregations (Figure 2.9, Supporting Information). Notably, the GelMA 7.5% plus Alginate 0.5% composition emerged as particularly conducive for colon tissue engineering, striking a balance between printability, structural integrity, and the biomechanical environment necessary for cell proliferation and tissue development.

In 3D bioprinting, especially for complex structures, two critical considerations are the bioink's cytocompatibility and the shear forces applied to cells during the

extrusion process. To assess these factors, we monitored cell viability and proliferation within our 3D-printed colon constructs over 14 days post-printing as depicted in Figure 2.2B. Quantitative analysis of 3T3 fibroblast viability within the constructs revealed that it exceeded 90% on the first day post-printing and notably increased to over 95% at the end of two weeks in culture (Figure 2.2C). This indicates that the shear forces encountered during extrusion, subsequent embedding in a support bath, and UV light exposure did not adversely affect cell viability, as further evidenced by Figure 2.10 in the Supporting Information.

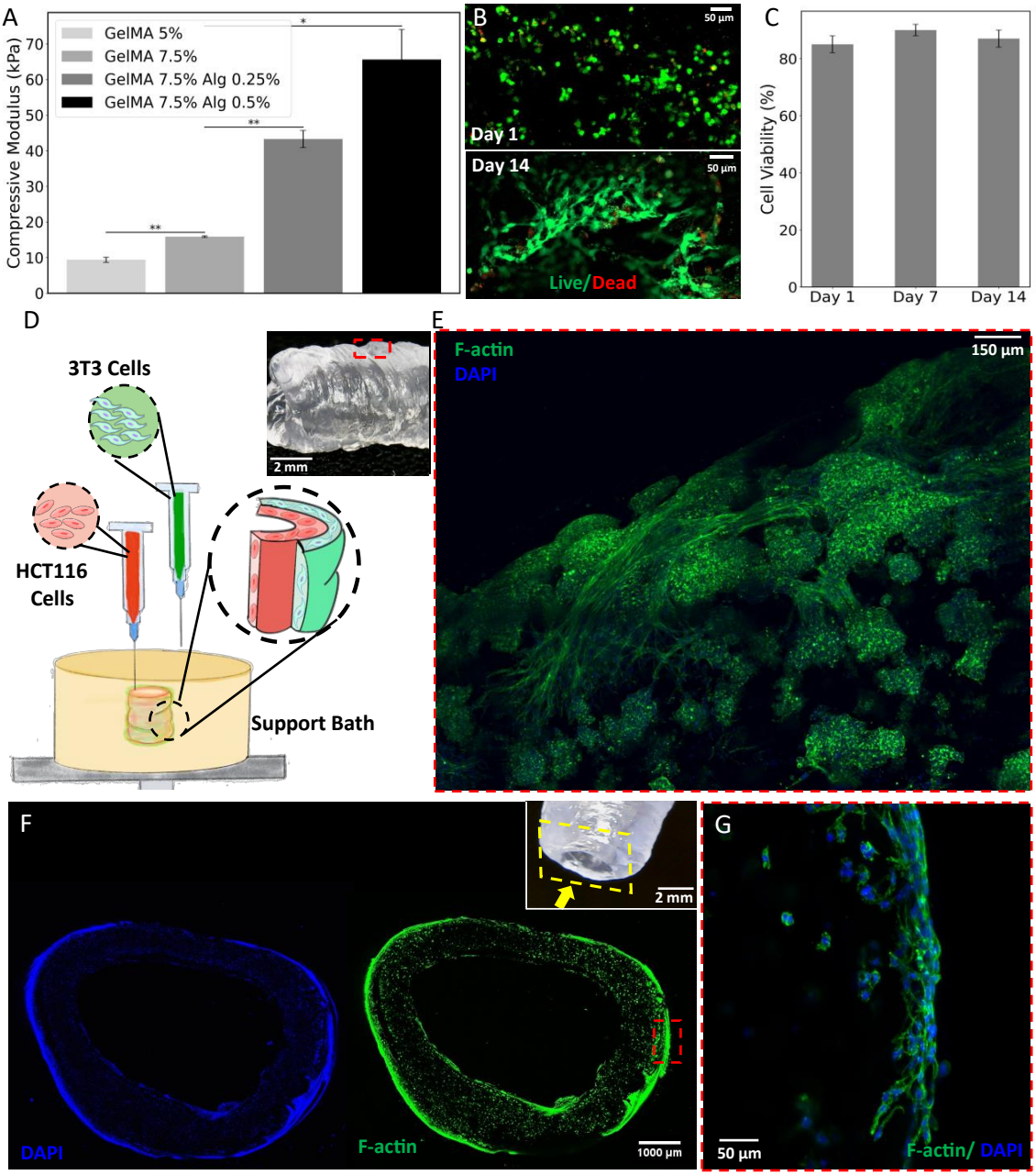

Figure 2.2 Characterization of 3D bioprinting of cell-laden colon constructs. (A) Mechanical properties of GelMA/Alginate composite hydrogels, showing comparison of compressive Young's modulus E for four different bioink. (B) Live/dead staining of the colon construct at day 1 and day 14 post bioprinting. (C) Viability of 3T3 fibroblast in 3D-printed colon construct over 14 days of culture. (D) A schematic to describe 3D bioprinting colon cancer constructs with fibroblast-laden GelMA/Alg bioink and HCT116-laden GelMA/Alg bioink. (E) Immunostaining of colon cancer construct against F-actin (green), and DAPI (blue) at day 21 post bioprinting from a side view indicating tumor spheroid and fibroblast network

formation. An image at the left shows the colon construct with the red box indicate the point of view. (F) Immunostaining of colon construct bioprinted with 3T3-laden bioink to represent the fibroblast elongation and network formation, F-actin shown in green, and DAPI shown in blue at day 14 post bioprinting from top view. An inset at the right shows the colon construct with the yellow box indicating the point of view. (G) A zoomed-in view of peripheral area illustrating how fibroblasts are elongated and formed a dense network on the peripheral. *p < 0.05, **p < 0.005, and ***p < 0.0005

To emulate the heterogeneous tissue environment of the colon using diverse cell types, a bi-layered construct was developed, incorporating 3T3 fibroblasts to establish a stromal layer and HCT 116 cells to simulate colon carcinoma, as depicted in Figure 2.2D. This construct was produced following a predefined bioprinting protocol and was cultured for a duration of 21 days. Initial cell viability for both 3T3 and HCT 116 cells exceeded 90% at day 1 post-printing. Notably, within the hydrogel matrix, the HCT 116 cells, known for their aggressive cancerous behavior, aggregated into spheroids and showed significant growth throughout the culture period. By day 21, these spheroids reached an average diameter of 500 μm, as detailed in Figures 2.2E and 2.11 Supporting Information. Concurrently, the 3T3 fibroblasts on the construct's outer surface elongated, creating a dense, interconnected network that further contributes to the construct's mimicry of colon tissue architecture. The migratory behavior of the fibroblasts was observed as they moved toward the periphery of the construct and elongated, resulting in a dense, interconnected network, as evidenced by immunostaining for DAPI and F-actin of 3T3-laden bioprinted colon construct at day 14, illustrated in Figures 2.2F and 2.2G. In these figures, cell nuclei are stained blue and F-actin filaments green, providing lateral and aerial perspectives of the structure.

In order to preserve the construct's morphology for imaging, we employed a technique that involved embedding the hydrogel samples in a 1% agarose gel and sectioning them into 1 mm slices. The procedure is elaborated in detail in the materials and methods.

Creating a functional 3D colon model that mirrors the physiological structure and function of the native colon necessitates an accurate reconstruction of the epithelial layer. The intestinal tract's defining feature, a monolayer of columnar epithelium composed mainly of absorptive enterocytes, forming a continuous, protective barrier critical for gastrointestinal integrity. This necessitates the inclusion of the epithelial layer in in vitro colon models to mimic true functionality. However, the precision required for replicating this single-cell layer presents a challenge due to the resolution limitations inherent in 3D printing technologies. As an initial step, we fabricated the three-dimensional colon structure utilizing a 3T3 cell-laden hydrogel. Within our engineered 3D scaffolds, a central hollow lumen facilitates the establishment of a functional epithelial interface in vitro. On the seventh day post-printing, Caco-2 cells, which serve as a model for human colorectal epithelial enterocytes, were seeded into the hollow lumen of the 3D printed colon constructs. This process was aimed at forming an epithelial barrier, as illustrated in Figure 2.3A. Over a period of 14 days, these cells uniformly and continuously coated the structure, culminating in the formation of a robust epithelial barrier contiguous with the lumen of the 3D construct. Immunofluorescent imaging at day 14 post-cultivation demonstrates the epithelial confluence achieved by Caco-2 cell coverage, as evidenced by DAPI and F-actin staining. This illustrates cellular proliferation and the formation

of a dense, continuous barrier layer. Figure 2.3B provides a top-down perspective of the epithelium, while Figure 2.3C offers insight into the inner region of the construct.

Moreover, immunofluorescent images depicted the development of protrusions towards the lumen that improve the absorption functionality of human colon tissue. A zoomed-in view of these structures, as shown in Figure 2.3D, reveals structures extending towards the hollow lumen, with cell nuclei stained in blue and actin filaments in green. This phenomenon is explained by the 3D architecture of the colon model and its luminal curvatures influencing enterocyte cell behavior to mature, polarize, and differentiate to form microstructures, as previous studies have shown that curved surfaces contribute to apical-basal polarization that increases intestinal epithelial barrier functions. The polarized epithelium, typical of mature enterocytes, indicates that our 3D printed colon architecture provided a suitable 3D niche for intestinal epithelial cells to attach and differentiate (Figure 2.3F). Furthermore, the expression of tight junction proteins, including Zonula occludens-1 (ZO-1), confirms the intestinal epithelial differentiation[109], [110], [111]. This analysis revealed that the epithelial cells exhibit tight junction formation, as evidenced by ZO-1 immunostaining within the scaffold lumen, as displayed in Figure 2.3E and 2.12, and Movie S2 Supporting information, presenting the cell nuclei in blue, f-actin in green, and ZO-1 in red.

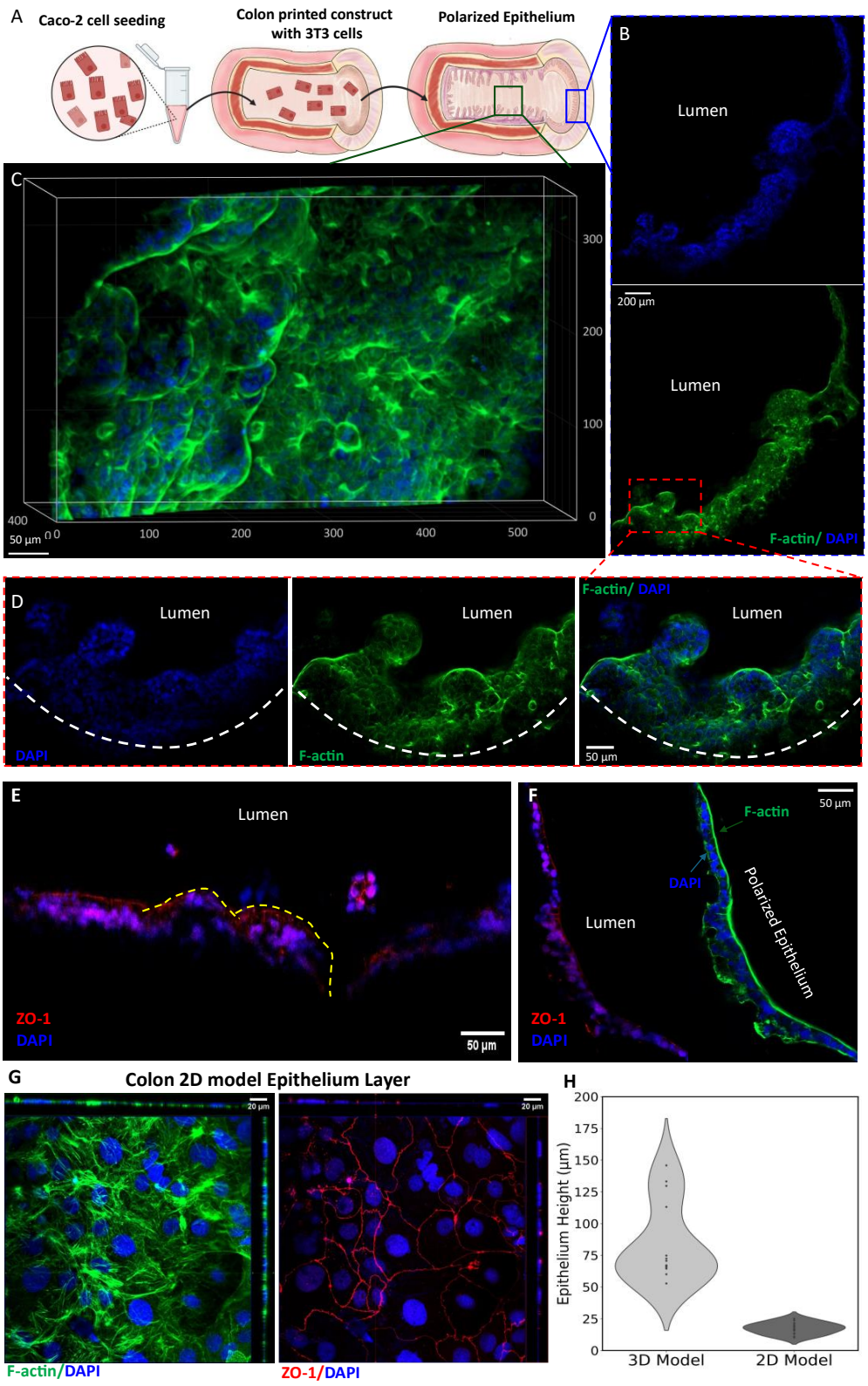
A
Caco-2 cell seeding
Colon printed construct with 3T3 cells
Polarized Epithelium
B
Lumen
200 µm
Lumen
F-actin/ DAPI
C
300
200
100
0
400
50 µm
0
100
200
300
400
500
D
Lumen
DAPI
Lumen
F-actin
F-actin/ DAPI
Lumen
50 µm
E
Lumen
ZO-1
DAPI
50 µm
F
50 µm
F-actin
DAPI
Polarized Epithelium
Lumen
ZO-1
DAPI
G
Colon 2D model Epithelium Layer
20 µm
20 µm
F-actin/DAPI
ZO-1/DAPI
H
Epithelium Height (µm)
200
175
150
125
100
75
50
25
0
3D Model
2D Model

Figure 2.3. Characterization and Comparison of 3D Colon Epithelium and 2D Transwell model. (A) Schematic of the 3D printed colon construct with Caco-2 cell seeding, showing progression to a polarized epithelium with microstructures. (B) Top view immunofluorescent depiction of Caco-2 cell-mediated epithelial coverage at day 14, highlighting the compact, confluent barrier formation as evidenced by DAPI and F-actin staining. (C) Inner area visualization of the formed epithelium within the lumen part, detailing the cellular arrangement and barrier integrity. (D) Cross-sectional images further illustrate the protrusions extending into the lumen, with actin filaments visualizing the cellular architecture. (E) and (F) The expression of ZO-1 (in red) indicates tight junction formation between cells, signifying the establishment of a polarized and differentiated epithelium. (G) The 2D Transwell model with Caco-2 cells forming a tight, continuous monolayer, exhibiting F-actin (in green), cell nuclei (in blue), and ZO-1 (in red). (H) A violin plot comparing the distribution of epithelium heights in the 3D model to the epithelium height in the 2D model, demonstrating the morphological superiority of the 3D model in mimicking in vivo-like structure, as measured by immunofluorescence. This figure underscores the enhanced physiological relevance of the 3D colon model over traditional 2D cultures, providing a more accurate in vitro system for studying epithelial integrity and function relevant to intestinal tissue engineering and drug discovery.

In intestinal tissue engineering, culturing Caco-2 epithelial cells on Transwell inserts is a recognized approach for examining epithelial interactions[112], [113], [114]. This study enhances this conventional model by introducing fibroblasts beneath the inserts to mimic the stromal layer, while Caco-2 cells form the epithelial layer above. After 14 days of maturation, we utilized immunofluorescence microscopy to assess the cell morphology and expression of ZO-1 in Transwell format. Figure 2.3G illustrates that the Caco-2 cells within this Transwell arrangement developed tight junction patterns indicative of monolayer integrity. To further evaluate cellular morphology, we generated Z-stacks, allowing for the inspection of epithelium morphology between two-dimensional and three-dimensional growth conditions. The Caco-2 cells in Transwell consistently exhibited a flat monolayer formation of the

epithelium layer. The quantitative assessment of epithelium height in both Transwell and 3D models, showcased in Figure 2.3H, revealed an epithelium height of around 20 μm for the 2D Transwell format, and a range from 20 μm to 180 μm in the 3D configuration. Our 3D model's epithelium microstructures height distribution is summarized in a violin plot, highlighting median epithelium height around 65 μm. The measurements for epithelium microstructures height were conducted using immunofluorescent imaging, with the baseline for measurement delineated in the images (Figure 2.12, Supporting Information).

Our three-dimensional colon model exhibits a morphology that more closely resembles the in vivo colon tissue architecture, surpassing traditional two-dimensional Caco-2 cell monocultures on Transwell systems. These conventional models fail to develop polarized epithelium and enlarged surface area. Our enhanced three-dimensional colon model, therefore, presents a more physiologically relevant in vitro system for the examination of epithelial integrity and function.

2.2.3 Functional analysis of the bioprinted colon tissue

To validate our system's ability to create suitable 3D environments for cell culture, we assessed the barrier integrity of colon epithelium by measuring Transepithelial Resistance (TEER) over time[115], [116]. Initial TEER evaluations were conducted on Caco-2 cells, both in monoculture and co-cultured with 3T3 fibroblasts, using Transwells in 2D and 2.5D formats (Figure 2.4A). In the 2D setup, Caco-2 cells were seeded on the apical side of the Transwell for monocultures, and for co-cultures, fibroblasts were first seeded on the underside, followed by Caco-2 cells on top. The 2.5D formats involved disc-shaped hydrogels, both with and without

embedded fibroblasts, serving as a base for Caco-2 cell seeding in both mono and co-cultures. TEER measurements spanned from day 1 post-seeding to day 21, utilizing blank Transwells and 3T3 cells alone as controls for monocultures and co-cultures, respectively. As depicted in Figures 2.4B and 2.4C, TEER values showed a consistent increase across the culture period for both hydrogel-based and porous filter membrane setups, indicating the successful establishment of a functional epithelial barrier. Notably, the 2D Caco-2 monocultures exhibited the highest TEER values, around 860 $\Omega.cm^2$, which then decreased to below 260 $\Omega.cm^2$ in 2.5D co-cultures with 3T3. The integration of 3T3 cells and GelMA gel within the 2.5D co-cultures was observed to modulate the characteristics of the Caco-2 cell layer, resulting in reduced TEER values when compared to monocultures, thus emphasizing the subepithelial layer's role in tight junction modulation. This reduction in TEER values in co-culture setups more accurately mirrors the in vivo colon TEER of 300-400 $\Omega\,cm^2$, suggesting a model that is more physiologically representative[117]. For the TEER measurements of the 3D colon construct, we employed a two-point method, fitting the hollow structure between two electrodes to monitor impedance changes throughout the culture period (Figure 2.4D). The measurement chamber was specially 3D printed to house the electrodes, ensuring their consistent positioning during all measurements. The electrodes' biocompatibility was verified, demonstrating minimal cytotoxic effects on cell growth and affirming their suitability for use (Figure 2.13, Supporting Information). From day 4 to day 21 of culture, TEER measurements showed an increase in impedance in the colon construct with Caco-2 cells, signifying a successful barrier formation (Figures 2.4F and 2.4G). Additionally, to further assess the integrity

of the epithelial barrier, we analyzed electrical impedance spectroscopy (EIS) to evaluate the electrical properties of both blank samples and those including Caco-2 cells, revealing significant insights into the barrier's development over time (Figure 2.4E). These comprehensive findings underscore our 3D colon model's effectiveness in emulating the physiological barrier properties of the colon epithelium, highlighting its potential as a valuable tool in intestinal tissue engineering.

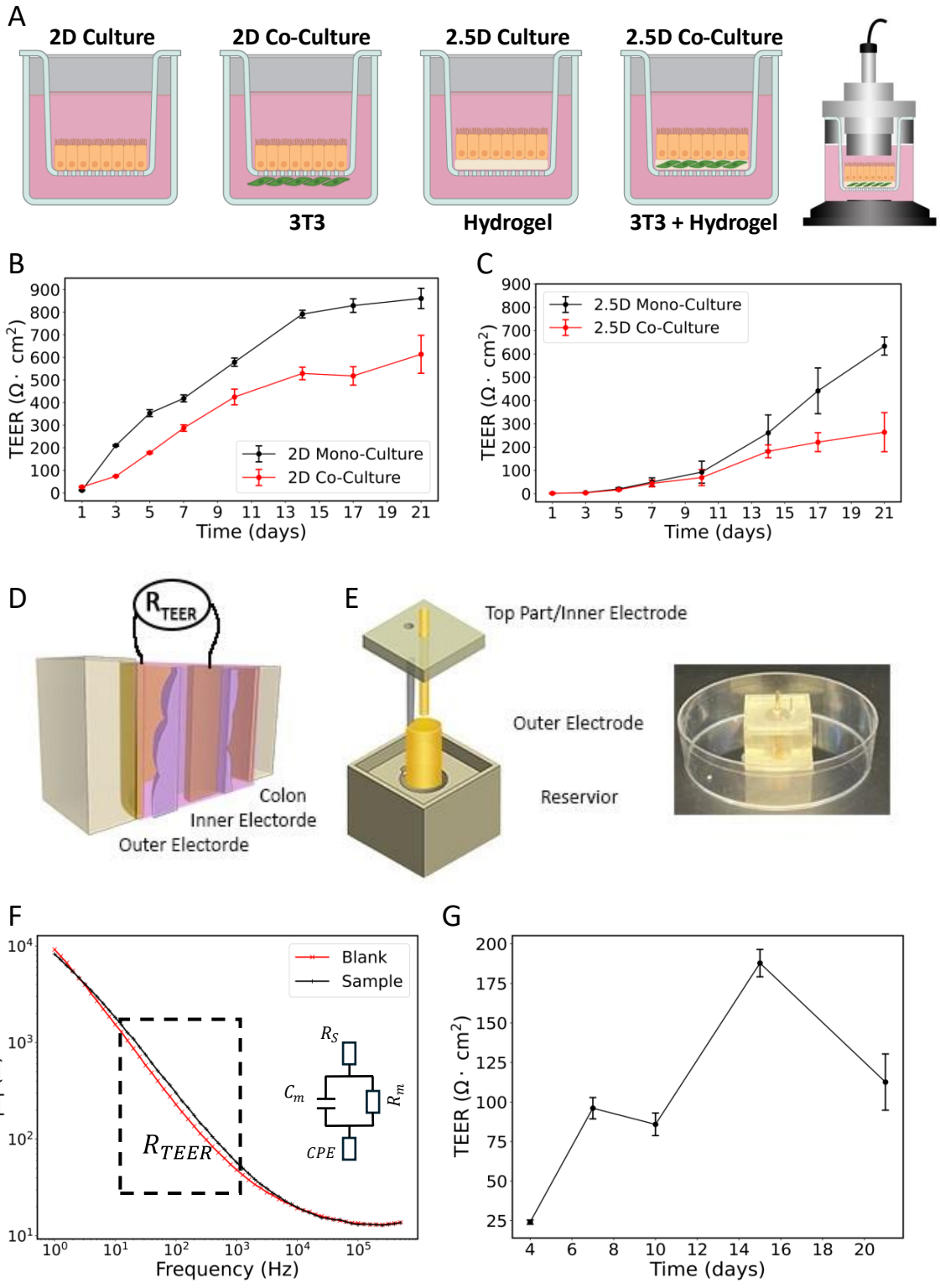
A
2D Culture
2D Co-Culture
2.5D Culture
2.5D Co-Culture
3T3
Hydrogel
3T3 + Hydrogel
B
TEER (Ω · cm²)
Time (days)
2D Mono-Culture
2D Co-Culture
C
TEER (Ω · cm²)
Time (days)
2.5D Mono-Culture
2.5D Co-Culture
D
R_TEER
Colon
Inner Electorde
Outer Electorde
E
Top Part/Inner Electrode
Outer Electrode
Reservior
F
|Z| (Ω)
Frequency (Hz)
Blank
Sample
R_TEER
R_S
C_m
R_m
CPE
G
TEER (Ω · cm²)
Time (days)

Figure 2.4 Evaluation of Transepithelial Electrical Resistance (TEER) in different cell culture models. (A) Schematic representations of the various culture systems: 2D Culture, 2D Co-Culture with 3T3 fibroblasts, 2.5D Culture on hydrogel disk, and 2.5D Co-Culture with 3T3-laden hydrogel disk setups. (B) TEER measurements of Caco-2 cells in monoculture and co-culture with 3T3 fibroblasts in 2D Transwell systems over 21 days, showing a higher resistance in monocultures. (C) TEER measurements of 2.5D Caco-2 cells in monoculture and co-culture with 3T3 fibroblasts, indicating a reduction in TEER values for co-culture systems. (D) Illustration of the TEER measurement setup with inner and outer electrodes for the colon model. (E) The design and assembled view of the measurement chamber with inner electrode and outer electrode within the reservoir. (F) Impedance spectra (|Z|) of blank and sample colon constructs over a frequency range, highlighting the TEER region of interest. (G) TEER values of Caco-2 cells cultured in 3D colon constructs from day 4 to day 16, showing a peak in barrier function at around day 12. The results demonstrate the influence of 3T3 cells as stroma layer and 3D architecture matrices on Caco-2 cell barrier integrity, with TEER values aligning more closely with in vivo conditions of the human small intestine.

2.2.4 Generation of colon cancerous model and study of the Effect of 5FU Treatment on the 2D and 3D models

In our study to establish a cancer model that mimics the in vivo tumor environment for effective drug screening, the HCT116 colorectal adenocarcinoma cell line was selected due to its origin from a malignant tumor, its aggressive growth, and its lack of differentiation capability[118], [119]. To simulate the tumor microenvironment more accurately, we cultured HCT116 cells to form tumor spheroids, achieving a size that reflects the ratio between the colon lumen and actual colon cancer polyps. Utilizing the hanging drop method, HCT116 cells aggregated into compact spheroids, approximately 500 μm in diameter, over 7 days (Figures 2.5A, 2.5B, and S9), aiming to represent the size of a stage I native tumor (5-10 mm)[120], [121].

As controls for our 3D colon architecture, we employed several models including Monolayer Culture: HCT116 cells grown in standard 2D culture conditions

for baseline comparison; Tumor Spheroids: Formed using the hanging drop method to better mimic the 3D tumor environment; and Transwell Model with Co-cultured Fibroblasts: Seeding fibroblasts on the underside of the Transwell, with Caco-2 cells and then HCT116 spheroids on the epithelial layer, cultured for an additional three days to replicate the tumor-stroma interaction.

In our experimental setup, we first 3D printed a 3T3-laden hydrogel into a colon-like architecture. After 5 days of culturing, Caco-2 cells were seeded within the hollow part of this construct and allowed to attach and grow for another 14 days before implanting the HCT116 cancer spheroids. Bright field images show the colon construct with implanted cancer spheroids one day post-implantation (Figure 2.5A-iv). Tumor growth rates within the colon construct were assessed by measuring the metabolic activity of samples due to the growth of cancer spheroids for three days post-implantation (Figure 2.5C).

To evaluate drug efficacy, we exposed both Transwell and 3D colon cancer models to varying concentrations of 5-Fluorouracil (5FU), widely used chemotherapeutic drug against colorectal cancer[122], [123] . Cell viability was quantified from 0 to 72 hours post-treatment with escalating concentrations of 5FU, using a metabolic activity assay (Figure 2.5D). The Transwell model exhibited a significant dose-dependent reduction in metabolic activity at 24-hour exposure to 5FU (Figure 2.5E). The IC50 value, indicative of the concentration of a drug required to inhibit a biological process by half, serves as a crucial metric in pharmacology for gauging drug potency. We calculated the half-maximal inhibitory concentration (IC50) across the models to assess the 3D microenvironment's influence on

chemotherapeutic response. The Transwell model's IC50 was approximately 42 μM, significantly higher than in monolayer cultures of HCT116 and HCT116 spheroids, pointing to the stromal layer's role in fostering chemoresistance (Figures 2.5F, 2.5I, and Supplementary Information S10).

The 3D colon architecture model's response to 5FU demonstrated a dose-dependent decrease in tumor cell metabolic activity, with an IC50 of approximately 540 μM, indicating a substantial increase in drug resistance compared to the control models (Figures 2.5G and 2.5H). These findings emphasize the 3D colon architecture's superiority in mimicking in vivo conditions, offering a more accurate platform for studying cancer progression and screening drug efficacy. This analysis highlights the necessity of using 3D models that closely replicate the tumor microenvironment for enhanced comprehension and treatment of colorectal cancer.

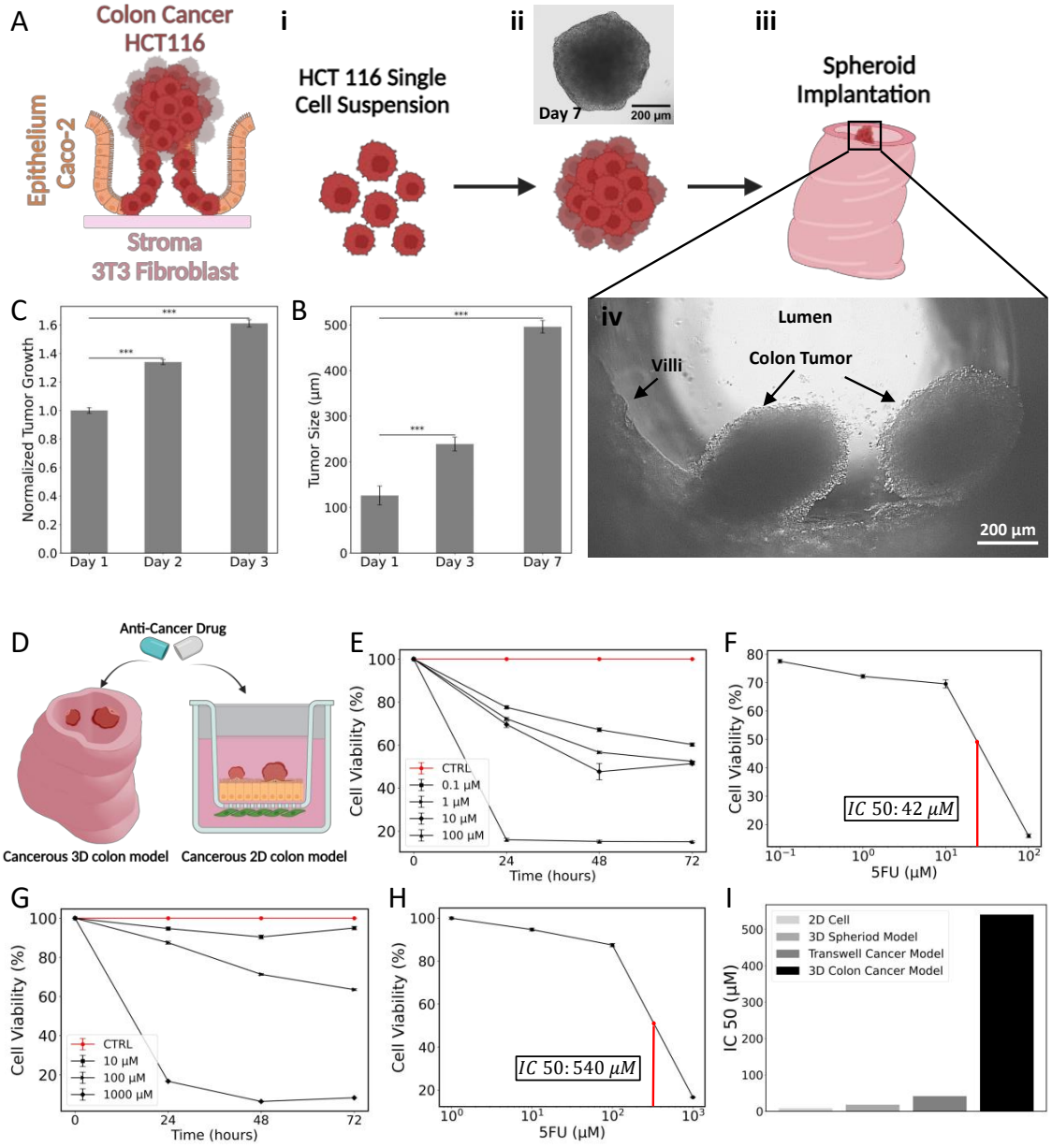

Figure 2.5 Development and Validation of an In-vivo-mimicking Colon Cancer Model for Drug Screening. (A) Schematic of the epithelium-stroma interface with HCT116 colorectal adenocarcinoma cells, (i-iii) Stepwise development of HCT116 spheroids from single-cell suspension to spheroid implantation into a 3D printed colon construct with highlighted implanted tumor within the lumen in a bright field image (iv). (B) Spheroid growth indicated as spheroid diameter over 7 days utilizing hanging-drop method. (C) Tumor growth within the colon construct based on metabolic activity over 3 days. (D) Schematic showing the exposure of both Transwell and 3D cancerous models to 5FU. (E) Dose-dependent cell viability of the Transwell cancer model over time upon 5FU treatment at 0.1-1-10-100 µM. (F)

Determination of IC50 value for the Transwell cancer model by non-linear regression. (G) Cell viability of the 3D colon cancer model over time with varying concentrations of 5FU, at 10-100-1000 μM. (H) IC50 value estimation for the 3D colon cancer model, indicating a significant increase compared to the Transwell model. (I) Comparative IC50 values across different model formats, highlighting the enhanced chemoresistance in 3D models. These results support the use of 3D cancer models as more representative of in vivo conditions for cancer progression studies and drug efficacy screening. *$p < 0.05$, **$p < 0.005$, and ***$p < 0.0005$

2.3 Discussion

Our study highlights the development of a novel functional three-dimensional colon model through FRESH 3D bioprinting, offering significant advancements in colorectal cancer research and therapeutic screening. This breakthrough directly tackles the critical limitations of traditional models, providing an accurate replication of the human tissue's complex microenvironment. The design and fabrication process of the colon structure, as detailed in our results, emphasizes not only the precision but also the complexity involved in recreating such a vital organ.

Over the past decade, a multitude of research endeavors have been undertaken to replicate in vitro colon tissue through various methodologies[124], [125], [126], [127]. Among these, Chen et al. introduced a bioengineered three-dimensional half-luminal tissue model of the intestine, employing a silk sponge scaffold via mold-casting fabrication. This model aimed at facilitating high-throughput analysis of the human gut microbiome[128]. Despite its innovative approach, this model is more representing a scaffold with a semi-cylindrical channel, omitting the actual luminal curvature and crypt structures. In a more recent advancement, two separate research entities have succeeded in fabricating three-dimensional geometries of crypts and villi using collagen-based bioinks to replicate small intestine in vitro. One team utilized a singular bioink consisting of Caco-2 cells to forge an epithelial layer, whereas another

advanced the methodology by employing two distinct layers: one comprised of Caco-2 cells for the epithelial layer and another of Human Umbilical Vein Endothelial Cells (HUVECs)[129], [130]. In both instances, the presence of crypt/villi architecture was found to enhance homogeneity, elevate proliferation rates, and augment the expression of differentiation markers when contrasted with models devoid of crypt-villus architecture. Although these innovations signify progress in modeling the human intestine, they have yet to mimic the luminal curvature characteristic of the native large intestine. The curvature of luminal structures is essential for the physical organization and functionality of various cell types, including those of stromal and epithelial origin found in corneal, renal, pulmonary, and intestinal tissues[125]. Notably, mesoscale curvature exerts a dominant influence on cell behavior over nanoscale topographical cues[131], [132]. To replicate the diverse curvatures encountered in vivo, numerous approaches have been adopted. These methods have elucidated that the cell's cytoskeleton and nucleus interact dynamically, with the nucleus acting as a mechanosensor, promoting cellular migration preferentially within concave geometries. Investigations into cellular responses to substrate curvature have revealed that apical stress fibers align radially and span concave surfaces to minimize bending, while basal fibers adapt to convexity. This response promotes enhanced apical-basal polarization on curved substrates compared to flat ones[133]. To our knowledge, the current study introduces, for the first time, a three-dimensional bioprinted colon structure that accurately incorporates actual luminal curvature.

Interestingly, we evidenced the formation of microstructures in our in-vivo-mimicking 3D colon model, improving the absorption functionality. This evidence is

lacking when we looked for it in the 2D format. In vitro experiments show that mouse intestinal fibroblasts can contract and buckle the extracellular matrix (ECM), controlling the folding patterns of the intestinal epithelium[134]. Moreover, the ability of Caco-2 cells to undergo villus morphogenesis has been previously observed by other groups[135]; however, they have been studied the monoculture of the cells under the dynamic flow, and its mechanical tension suggesting that microenvironmental cues (e.g. microfluidic flow, cyclic mechanical strain) will induce the villus differentiation. Having the cells reside in 3D niche which accurately mimic the native tissue topography can induce the cells with mechanical tension needed for differentiation and form the functional microstructures in vitro. Furthermore, we anticipate culturing our colon 3D model in a dynamic bioreactor format where the mechanical cues due to peristaltic movement could also be simulated, will enhance the villus differentiation which potentially can be a future direction for this study.

The utilization of a specific model for evaluating drug efficacy, with a focus on colorectal cancer (CRC) treatments, has demonstrated promising outcomes. The uniform exposure of cells in a monolayer culture to chemotherapeutic agents, predominantly comprising proliferative cells, contrasts with the resistance observed in spheroid cell culture models. These models encompass cells at various stages of the cell cycle, thereby better replicating in vivo conditions, including aspects of the cell cycle, morphology, nutrient requirements, and behavior[136], [137]. Spheroid formation in 3D cultures allows CRC cells to sustain minimal proliferation rates. This rate diminishes as the spheroid size increases, due to the accumulation of quiescent cells at the spheroid's center, which in turn augments resistance to

chemotherapy[138], [139]. Recent decades have witnessed significant employment of colon cancer cell spheroids in drug development studies. Yet, the implementation of colon cancer spheroids within a mature, topographically structured hydrogel into an native organ architecture remains unexplored[140], [141], [142]. This approach proposes a complex model that incorporates aggressive colon cancer spheroids and a native tissue-like extracellular matrix (ECM) in interaction with fully matured epithelium, thereby replicating the in-vivo tumor environment surrounded by ECM and stromal cells. This environment is intricately linked to tumorigenesis, with 3D cell cultures more accurately mirroring cancer cell phenotypes, such as hypoxia and the activation of angiogenesis, unlike 2D models.

Our findings indicate a marked superiority of in vivo mimetic models over traditional 2D cultures and existing 3D constructs in assessing drug responses, highlighting the necessity of employing physiologically accurate models for preclinical testing. This can lead to the development of more effective and targeted therapeutic strategies. Specifically, the observed dose-dependent reduction in tumor cell metabolic activity in response to 5-Fluorouracil (5FU) treatment within our 3D colon architecture model—yielding an IC50 significantly higher than those observed in 2D and simpler 3D models—emphasizes the critical influence of the microenvironment on drug resistance. The reduced sensitivity of the 3D colon cancer model to 5FU treatments, compared with conventional 2D cell cultures, underscores the propensity of anticancer drugs to be overestimated for their cytotoxic activity in 2D-culture-based screenings. As previously reported, a mere 20% of patients undergoing 5-Fluorouracil (5-FU) treatment achieve plasma concentrations within the optimal Area Under the

Curve (AUC) target range and the majority of the patient cohort are underdosed[143], [144]. The interaction among various factors, such as intracellular changes and paracrine signaling, along with modifications in the supporting matrix, likely contributes to diminished drug sensitivity in the human body. This suggests the necessity for more complex organ models that maintain the organ's architecture alongside its supporting matrix and mimic tissue functionality. Such findings are crucial for understanding the complexities of cancer progression and highlight the potential of 3D bioprinted models to transform the fields of drug development and cancer research.

While our study marks a significant stride towards more accurate disease modeling and drug screening, it is not without limitations. Future research should focus on expanding the model's application to other gastrointestinal diseases, improving the model's scalability, and exploring the integration of additional cell types to further enhance physiological relevance. Additionally, advancements in bioprinting technology and bioink formulation are essential to address current limitations and expand the capabilities of 3D bioprinted models.

2.4 Conclusion and Future Direction

In this study, we have successfully pioneered the development of a functional, three-dimensional colon model through the application of advanced 3D bioprinting techniques, marking a significant stride in the realm of colorectal cancer research and drug screening. By leveraging the FRESH method alongside optimized bioinks, we have engineered a dual-layered construct that meticulously replicates the colon's

intricate architecture. This includes the emulation of 3D luminal curvature and native-like tissue macrostructures, featuring both inner epithelial and outer lamina propria layers. This sophisticated design facilitates the formation of microstructures, closely mirroring the colon's natural architecture and improving the absorption functionality and thereby providing a highly physiologically relevant platform for in-depth exploration of colorectal cancer mechanisms and the evaluation of therapeutic responses. Our model exhibits enhanced cell viability, differentiation, and mechanical integrity compared to conventional models, overcoming previous limitations in biofabrication and establishing a new benchmark for the creation of biomimetic structures. Significantly, our model's heightened fidelity in mimicking the human colon's microenvironment was showcased by its amplified response to 5-fluorouracil, a widely used chemotherapeutic agent. This differential drug responsiveness, when compared to traditional 2D and other 3D models, underscores the critical importance of employing more physiologically accurate systems for preclinical testing. Such insights hold the promise of ushering in more effective treatment modalities for colorectal cancer, bridging the gap between laboratory research and clinical application.

Building upon the significant advancements achieved with our novel three-dimensional colon model, several future directions can be explored to further enhance its applicability and relevance in preclinical research.

A critical step forward involves the incorporation of patient-derived cells into our 3D colon model. By integrating cells directly obtained from patients, the model’s

fidelity to human physiology can be significantly increased. This approach ensures that the cellular diversity and specific genetic variations present in human tissues are accurately represented, thereby improving the model's predictive power for drug efficacy and toxicity. Utilizing patient-derived cells will also enable personalized medicine applications, allowing for the development of tailored therapeutic strategies based on individual patient profiles.

To further replicate the mechanical environment of the native colon, future iterations of our model should include the simulation of shear stress and peristalsis movements. These mechanical forces play a crucial role in the physiological functioning of the colon, influencing cellular behavior, nutrient absorption, and drug metabolism. By incorporating dynamic elements that mimic these movements, we can create a more physiologically relevant model that better simulates the in vivo conditions, thereby providing more accurate insights into disease mechanisms and therapeutic responses.

The human colon is home to a complex and diverse microbiota that plays a pivotal role in health and disease[145]. Future developments should focus on incorporating specific bacterial cultures to accurately reproduce the microbiota environment within the colon model. Understanding the interactions between the gut microbiome and host tissues is essential for studying various gastrointestinal diseases and for developing microbiome-targeted therapies[146]. Cultivating a representative microbiota within the model will provide deeper insights into the role of microbial communities in disease progression and treatment outcomes.

Our 3D colon model presents an excellent platform for advancing drug development strategies. Future research should aim to utilize this model for identifying optimal drug dosages and effective drug combinations. By conducting high-throughput screening and detailed pharmacokinetic and pharmacodynamic studies, we can explore new therapeutic avenues and enhance the efficacy of existing treatments. This approach not only aims to maximize therapeutic outcomes but also seeks to minimize adverse side effects, thereby improving patient quality of life.

In conclusion, our pioneering 3D colon model sets a new standard in preclinical research by providing a highly accurate and scalable platform for studying disease progression and therapeutic interventions. The proposed future directions underscore the potential of this model to evolve further, integrating more complex physiological and biological aspects to enhance its relevance and applicability in precision medicine. By continuing to refine and expand this model, we can make significant strides in understanding colorectal diseases and developing more effective treatments.

2.5 Methods

In this study, gelatin type B, calcium chloride dihydrate, agarose, and ammonium hydroxide were purchased from Fisher Chemical. Pluronic F-127, gum Arabic, alginic acid sodium salt, Triton X-100, and 5-Fluorouracil were purchased from Sigma-Aldrich. Dulbecco's Modified Eagle's Medium (DMEM), fetal bovine serum (FBS), penicillin-streptomycin and trypsin were obtained from Gibco. Live/Dead viability assays were obtained from Invitrogen (CA, USA). Bovine Serum Albumin was obtained from Fisher Bioreagents.

Preparation of gelatin support bath

FRESH support bath was prepared following the procedure reported earlier by Lee et al[95]. In brief, first, 2.0% (w/v) gelatin Type B (Fisher Chemical), 0.25% (w/v) Pluronic F-127 (Sigma-Aldrich), and 0.1% (w/v) Gum Arabic (Sigma-Aldrich) were dissolved in a 50% (v/v) ethanol solution at 45ºC in a 1 L beaker. To form the slurry of gelatin microparticles, the beaker was then placed under an overhead stirrer, sealed with aluminum sheet to minimize evaporation, and allowed to cool to room temperature while stirring for 8 hours. The resulting slurry was then divided into 50 mL conical tubes and centrifuged at 300 g for 5 min to compact the gelatin microparticles. The supernatant was then removed, and gelatin microparticles were resuspended in a washing solution (0.2% (w/v) $CaCl_2$ (Fisher Chemical)) to remove the ethanol and Pluronic F-127. The gelatin slurry was then washed three times with washing solution at 1000 g for 2 min. Prior to printing, the uncompacted slurry was degassed in a vacuum chamber for 15 min, followed by centrifugation at 2000 g for 10 min with the temperature of centrifuge set to 10 °C. The supernatant was removed, and the gelatin slurry was transferred into a print container of appropriate volume, typically 50% larger than the construct to be printed. For sterile support preparation, all hardware was either cleaned with 70% Ethanol and UV sterile inside the biosafety cabinet.

Bioink preparation

Bioinks were prepared by dissolving in a sterile environment GelMA (Advance Biomatrix, USA) in PBS in a concentration of 7.5% (w/v), 0.2% (w/v) of lithium

phenyl-2, 4, 6-trimethylbenzoylphosphinate (LAP) (Allevi, USA) as the photo initiator and 0.5% Alginate(w/v) and homogenizing it by magnetic stirring at 300 rpm overnight.

Characterization of bioink

Rheology

The rheology profile of the GelMA-Alginate bioink was characterized by using a TA DHR-2 Discovery series (TA instruments, United Kingdom) equipped with a Peltier for temperature control. Parallel plate geometry (25 mm) was used with a gap of 0.3 mm. GelMA-Alginate ink is previously tempered at 37 °C before each test. The share rate effect in the viscosity of GelMA was measured at a constant temperature of 25 °C by varying the shear rate between 0.01 and 1000 1/s in the rotational mode. The sweep tests of the GelMA-Algintate ink were evaluated with frequencies ranging from 0.1 to 10 rad s^{-1} at a rotation amplitude of 1 % at 25 °C.

Compressive modulus

To study the compression modulus of the GelMA-Alginate bioink, samples were prepared and molded with a diameter of 15.6 mm and a height of 5 mm. The unconfined compression test was performed using an Instron 3365 UTS testing machine (Norwood, Massachusetts, United States) at room temperature under a compression rate of 200 μm/min. The mechanical properties of compression are obtained from the averaged compression stress-strain curve. The compression modulus was calculated as the slope of the linear region in the 0.1–0.15 strain range of the stress-strain curves.

Cell culture

HCT-116 and Caco-2 were obtained from ATCC, and 3T3 fibroblast was kindly donated by Prof. Benavente. Briefly, cells were cultured in Dulbecco's Modified Eagle's Medium (DMEM). The culture media for both cell lines were supplemented with 10% (v/v) fetal bovine serum (FBS) and 1% (v/v) penicillin-streptomycin. Cells were incubated at 37°C in a 5% CO2 atmosphere.

Cell Culture on Transwell Inserts

Firstly, Transwells inserts (Corning, USA) were incubated in culture media for 2 hours to equilibrate the membrane for seeding. For 2D monocultures, Caco-2 epithelial cells were seeded onto the apical side of 24 mm Transwell inserts as shown in Figure 2.4, at 2.5 x 10^5 cells per well density. The cells are cultured in 1 mL of culture medium in the basolateral compartment and 400 µL into the apical compartment. For co-culture experiments, 3T3 fibroblasts were initially seeded followed by Caco-2 addition. Transwell inserts were initially inverted and seeded with 1 x 10^5 cells in 50 µL of 3T3 medium and incubated for 1 h to encourage cell attachment to the membrane. Thereafter, seeded inserts were returned to wells containing 1 mL of 3T3 medium and grown for 5 days. Four days after fibroblast seeding, inserts were seeded with Caco-2 cells on the apical side as previously described. For 2.5D cultures in Transwell format, firstly, 100 µL of hydrogel with and without embedded 3T3 fibroblast at 5 million per ml is drop casted in 96 well plate and crosslinked for one minute at 405 nm UV exposure, later on, 200 µL of 0.2% $CaCl_2$ is added to the well and let stay for 10 minutes. After crosslinking, the hydrogels are transferred to the apical

side of the Transwell and cultured for 5 days. After day 5, Caco-2 cells at 2.5 x 10^5 cells per well density are seeded on top of the hydrogels with and without 3T3 fibroblasts for mono and co-culture samples. Samples on Transwell inserts were fed every 2–3 days with 1 mL of culture medium in the basolateral compartment and 400 µL into the apical compartment. For some experiments, Transwell inserts seeded only with 3T3 fibroblast on the basolateral side were used and referred to as fibroblast monoculture on Transwell inserts.

3D bioprinting protocol and construct culture

In preparation for printing the double-layer colon model, Colon NIH 3D model is processed to generate a scaled-down computer-aided design (CAD) model (10 mm in length and 5 mm in diameter) composed of two interconnected layers that mimic the cancer tumor and the external epithelium. Later the CAD model was sliced and processed using Cellink HeartWare software (CellInk, USA) to generate the G-code. Bioink formulations were optimized to meet the mechanical properties and cell viability of colon tissues. HCT-116 and 3T3 cells were dispersed respectively at concentrations of 3 x 10^6 and 8 x 10^6 cells/mL, in the early described bioinks. Then, cell-laded bioinks were transferred to extrusion cartridges avoiding the formation of bubbles, and G22 nozzles were attached. To print the colon model, embedding extrusion bioprinting was performed (FRESH method), by using an Inkredible+ bioprinter (CellInk, USA). In preparation, the sterilization of the printer was performed by using ethanol 70%, UV-light, and using the HEPA filter embedded within the printer. Once sterilized, the cartridges were placed inside the printhead along with the reservoir filled with gelatin support bath. The cartridges and needles were

positioned in the XY center of the container. The bioprinting was then started. All colon constructs were printed at 27 °C. Upon bioprint completion, colon constructs were exposed to 405 nm light for 1 minutes to crosslink the GelMA. Later, the container was incubated at 37 °C to melt the gelatin support bath and release the printed colon. Once released, colon constructs were washed with fresh media to remove the melted gelatin support bath, and then cultured.

Construct staining and embedding

Life/death assay

The LIVE/DEAD® assays were conducted following the manufacturer's instructions. Briefly, the culture medium was removed from printed constructs, and two PBS washes were performed to extract the remains of the media. The LIVE/DEAD® reagent was then added to the samples and incubated for 40 min in the incubator, followed by three washes with PBS. Finally, the samples were examined by LSM 900 with Airyscan Microscope (Carl Zeiss, Jena, Germany).

Immunofluorescence staining

Immunostaining was performed by fixing the colon printed samples with 4 Paraformaldehyde (PFA) (Fisher Scientific, Waltham, Massachusetts, United States) for 60 min and 10 minutes for Transwell format samples, followed by two washes with 1x PBS. After washing, Cell permeabilization was done using 0.1 v/v% Triton X-100 in PBS for 20 min and blocking was performed with 3% BSA in PBS to prevent non-specific binding. F-actin cytoskeleton was stained by incubating bioprinted constructs with Alexa Fluor 488 Phalloidin (Thermo Fisher Scientific, USA) (1:40 dilution), tight

junction proteins was stained by Alexa Flour 555 conjugated ZO-1 (Invitrogen, USA) (5 μg/mL in blocking buffer) at 4 °C overnight. The optimal concentration used for antibodies are based on the manufacturer's instructions. Samples were washed with PBS three times and then stained with DAPI for 20 min at room temperature. After washes with PBS, the samples were embedded in agarose gel and sectioned as explained below and were imagined by LSM 900 with Airyscan Microscope (Carl Zeiss, Jena, Germany) and Z.1 lightsheet microscopy (Carl Zeiss, Jena, Germany).

Agarose embedding

For fluorescence microscopy imaging, the printed colons require to be sliced in small cross-sections. To provide mechanical support during the cutting, the stained colon printed constructs were embedded in agarose. Briefly, agarose was dissolved in distilled water to produce a 1% w/v solution at 60 °C under magnetic stirring for 2 h. Once dissolved, agarose was cold down to 40 °C for embedding. The barrel and plunger of a 3 mL syringe were disarmed. The stained colon construct was gently placed inside the barrel with the help of a spatula, and the plunger was carefully re-inserted to not damage the sample. Agarose was then absorbed slowly until covering the full construct, then the syringe was placed vertically until the agarose solidified. The top of the syringe was cut to release the stained embedded colon sample. Finally, surgical blader was then used to slice the embedded construct.

Electrode and chamber fabrication

To ensure uniform spacing between electrodes, a specialized chamber was designed to house both the reference electrode (RE) and the working electrode (WE). Utilizing Solidworks (Solidworks Corp., USA), the chamber was conceptualized as a cylindrical structure with an inner diameter (DI) of 6 mm and a height of 10 mm. The upper section of the chamber serves as a lid, incorporating a central aperture designed to secure the second electrode, which has a DI of 4 mm. The design facilitates a key-and-lock mechanism between the lid and the chamber body, ensuring the electrodes' positions remain stable throughout the measurement process. Details of the chamber's design, including specific dimensions, are provided in Figure 2.16. The fabrication process of the chamber involved 3D printing using a LumenX digital light processing printer (Cellink, USA) with a plastic resin. The design was prepared for printing by slicing it into layers with a height of 100 μm. Post-printing, both the chamber and lid underwent a thorough cleaning to remove any residual resin, followed by ultraviolet curing to ensure complete solidification. Subsequently, the chamber was affixed to a petri dish using adhesive and allowed to dry overnight. For the electrodes, a PI-Gold flexible sheet (KOYE Technology, China) was used, which was precisely cut using cutter plotter and folded to fit within the chamber and through the lid's aperture. To enhance adhesion between the electrodes and their respective surfaces, double-sided tape was employed. This methodological approach ensures a consistent and reliable setup for electrochemical measurements, highlighting the precision and care taken in the fabrication of the experimental apparatus.

Measurement of transepithelial electrical resistance (TEER)

The TEER of both Caco-2 cell monoculture and Caco-2/3T3 co-culture cell models housed in 24-well Transwell inserts was measured using an EVOM (World Precision Instruments, USA). A blank Transwell insert with no cells and only hydrogel served as a blank control for the mono-culture model whilst a Transwell insert with 3T3 cells with and without hydrogel layer served as a blank control for the co-culture model. TEER values ($\Omega.cm^2$) of cell models were calculated using Equation (1)

$$TEER = (R - R_{blank})A$$

(1) where R is the resistance measured across the cell layer(s), R_{blank} is the resistance of a blank as explained earlier, and A is the surface area of a Transwell insert (0.33 cm^2).

For the 3D colon construct measurements, firstly the fabricated electrode and chamber are sterilized using 70% Ethanol and UV sterilized for 30 minutes. Then the electrodes are connected to potentiostat (VersaSTAT 3, Princeton Applied Research) in two-electrode measurement setup, the applied DC voltage between to two electrodes is set to 0 and 0.01 V Ac voltage is applied for the measurements. After that, 1X PBS is used to check the stability of the setup and data is recorded from 1 Hz to 10^6 Hz. After that, the samples without Caco-2 cells are measured as the blank measurements and later on the colon sample with Caco-2 cell are measured through culture time from day 4 to day 21. The impedance differences associated with the growth of Caco-2 cells is calculated based on the averaged difference between black

and sample at 10 Hz to 1 kHz. The values are multiplied by surface area of lumen part of the colon (1.25 cm^2) to find the resistivity of the caco-2 layer.

Hanging-Drop method for Spheroid formation

HCT116 spheroids were generated using the hanging-drop technique. Briefly, a concentration of 5 x 10^4 cells/drop was used. Drops of 52 μL were deposited in a petri dish and carefully flipped to produce a hanging drop meniscus, as depicted by Figure 2.14. To avoid evaporation 4 mL of PBS was added into the lid, and the petri dish was sealed with parafilm. The spheroids were cultured in an incubator, and their growth was monitored daily with an inverted microscope through culture (Figure 2.14). The size distribution of the spheroid was analyzed from optical microscopy images.

Metabolic activity analyses

The metabolic activity of the cells contained in the colon constructs were evaluated at days 0, 1, 2 and 3 of drug exposure. The samples were incubated with 10% (v/v) of Resazurin reagent (R&D Systems, USA) in EMEM media for 2 h at 37 C. Then the supernatant was collected and replaced for control samples with fresh culture media and for treated samples with media + drug. The fluorescence of the supernatant was measured at an excitation wavelength of 530 nm and an emission wavelength of 590 nm with microplate reader (BioTek Cytation 5, Agilent).

Statistical analysis

The statistical analysis was conducted using analysis of variance (ANOVA) in Python script. *p*-Values (*$p < 0.05$, **$p < 0.005$, and ***$p < 0.0005$) were considered to

be statistically significant. The data were presented with standard deviation of at least triplicate experiments.

2.6 Supporting Information

2.6.1 Note 1 | Rheological behavior of four ink candidates

The rheological properties of bioink formulations comprising 5% and 7.5% GelMA, and those augmented with alginate (0.25% and 0.5% in 7.5% GelMA), were meticulously evaluated. Figure 2.6A illustrates the inherent shear thinning behavior of all bioink candidates, characterized by a viscosity decrement in response to escalating shear rates. This non-Newtonian fluid property is essential for extrusion-based 3D printing, ensuring optimal printability through fine nozzles and guaranteeing the structural integrity of the resulting constructs via prompt solidification. Initial viscosity measurements at a shear rate of approximately 10 s^{-1} and a temperature of roughly 22°C yielded viscosities of 0.27, 0.30, 0.41, and 0.95 Pa s for GelMA 5%, GelMA 7.5%, GelMA 7.5% with 0.25% Alginate, and GelMA 7.5% with 0.5% Alginate, respectively. These viscosities correlate directly with the increment in GelMA concentration and the integration of Alginate, serving as a rheological modifier. Further, the gelation kinetics of these inks were scrutinized by methodically diminishing the temperature at a uniform rate of 1°C per minute. The modified GelMA formulations, specifically those with alginate, manifested a pronounced increase in viscosity near 20°C, diverging from the unmodified GelMA 5%, which exhibited a comparable viscosity augmentation at approximately 16°C. These findings accentuate the distinctive gelation thresholds and viscosity responses of the bioinks in question

(Figure 2.6B). Moreover, our analysis included an assessment of the storage modulus (G') and loss modulus (G") over a range of oscillatory frequencies. The results indicated a dependency of both moduli on the frequency of oscillation, with alginate presence enhancing these rheological parameters. Consequently, this implies that alginate incorporation enables the fine-tuning of GelMA hydrogels' mechanical and viscoelastic characteristics, amplifying their applicability in bespoke bioprinting endeavors where precision-engineered material properties are imperative (Figure 2.6C).

2.6.2 Note 2 | Quantitative analysis for comparison of 3D printed colon and 3D colon model images

To rigorously evaluate the fidelity of 3D printed constructs relative to their original digital 3D models, we developed and applied a detailed image processing and analysis methodology, utilizing the Python programming environment and leveraging libraries such as scikit-image for image manipulation tasks and numpy for numerical analysis. This process commenced with the collection and preprocessing of digital images of the 3D printed constructs and their 3D model counterparts. To ensure a focused analysis on structural integrity rather than color discrepancies, images were converted to grayscale, thus standardizing the dataset for subsequent operations. Critical to our analysis was the precise alignment of images for direct comparison, achieved through a bespoke image shifting technique grounded in the Fourier Shift Theorem. This technique involved the application of a 2D Fourier transform to

compute the image's frequency spectrum, followed by a phase shift to achieve the desired alignment, and an inverse Fourier transform to return the image to its spatial domain, thereby allowing for sub-pixel precision in aligning the images to a common orientation and scale. The effectiveness of our approach was evidenced by visual comparisons, with difference images generated to visually depict the discrepancies between the printed constructs and the 3D models (Figure 2.7A). The quantitative assessment of the 3D printed constructs against the original models was conducted using two key metrics: the Structural Similarity Index (SSIM) and Mean Squared Error (MSE). SSIM was utilized to measure the similarity between the two images in terms of contrast, luminance, and structural information, offering a nuanced view of the perceived quality of the printed constructs. Conversely, MSE provided a straightforward, quantitative measure of the average squared difference between the pixel intensities of the comparative images, serving as an indicator of the absolute error across the images. Our methodology yielded high SSIM values, indicating a high degree of structural and visual similarity between the printed constructs and their original 3D models, while low MSE values highlighted the minimal discrepancies, thus validating the precision and accuracy of our 3D printing process (Figure 2.7B). This comprehensive analysis not only demonstrated the high fidelity of our 3D printed constructs but also contributed significantly to the understanding of the capabilities and limitations of current 3D printing technology in accurately replicating detailed and complex structures. Through this process, our study underscores the potential and precision of advanced 3D printing techniques, offering valuable insights and methodologies for future research and application in the field.

2.6.3 Note 3 | 3T3 fibroblast growth dynamics in different ink composition

In recent decades, hydrogel biomaterial platforms have facilitated the exploration of cell-matrix interactions within environments that closely mimic physiological conditions, distinct from the traditional tissue culture plastic, which lacks the complex and potentially confounding biological signals found in vivo. Such advancements have led to the elucidation of the role of mechanical stimuli, such as the elastic modulus or stiffness of the substrate, in directly influencing fibroblast activation. Therefore, we have investigated different ink composition including GelMA 7.5% with Alginate 0.25%, GelMA 7.5% with Alginate 0.5%, GelMA 5% with Alginate 0.5%, and GelMA 7.5% with Alginate 1% on fibroblast cell morphology, aggregation, and network formation. As depicted in Figure 2.9, phase contrast images of different hydrogels with 8 million per ml of 3T3 fibroblast embedded in reveal that higher concentration of GelMA coupled with lower Alginate concentration favors less cell clustering and promotes the formation of planar and elongated fibroblast networks.

2.6.4 Note 4 | Electrode Chamber Fabrication

To ensure uniform spacing between electrodes, a specialized chamber was designed to house both the reference electrode (RE) and the working electrode (WE). Utilizing Solidworks (Solidworks Corp., USA), the chamber was conceptualized as a cylindrical structure with an inner diameter (DI) of 6 mm and a height of 10 mm. The upper section of the chamber serves as a lid, incorporating a central aperture designed to secure the second electrode, which has a DI of 4 mm. The design facilitates a key-

and-lock mechanism between the lid and the chamber body, ensuring the electrodes' positions remain stable throughout the measurement process. Details of the chamber's design, including specific dimensions, are provided in Figure 2.16. The fabrication process of the chamber involved 3D printing using a LumenX digital light processing printer (Cellink, USA) with a plastic resin. The design was prepared for printing by slicing it into layers with a height of 100 µm. Post-printing, both the chamber and lid underwent a thorough cleaning to remove any residual resin, followed by ultraviolet curing to ensure complete solidification.

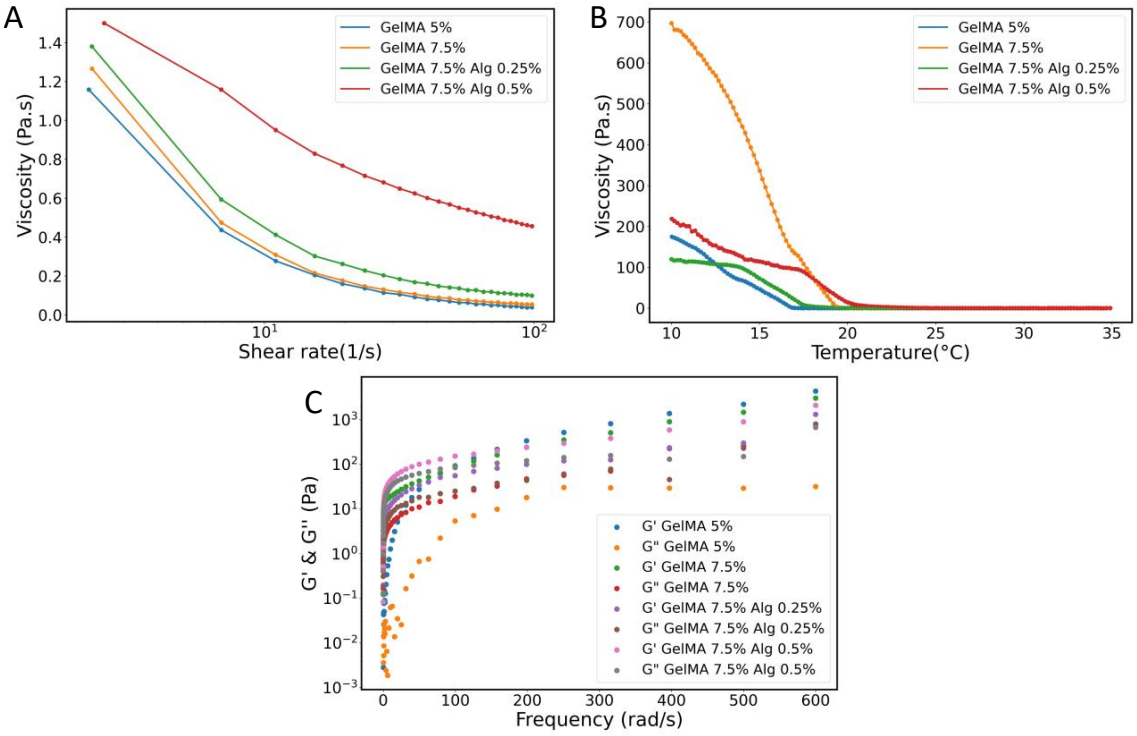

Figure 2.6 Rheological properties of four bioinks. (A) Viscosity of GelMA 5%, GelMA 7.5%, GelMA 7.5%+ Alginate 0.25%, and GelMA 7.5%+ Alginate 0.5% bioinks as a function of shear rate. (B) Temperature dependence of viscosity of bioinks with different shear rate. (C) Storage modulus, G′, and loss modulus, G″, of bioinks formulations as a function of frequency.

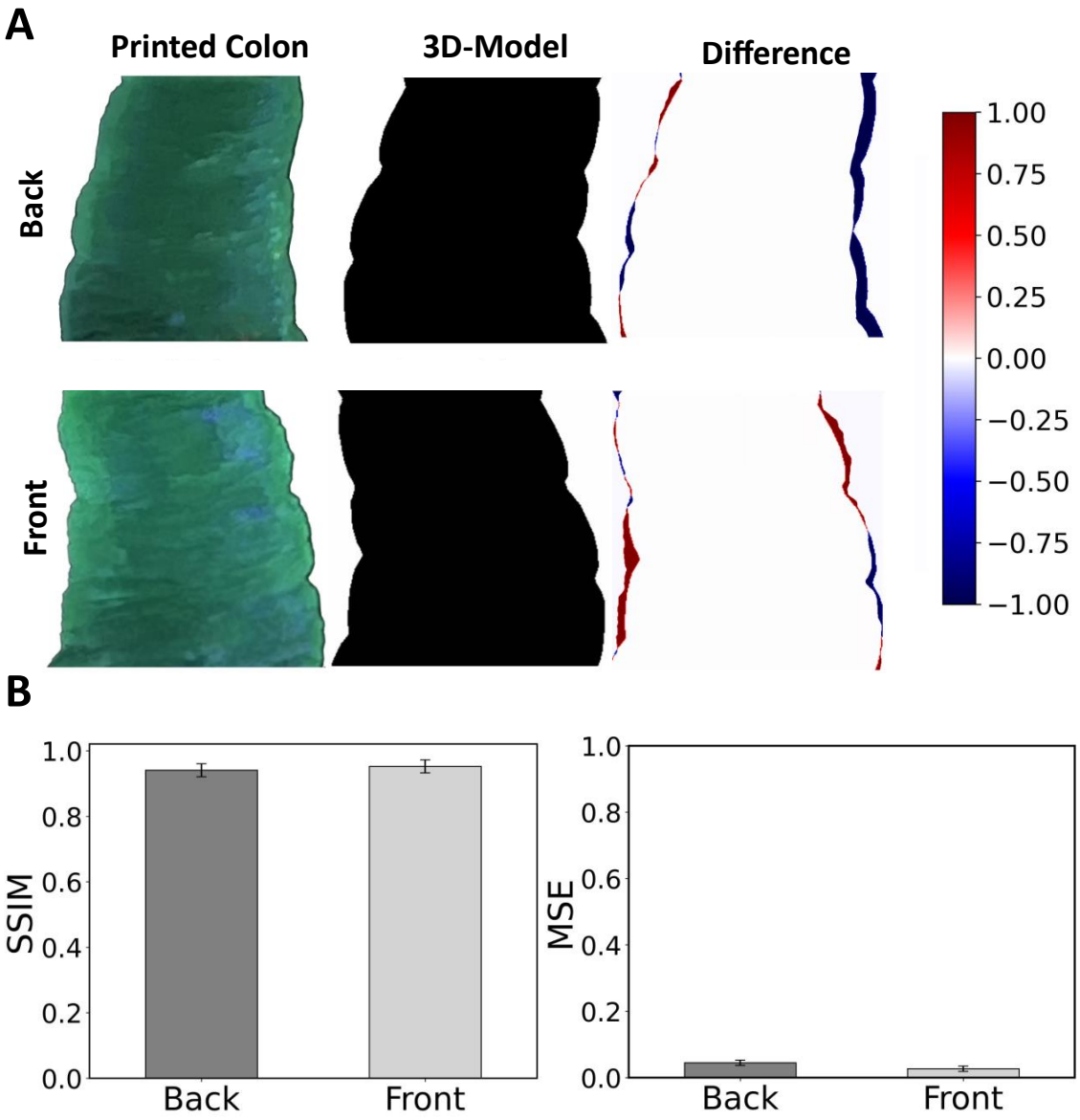

Figure 2.7 Quantitative Comparison of 3D Printed Construct and NIH 3D Model Images. (A) Top row displays the back view of printed colon and 3D colon model image, while the bottom row shows the front view. The color map indicates the degree of similarity, with blue representing negative differences and red indicating positive differences. (B) Presents a bar graph of the comparison metrics: SSIM (Structural Similarity Index) and MSE (Mean Squared Error), for both views. Error bars represent the variability within the measurements.

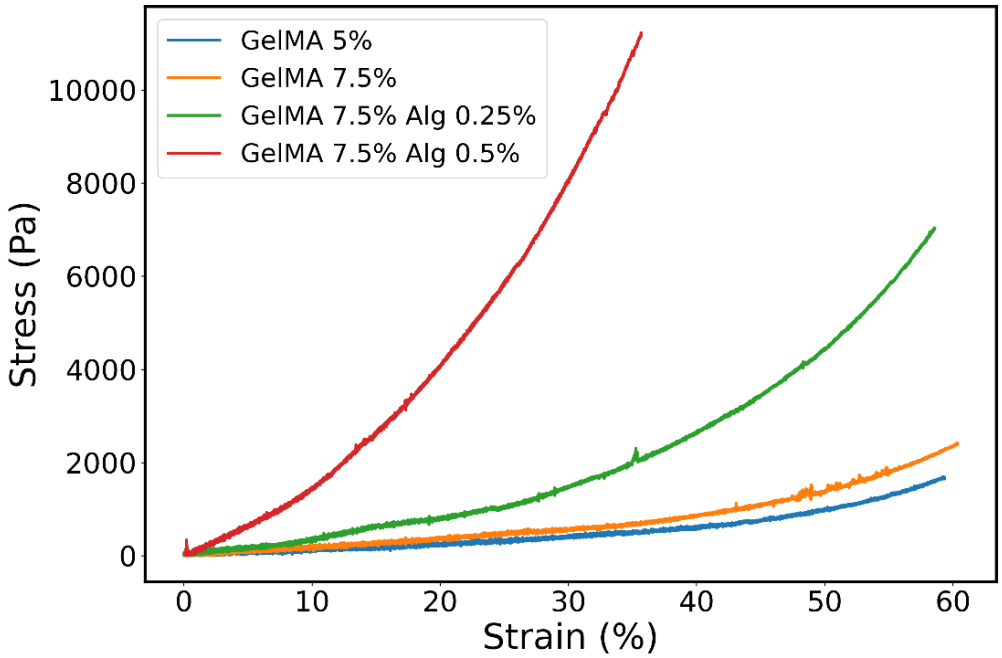

Figure 2.8 A stress–strain curve was obtained through compression testing of four bioink formulations (GelMA 5%, GelMA 7.5%, GelMA 7.5%+ Alginate 0.25%, and GelMA 7.5%+ Alginate 0.5% composite hydrogels.

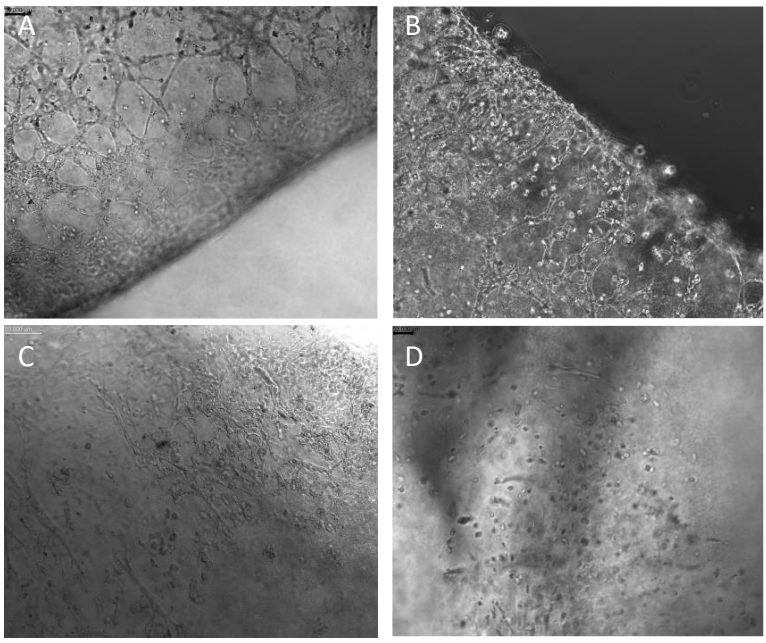

Figure 2.9 Morphological assessment of 3T3 fibroblast behavior in various hydrogel compositions over 5 days. (A) GelMA 7.5% with Alginate 0.25%, (B) GelMA 7.5% with Alginate 0.5%, (C) GelMA 5% with Alginate 0.5%, and (D) GelMA 7.5% with Alginate 1%. Phase contrast microscopy reveals the influence of hydrogel composition on cell morphology,

aggregation, and network formation. Higher GelMA concentration coupled with lower Alginate concentration favors less cell clustering and promotes the formation of planar and elongated fibroblast networks.

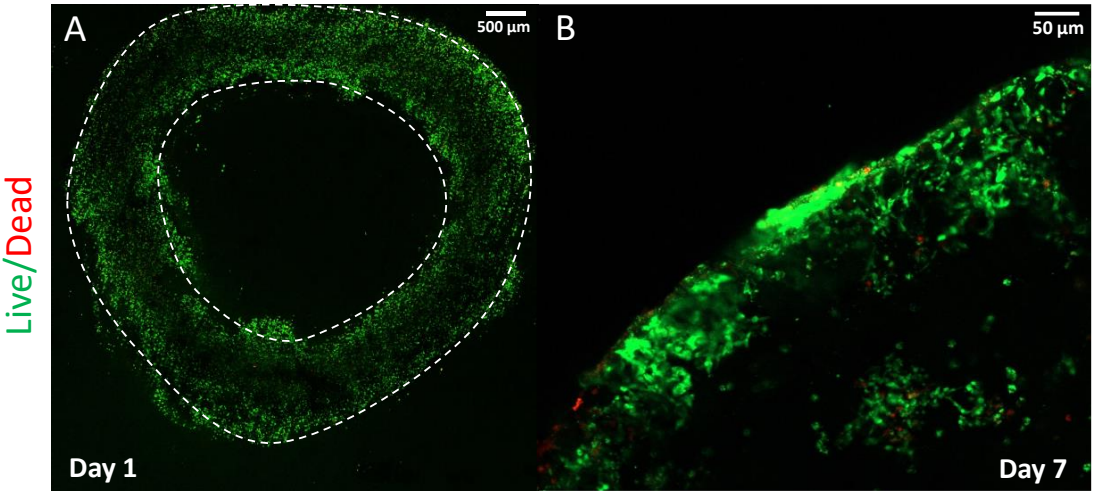

Figure 2.10 3D bioprinting of 3T3 cell-laden colon structure. (A) A representative image of live/dead stained 3T3 cells within the 3D bioprinted colon construct on day 1. Representative live/dead images showing the distribution and spreading of 3T3 cells in the 3D bioprinted constructs (B) on day 7 post-printing.

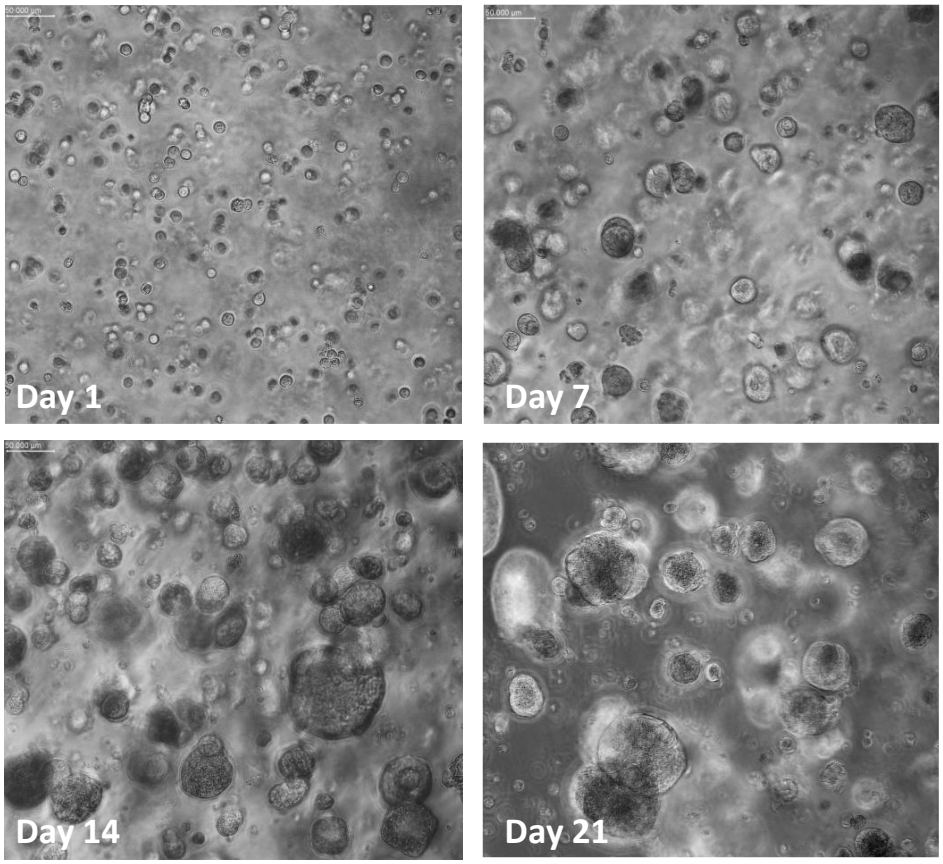

Figure 2.11 Progressive development of cellular spheroids over 21 days in 3D hydrogel culture. Phase contrast images of HCT 116 cells embedded in GelMA/Alginate hydrogel over 21 days, showing single-cell dispersion (Day 1), aggregation (Day 3), and mature spheroid formation (Day 7), These images demonstrate the morphological changes as the cells transition from a single-cell suspension to a multicellular spheroid configuration while cultured in 3D, scale bar: 50 μm.

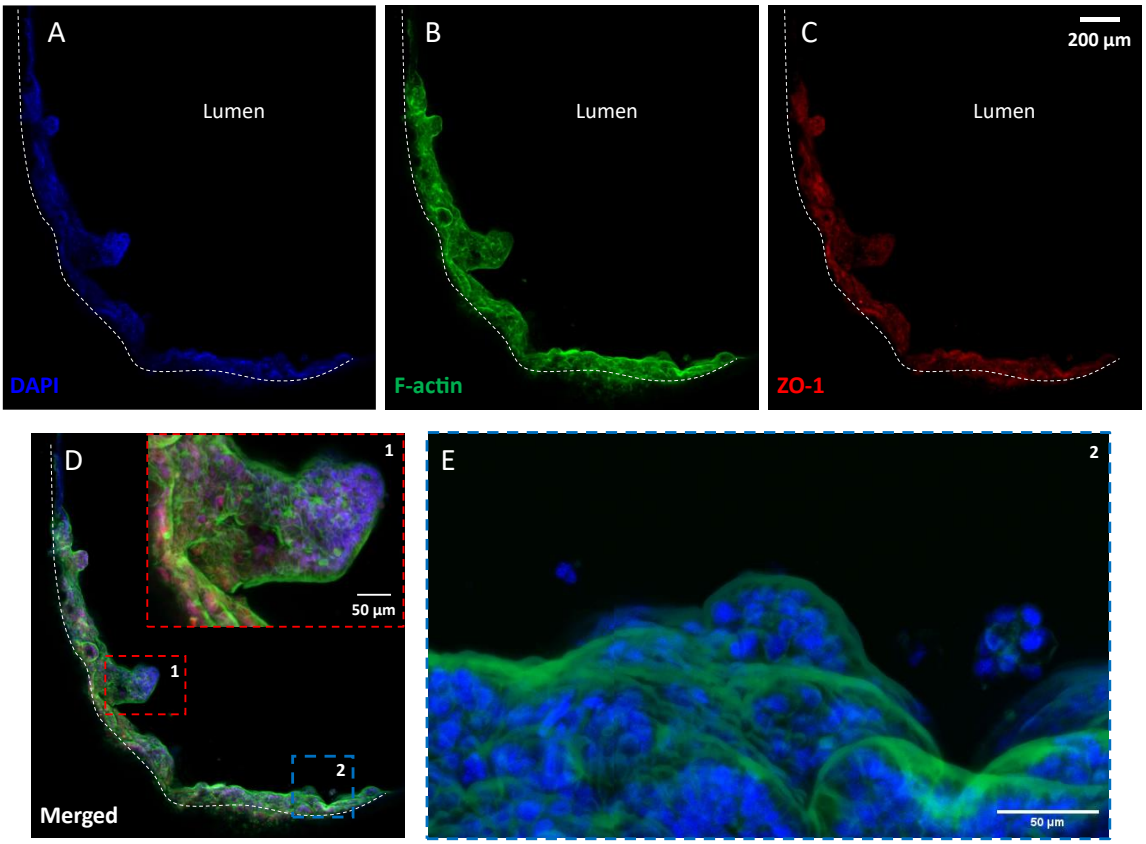

Figure 2.12 Immunofluorescence characterization of intestinal epithelium layer in a 3D scaffold. (A-C) Fluorescent staining of a cross-section of the scaffold shows the expression of ZO-1 (red), F-actin (green), and cell nuclei (blue), highlighting the establishment of a polarized epithelial layer. (D) Merged image of the fluorescent markers within the scaffold, the quantitative assessment of epithelium height across the 3D model, has been measured in respect to the dashed white line presented. The inset (E) provides a magnified view of the differentiated epithelial cells, illustrating the formation of micro-protrusions. The images confirm the presence of tight junctions and the epithelial layer's compactness.

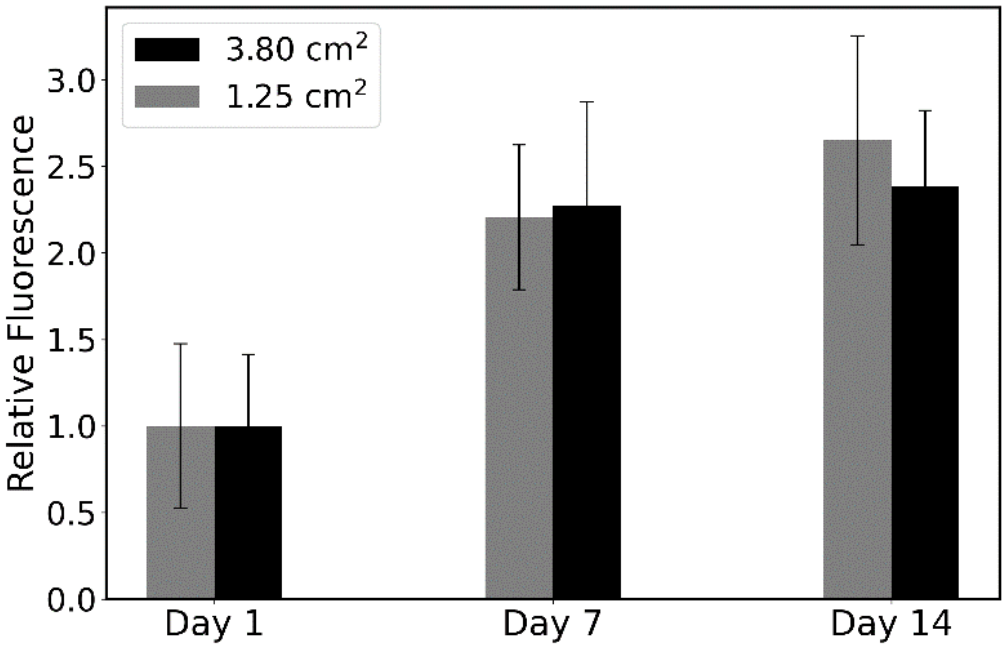

Figure 2.13 Relative fluorescence indicating metabolic activity of 3T3 fibroblast cells cultured on gold electrodes of two different sizes (3.80 cm^2 and 1.25 cm^2) over a period of 14 days. Data are presented as mean ± standard deviation, obtained from three independent biological replicates, to assess the biocompatibility of the electrodes at time points of days 1, 7, and 14.

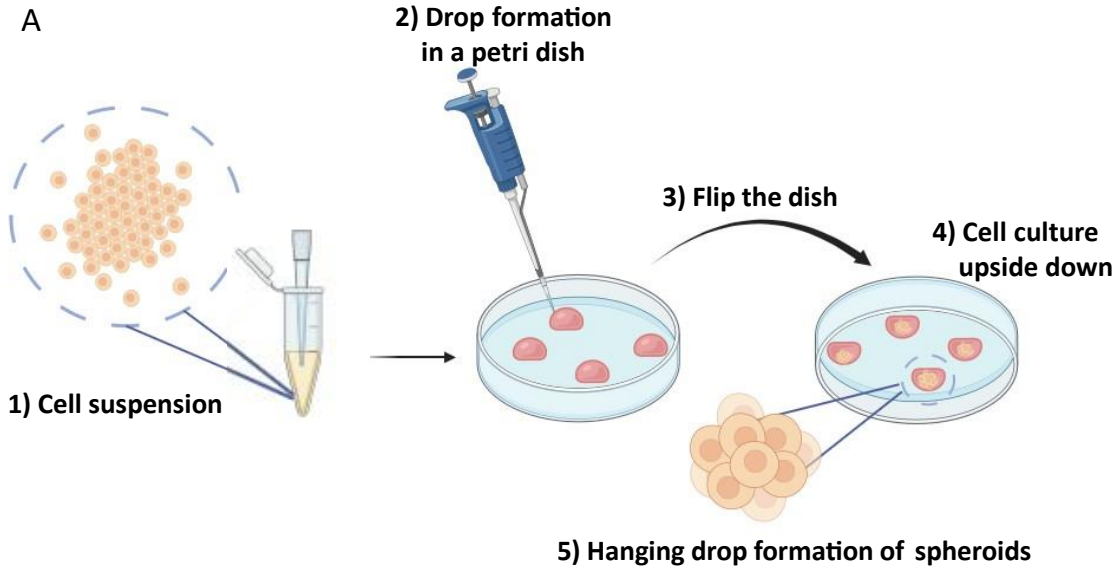

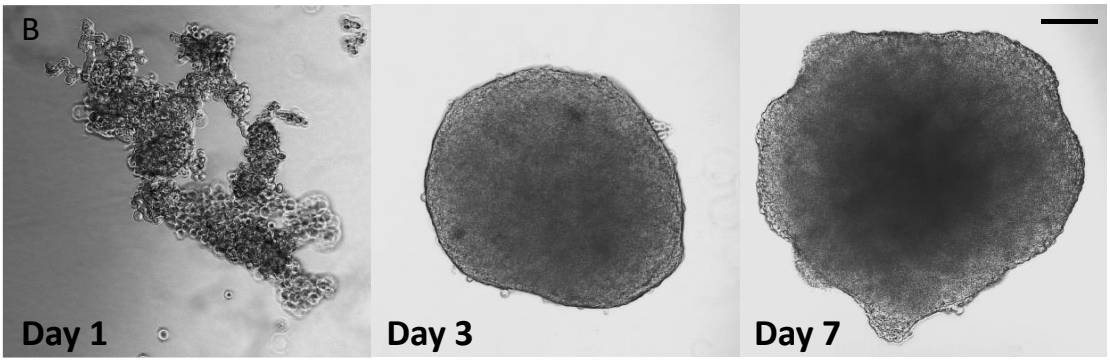

Figure 2.14 Formation and growth progression of HCT116 spheroids via the hanging-drop method. A) Schematic representation of the technique illustrating the preparation and inversion of drops to facilitate spheroid formation. B) Sequential images captured by an inverted microscope showing the development of spheroids on days 1, 3, and 7, with initial cell seeding at 5 x 10^4 cells per drop.

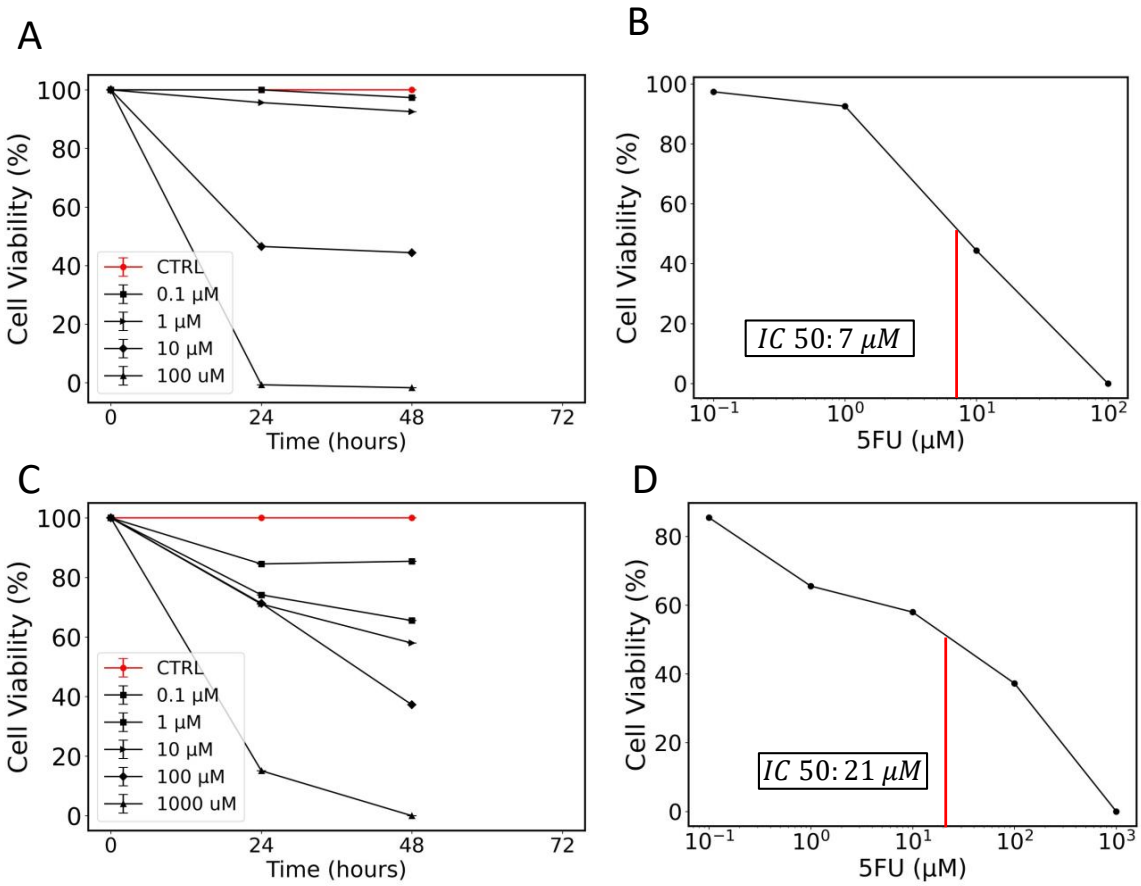

Figure 2.15 Drug efficacy study for HCT116 cell monoculture and 3D spheroid in well plate format. (A) Dose-dependent cell viability of the HCT116 monoculture over time upon 5FU treatment at 0.1-1-10-100 µM. (B) Determination of IC50 value for the HCT116 monoculture by non-linear regression. (C) Cell viability of the 3D spheroid model over time with varying concentrations of 5FU, at 0.1-1-10-100-1000 µM. (D) IC50 value estimation for the 3D spheroid model, indicating an increase compared to the monoculture model.

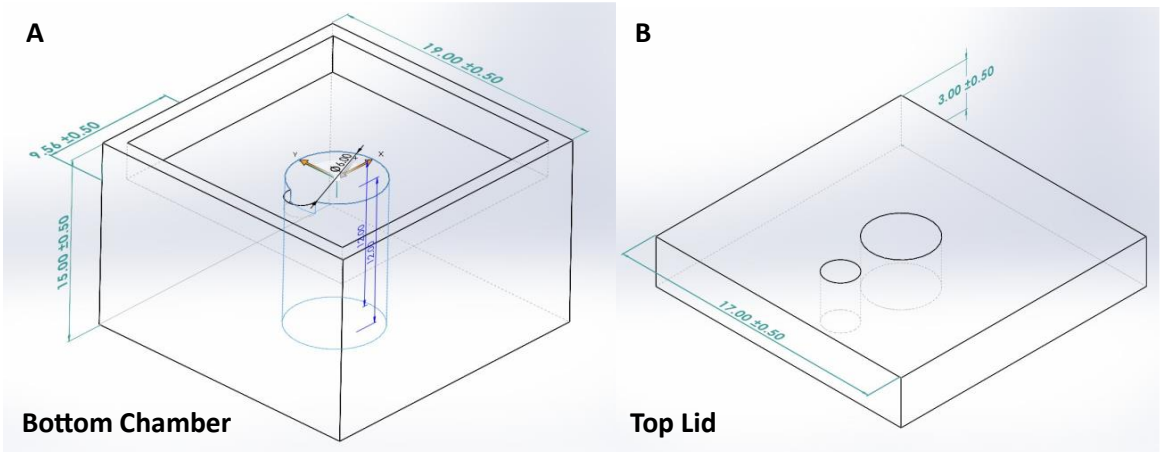

Figure 2.16 Design of Electrode Chamber, bottom and top for TEER measurement in 3D colon constructs, assembled as key and lock configuration. (A) Bottom chamber design hosting the first gold electrode. (B) Top lid accommodating the second electrode in the center.

Chapter 3 : An *in-vivo*-mimicking 3D Lung cancer-on-a-chip model to study the effect of external stimulus on the progress and inhibition of cancer metastasis

3.1 Introduction

Non-small cell lung cancer (NSCLC) accounts for ~85% of all lung cancer cases in the United States, with a 5-year survival rate of ~15% [147]that is further reduced to <5% [148][2] in the case of metastatic lung cancer. The high probability that NSCLC is detected at advanced stages and the absence of systematic treatment approaches made it essential to investigate the underlying disease mechanisms in order to identify and validate the most potent treatment approaches to improve patient survival [149]. In recent years, organ-on-a-chip perfusion culture models have demonstrated superiority over genetically diverse in vivo animal models, as well as traditional two-dimensional (2D) and disordered three-dimensional (3D) static in vitro culture models, in the study of epithelial-to-mesenchymal transition (EMT) markers.

Although decades are passed after the identification of the lung cancer severity, most models remain limited to the culture of 2D monolayer lung epithelial cells. Also, 3D planner culture models with air-liquid interfaces were also evaluated [150], [151], [152]. Over the years, many researchers investigated the mechanism to elucidate the effect of cigarette smoke extract (CSE) on the healthy lung cells [153], [154], [155]. The present work emphasizes on the enhanced possibility of lung cancer metastasis

upon exposure to cigarette smoke extract. Although the topic has been studied and recognized by researchers over the decades, there is a scarcity of such well representative models which can potentially identify the possible effects of cigarette smoke for different smoking scenarios on the initiation and advancement of metastatic lung cancer in-vitro. In the present work the physical, mechanical, and biological features of the cancer microenvironment are critically considered. In this regard, the effectivity of a 3D in-vitro culture model to represent the dynamic cancer microenvironment is accepted as an important design consideration for constructing lung-cancer-on-a-chip models[156], [157]. To address this phenomenon, the inclusion of 3D bioprinting technology, as a fabrication process of 3D cancer microenvironment, offers a computer-controlled, simple yet versatile technique to position cells to the desired architecture.

In the past decades, the co-culture of stromal cells with lung epithelial cells in microengineered devices containing parallel channels, and separated by an extracellular matrix–derived protein-coated porous membrane, has attracted significant attention to the in-vitro modeling of lung diseases. It showed the ability to recreate many in-vivo features including breathing conditions by adding parallel channels in both sides of the cell-culture chambers. This phenomenon results in mechanical forces on the cultured cells that resembles the native lung milieu. Xu et al. applied this device to model lung cancer metastasis in-vitro along with integration with three other organ-specific cells i.e. liver (hepatocytes), brain (astrocytes) and bone (osteocytes). The device showed upregulation of functional markers

representing damage of conjugated organs due to lung cancer metastasis [158]. Such devices were validated for EMT markers and further evaluated for drug resistance of lung cancer cells[159], [160], [161]. Although these models have proven superior compared to the physiologically inferior 2D models and static 3D culture models, they include complex methodologies and stiff materials made of synthetic polymers with physiologically different mechanical properties to culture human lung cells. The model lacks 3D features of the scaffolds to replicate the 3D in-vivo mimicking physiochemical characteristics, which plays an essential role in the functional maintenance of cells in-vitro. Furthermore, the 2D culture of human lung cancer cells lacks the biological complexity of the in-vivo counterpart processes[162], [163], [164], [165], [166], [167], [168]. These limitations may yield misleading assessments of disease conditions and inferior estimation of drug doses [169].

The present work introduces and reports the development of an in-vivo–mimicking 3D-lung cancer-on-a-chip (IVM3DLCOC) system for modelling human lung diseases in-vitro. The proposed model is designed to mimic the physical, mechanical, and biological characteristics of the human lung. Physiologically relevant media flow, pseudo-respiration including exhalation/inhalation, and an air-liquid interface are intended to provide physical cues. Gelatin methacryloyl (GelMA) hydrogel, a proven material for maintaining primary human alveolar epithelial cells (hAECs) [170], is used to 3D bioprint the lung cancer cells along with associated stromal cells inside the fluidic channels to the desired shape, which facilitates cell-cell and cell-matrix interactions and replicates the mechanical and biological cues of the human lung.

Polydimethylsiloxane (PDMS), which is a highly biocompatible, chemically stable, transparent material possess high gas permeability and mechanical stability [171], [172], [173], [174] is used to fabricate the fluidic channels. These fluidic channels are connected to an air channel through a porous membrane for systematic application of inhalation and exhalation along with an air-liquid interface to the lung epithelial cells to mimic the in-vivo microenvironment. Rapid prototyping, conventionally termed 3D bioprinting, was used to biofabricate the multilayer and multistage IVM3DLCOC model [175]. Thus, the newly developed model is an all-inclusive unit contacting cell constructs along with the lung's representative air and fluid compartments, efficiently prototyped using a single tool. The bioprinter used here is able to print biomaterials with and without human cells to a predesigned 3D architecture [176]. This biofabricated IVM3DLCOC model was then fully characterized and validated for disease modelling in studies of cigarette smoke extract (CSE)-induced lung cancer metastasis, and in dose-dependent evaluation of drug efficacy. Cigarette smoke (which contains more than 69 different types of carcinogens, including nicotine, nickel, cadmium, ammonia, and nitrosamines, e.g., 4-(methylnitrosamino)-1-(3-pyridyl)-1-butanone[177] is recognized as the most common accelerator of lung cancer metastasis, through enhancing the invasiveness of cancer cells [178], [179]. To date, the pathophysiology in the progression of CSE-induced metastatic lung cancer has been investigated using different animal-based in-vivo models [180], [181], [182], [183]. However, such in-vivo models are unreliable for analyzing disease mechanisms in co-relation with human pathophysiology due to genotypic dissimilarity [184] and the natural aversion of rodents to smoking. This results in >90% failure of preclinically

tested drugs in clinical trials on human patients [185], causing the loss of millions of dollars each year [186]. In contrast, our IVM3DLCOC model is ideally suited to the study of CSE-induced metastatic lung cancer in-vitro. A549 cells, a widely known model lung adenocarcinoma cells, and a model cell for in-vitro representation of type II pulmonary epithelial cell [187], [188] along with human lung fibroblast are applied. The nature of this applied lung cancer cell line (A549) enables the detailed in-vitro investigation of the biosynthesis and secretion of complex lipoprotein materials[189], [190]. The current model is intended to analyze the effect of the external stimulus on the progress and inhibition of lung cancer in the presence of the stromal cells. Fibroblasts are the major stromal cells present in solid tumours and are the key component of the tumor microenvironment. They adapt a myofibroblastic phenotype in the presence of cancer cells [191]. With an increase in α-SMA expression, fibroblasts can also enhance the invasiveness of metastatic cancer cells [192]. It was observed that tobacco exposure to the fibroblasts could result in disruption of the epithelial cell-cell interactions and further can influence epithelial migration and proliferation [193]. Cigarette smoke extract can induce the formation of different reactive oxygen species (ROS) due to the generation of oxidative stress, which can impair the normal functional properties of the lung fibroblasts. Reportedly CSE can result in the decrease of glutathione levels and can weaken superoxide dismutase activity, thus promoting the oxidative stress generation in lung fibroblasts [194]. Thus, the current model includes human lung fibroblasts along with A549 cells to model metastatic lung cancer to create an in-vivo mimicking cancer microenvironment. Cell constructs are maintained by diffusion flow generated by well-controlled flow gradients between the

media reservoirs. The biofabricated IVM3DLCOC model is suited to the study of two different CSE exposures: for the heavy smoker (i.e., 20 cigarettes/day) and light smoker (i.e., 10 cigarettes/day), with different exposure times (24, 48, and 72 h). The EMT markers, including N-Cadherin (N-Cad) for the metastatic invasiveness of A549 and fibroblast activation marker (alpha-smooth muscle action, α-SMA) of human lung fibroblasts (HLFs), are monitored along with translational markers such as secretion of interleukin-6 (IL-6). Additionally, to further validate our IVM3DLCOC model and demonstrate its utility for drug efficacy evaluations, a dose-dependent study on the effect of paclitaxel, an FDA approved model chemotherapeutic drug[195], [196], [197] on the cancerous cells of the model was successfully performed.

In brief, our in-vivo mimicking 3D lung-cancer-on-a-chip model has been successfully developed and validated to preserve the function of human lung cells in 3D under disease and normal conditions by providing essential in-vivo features such as an air-liquid interface to the lung epithelial cells, inclusion of artificial breathing and diffusion control flow through the barrier of stromal cells, and both mechanical and biological cues to the cell-laden bioprinted human lung tissue. The model is then fully characterized and its utility for disease modelling and drug efficacy evaluations is demonstrated on two model studies, i.e., CSE lung cancer metastasis and dose-dependent effect of chemotherapeutic agents. Our biofabricated model is likely to find further applications for the analysis of underlying disease mechanisms and for screening potential drug's efficacy.

3.2 Results and discussion

3.2.1 Design and Fabrication of IVM3DLCOC

In-vitro lung models with the capability to stimulate biophysiological and biochemical responses towards foreign molecules similar to those seen in-vivo, either a disease-causing element or a material with therapeutic potential capabilities, are now much sought after to find effective solutions and to decode underlying disease mechanisms in respiratory diseases. Herein, we describe the design and testing of a 3D-lung- cancer-on-a-chip (IVM3DLCOC) model that mimics the positioning of lung cancer cells inside the stromal cell barrier, protected from shear flow, with controlled diffusive transport of nutrients, oxygen, and drug (Figure 3.1A,1C). Diffusion is generated by the concentration gradient in the cell chamber and kept constant by the main media stream circulation between the two reservoirs. To model and properly understand the distribution of concentrated species, we employed a computational model (COMSOL) to simulate the distribution of flow rate, oxygen level, nicotine, and added drug concentrations in our model (Figure 3.1F, 1G). The cross-section of microchannels creates a fluidic resistance in the cell culture area 10 times greater than that realized through the media channel (represented by the flow rate profile in Figure 3.1F), further confirming that the transport of media would be purely diffusive at a lower speed in the cell chamber ($\sim 2\times10^{(-4)}$ mm/s). Here, we assumed that the cell distribution is homogeneous inside the GelMA hydrogels, and hydrogels are assumed to be semi-solids. Therefore, the flow rate within the hydrogel is set as zero and considered to be only diffusion induced around the hydrogel [198]. The transport of

small molecules like nicotine and drug within the cell chamber was considered to be completely through diffusion, which was simulated with an inlet concentration of 1 mol/m^3, after zero initial concentration in the IVM3DLCOC model, a diffusion coefficient of $1.0 \times 10^{(-9)}$ m^2 /s in culture media, and no cell uptake or flux through the walls, with a velocity of $5 \times 10^{(-6)}$ m/s (Figure 3.1F,1G) as the inlet velocity. The simulation results show that it takes ~5 hours to reach a stable concentration throughout the cell chamber. In addition, our IVM3DLCOC model offers close replication of the diffusion control flow of media and essential biomolecules towards 3D bioprinted lung cells. It is already well known that the fluid moves inside the cellular environments through diffusion and cross the semipermeable membranes by osmosis [199]. In this reported research, the presence of media reservoirs at the perpendicular direction (Figure 3.1E), leads to restricted flow towards the cell chamber and induce more diffusion-controlled flow to mimic the in-vivo features of fluid movement. This facilities the in-vivo–mimicking gradient flow of essential nutrients inside the cell construct [200]. COMSOL simulation also indicated that the applied media flow creates diffusion of the media through the constructs at a physiologically relevant rate, which is necessary for superior in-vitro cell maintenance. Because the air-liquid interface present at the lung epithelium is a major regulator of the cell microenvironment[201], it has been replicated in our biofabricated IVM3DLCOC model with an inhalation and exhalation feature.

3D PDMS printing was successfully applied to print the three layers of the lung-model fluidic-system, i.e. (i) an air channel integrated with a spin-coated PDMS layer, (ii) a porous layer, and (iii) media reservoirs with cell holding unit (Figure 3.1D). The

lung-model fluidic system is integrated after printing all the layers using a corona discharge machine. The bottom-most layer consists of the cell chamber, media reservoirs, and microchannels for media flow, printed on a glass substrate (Figure 3.1J(i)). Glass was used as a substrate to reduce the exposure of media to the PDMS, which is known for its ability to absorb small hydrophobic molecules [202], [203]. The air channel (Figure 3.1H (i)) is printed on the surface of a spin-coated PDMS membrane followed by integration with a porous membrane (Figure 3.1H (ii & iii)) (pore size 126.5 ± 27.3 μm) (Figure 3.1I), printed with PDMS ink. After fabricating all the layers of the device, lung cancer cells are printed in a grid formation at the center of the bottom layer, whereas the fibroblasts are printed around the epithelial cells (Figure 3.1J(ii)) to create a flow barrier from media reservoir (left) towards the media reservoir (right). Finally, all the layers are unified (Figure 3.1J (iv)), and media and airflow are introduced simultaneously using programmable syringe pumps. In our device, in order to support cell growth with the medium supply and nutrients, the cell-laden hydrogel was printed in the fluidic channel connected to the media reservoir enabling dynamic culture of the cells. Also, the air channel has been designed for gas exchanges to enable air-liquid interface for the lung epithelial cancer cells similar to in-vivo. Introduction of the porous layer with the optimized pore size of around 126.5 ± 27.3 μm, was not only applied to ensure that the cell-laden hydrogel (epithelial compartment) is directly exposed to the air and gases effectively, but also to avoid any leakage and disruption effect on the flow of the culture medium in the lower fluidic channel. The porous layer has been designed to provide enough interface between the hydrogel and air for gas exchange through the pores. we controlled the flow of air

similar to breathing rhythm in-vivo, by creating cyclic “inhalation” for 2.5 s, which results in 120 µl air intake according to area of our epithelial cancer layer and pore size distribution, followed by an “exhalation” phase of 2.5 s. Thus, the total time for a single breath is 5 s, which is approximating the physiologically relevant breathing conditions[155].

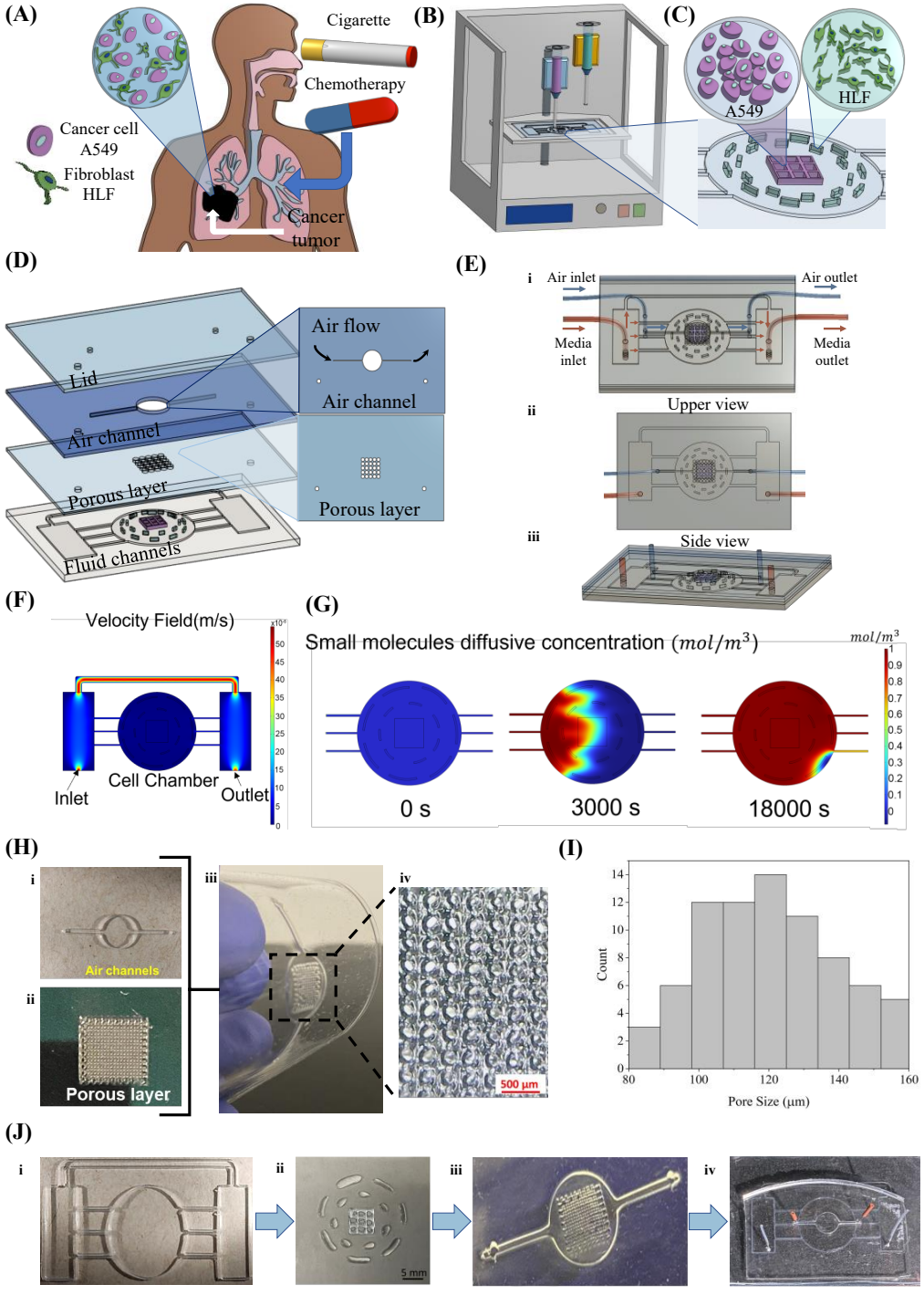

Figure 3.1 Graphical representation of the IVM3DLCOC model and its fabrication process. (A) Effect of CSE and chemotherapeutic drugs on the progress of lung cancer metastasis with A549, a human lung cancer cell line, and human lung fibroblasts (HLF), studied in the proposed IVM3DLCOC model. (B) Rapid prototyping via 3D bioprinting is used

to biofabricate the multilayer and multistage IVM3DLCOC model as an all-inclusive unit contacting cell constructs along with the lung's representative air and fluid compartments. Simultaneously, lung cells are bioprinted as a (C) cell-laden hydrogel to grid structure and lung fibroblasts are bioprinted as a flow barrier around the lung cancer cells. (D) The lung-like chip component of the model is composed of 3 different layers of media reservoir and cell chamber connected by microfluidic channels, a porous layer, and air channels. The model is designed with an air-liquid interface, exhalation/inhalation, and mechanically/biologically in vivo–mimicking 3D microenvironment for maintaining cell functions in-vitro. (E) (i) side view, (ii) upper view, and (iii) lateral view of the model are presented. (F) COMSOL simulation modeling is applied to envision the flow dynamics inside the fluid channels upon connecting with the pumps. (G) Diffusion control flow is validated to confirm the gradual diffusion of the media towards the cell chamber from the inlet media reservoir. (H) (i) Air channel is printed on the top of a spin-coated PDMS layer, and a 3D printed (ii) porous layer is (iii) implemented to provide an air-liquid interface on top of the lung epithelial cells. (iv) Microscopic images of the porous layer show an average pore size of 126.5 ± 27.3 μm quantified using ImageJ (n = 100). (J) (i) The media reservoir and cell chambers are printed on top of a substrate, followed by (ii) the bioprinting of lung cells in the desired patterns. (iii) The porous layer integrated with the air channel is then bonded to (iv) the media reservoir and cell chambers that contain the cells, followed by applying the flow of both liquid and air to the model.

3.2.2 Characterization of Cell-laden Hydrogels

Hydrogels are the most promising bioinks for 3D bioprinting, as they mimic features of ECMs, can be modified to achieve mechanics similar to those of soft tissues and can support cell adhesion and proliferation. Therefore, bioinks were characterized to fully confirm their capacity to successfully bioprint human lung cells to the desired structures. The printing fidelity of GelMA 10% + 0.2% LAP was inferior to CAD design (i.e. expected dimensions). Thus, the ink was supplemented with 5% Gelatine type A to improve rheological characteristics during printing. The mechanical and rheological behaviour of GelMA 10% LAP 0.2% and GelMA 10 + Gelatin 5% Lap 0.2% were investigated. The unconfined compression curves are shown in Figure 3.2A. The resulting compressive modulus were 5.2 ± 0.1 and 8.9 ± 0.4 kPA for GelMA 10% LAP 0.2% and GelMA 10 + Gelatin 5% Lap 0.2% respectively. The supplementation of GelMA 10% with Gelatin 5% results in an increase of compressive

modulus in comparison with pristine GelMA 10%. Both modulus are comparable with the modulus of native human lung tissue (~1.4 to 7.2 kPa)[204] but significantly less than the modulus of glass or plastic tissue culture plates, thus GelMA10% Gelatin 5% was the bioink finally selected for 3D bioprinting of A549 and HLFs [204]. Nonetheless, this ink shows viscoelastic shear-thinning properties at low temperatures, which is highly desirable for 3D printing applications (Figure 3.2B, C, D).

The optimized ink composition was mixed with the respective cells, i.e., A549 cells at a concentration of 3 x 106 cells/ml and HLFs at a concentration of 2 x 106 cells/ml, and then 3D bioprinted to the grid (centre) and circular (periphery) structures, respectively (Figure 3.1J (ii)). Both cell-containing bioinks are printed simultaneously using two different printheads (Figure 3.1B). After printing, the constructs are incubated overnight in the cell holding part of the IVM3DLCOC model to fully remove the melted sacrificial gelatine, and then bonded with the other layers (Figure 3.1J (iv)). The viability of the printed cell constructs is assured using a live-dead assay after overnight maintenance on the bottom fluidic layer (Figure 3.2E). Both A549 and HLF showed >80% cell viability on day 1 post printing, and >90% viability was recorded after 14 days of culture (Figure 3.2E), further validating the suitability of the optimized bioinks to offer superior maintenance of 3D printed viable human lung cells.

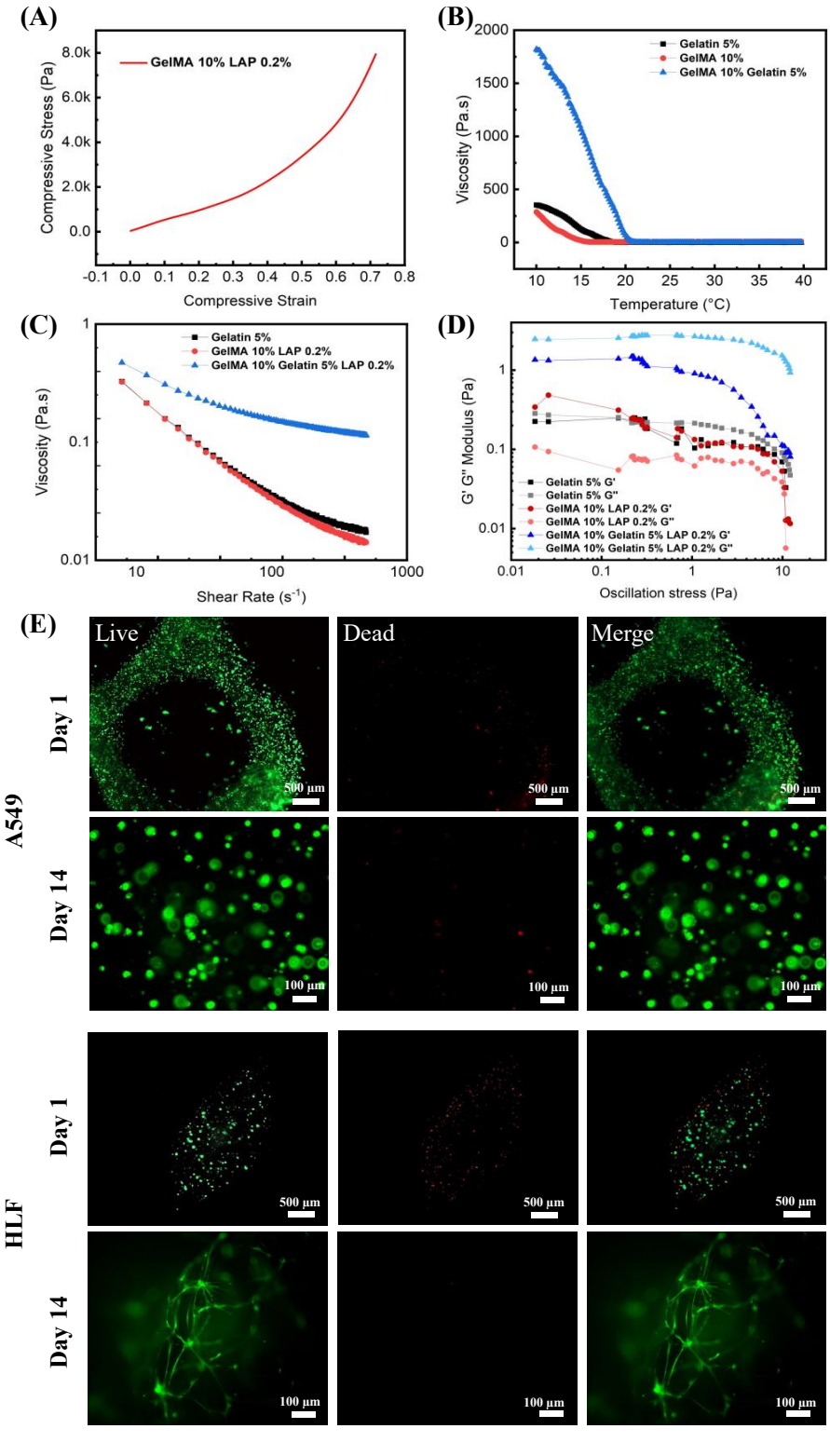
(A)
GelMA 10% LAP 0.2%
Compressive Stress (Pa)
Compressive Strain
(B)
Gelatin 5%
GelMA 10%
GelMA 10% Gelatin 5%
Viscosity (Pa.s)
Temperature (°C)
(C)
Gelatin 5%
GelMA 10% LAP 0.2%
GelMA 10% Gelatin 5% LAP 0.2%
Viscosity (Pa.s)
Shear Rate (s-1)
(D)
Gelatin 5% G'
Gelatin 5% G''
GelMA 10% LAP 0.2% G'
GelMA 10% LAP 0.2% G''
GelMA 10% Gelatin 5% LAP 0.2% G'
GelMA 10% Gelatin 5% LAP 0.2% G''
G' G'' Modulus (Pa)
Oscillation stress (Pa)
(E)
Live
Dead
Merge
A549
Day 1
Day 14
HLF
Day 1
Day 14
500 μm
100 μm

Figure 3.2 Characterization of bioinks for human lung cells. (A) Disks 7 mm in thickness and 15.6 mm in diameter are fabricated and used to measure compression modules of GelMA 10% LAP 0.2% and GelMA 10% Gelatin 5% LAP 0.2%. (B), (C), (D) Rheology characterization of the bioink with and without 5% gelatin. Rheological properties of pure 5% gelatin, GelMA 10% LAP 0.2%, and GelMA 10% Gelatin 5% LAP 0.2% are evaluated to assure extrusion printability. (E) Cell viability of both A549 and HLF cells is validated on day 1, after printing and culturing the cells in GelMA 10% LAP 0.2% 5% Gelatin for 14 days. The live-dead assay is conducted using calcein-AM (Live: Green) and ethidium homodimer-1 (Dead: Red). >80% cell viability is found for both cell types on day 1 post-printing and a >90% after 14 days of maintenance of both the lung cells within the optimized bioink formulation.

3.2.3 Biological Characterization of IVM3DLCOC

Media flow of 80 µl/hr and airflow of 120 µl/2.5 s of inhalation and 2.5 s of exhalation was applied to the fluidic system of IVM3DLCOC model to obtain delivery of the media flow as optimized by COMSOL simulation along with providing an in-vivo mimicking air-liquid interface presented only to the lung epithelial cells. The model was maintained for 14 days and evaluated for cell growth by visualizing cell cytoskeletons through staining with F-Actin and EMT transition markers, i.e., E-Cad and N-Cad, on days 3, 7, and 14 (Figure 3.3A, C, E). A significant increase in F-actin expression, which indicates a gradual increase in the size of A549 spheroids, was observed (figure 3.3A, 3.3B). This results in inhibition of nutrients and oxygen to the spheroid core, thus mimicking the realistic hypoxic and necrotic situation of in-vivo tumors [205]. Interestingly, E-Cad expression (Figure 3.3C, 3.3D) remained unchanged from day 3 to 7 and decreased after day 14, whereas N-Cad (Figure 3.3E, 3.3F) constantly increased from day 3 to day 14, indicating gradual upregulation of mesenchymal transition marker along with downregulation of the epithelial markers in A549 cells in a 3D dynamic culture. These observations indicate that A549 cells increase in invasiveness over long-term maintenance in dynamic 3D culture. As with

A549 cells, an increase in activation marker, i.e., alpha-smooth muscle actin (α-SMA) was also observed from day 3 to day 14 in HLF co-cultured with A549 cells (Figure 3.3G, 3.3H), thus indicating a transition from normal fibroblasts towards cancer-associated fibroblasts (CAF) in co-culture with lung cancer cells in-vitro. In 2019 Tièche et al. reported on the morphological behaviour of A549 cells, which showed invasiveness, migration capability, and resistance to anti-cancer drugs in 2D in-vitro cultures [206]. It was also documented that both 2D and 3D culture conditions could influence the spatial organization of A549 cells, which shifted from a flat morphology in 2D models (i.e., on a glass substrate) towards a spherical shape in 3D models (i.e., in Matrigel) [207]. Another group, Prina-Mello et al., reported that A549 acquires a mesenchymal phenotype in 3D culture inside soft hydrogels like Matrigel™ and PuraMatrix™ and demonstrated a PI3K/Akt signalling cascade–associated higher secretion of IL-8 that could induce an increase in the invasiveness of A549 cells independent of EMT [207]. It was also previously reported that co-culture of A549 cells with normal lung fibroblasts can induce the transformation of those fibroblasts towards cancer-associated fibroblasts 7, which is consistent with our observation of an increase in α-SMA expression from day 3 to day 14 (Figure 3.3H). Thus, the present IVM3DLCOC model is able to preserve the characteristics of the bioprinted cells over the culture period, demonstrating that it is an effective model for tissue engineering with functional human lung cells in-vitro.

Nicotine and cigarette smoke overall can create a variety of lung diseases including both small-cell lung cancer (SCLC) and non-small cell lung cancer (NSCLC) not only to the smoker but also to the people surrounding them, who effectively

become passive smokers [208]. As the first model of study, our IVM3DLCOC model was implemented to study the effect of CSE extract by considering heavy (20 cigarettes/day) and light smoking (10 cigarettes/day) situations. The appropriate CSE concentrations were determined by quantifying their nicotine content to create heavy and light smoking scenarios. The EMT of A549 cells under nicotine treatment was studied by immunostaining the EMT transition markers. The effect of CSE on the IVM3DLCOC model was studied by treating the dynamic culture after 5 days of maintenance in healthy conditions with two different concentrations of CSE. The two concentrations of CSE were achieved by diluting the stock CSE solution, which had a concentration of 66.88 μM, quantified from the standard equation (Figure 3.5) obtained by GC-MS of the nicotine solutions of known concentrations. To model the CSE effect for heavy smokers (20 cigarettes/day) and light smokers (10 cigarettes/day), 3.09 μg/day and 1.54 μg/day respectively, nicotine was allowed to circulate in the IVM3DLCOC model for 30 days, which within 24 hrs stimulated the advancement of lung cancer metastasis. Metastasis markers (Figure 3.3I, 3.3J) for both lung cancer cells (N-Cad) and stromal cells (α-SMA for HLF) were evaluated after treatment with a defined concentration of cigarette smoke extract for 24, 48, and 72 hrs. CSE treatment produced a ~3-fold increase in N-Cad expression in A549 cells (Figure 3.3K) and ~2.5-fold increase in α-SMA expression in lung fibroblasts (Figure 3.3L) as treatment time increased from 24 to 72 hrs. Again, an increasing trend in N-Cad expression for A549 cells and α-SMA expression for HLFs was seen with increasing nicotine concentration at all time points (Figure 3.3K, 3.3L). These observations indicate the enhancement of metastatic markers upon treatment with

CSE over time. Also, the differences in heavy and light smoking situations are significantly visible and differentiable in EMT markers expressions, and IL6 secretion in the IVM3DLCOC models. As expected, with increasing concentrations of CSE, the induction of EMT in A549 cells is highly evident from the significant upregulation of N-cad expression in A549 cells and a gradual increase in α-SMA expression in HLFs (Figure 3.3I, 3.3J)[209], [210], [211]. A time-dependent and persistent increase in N-Cad and α-SMA expression was also notable as treatment continued through 72 hrs. Our observations are consistent with previous studies of the effects of nicotine treatment on A549 cells, which reported that raising the nicotine concentration increased the invasiveness and migration of A549 cells, and a maximum effect was observed for a nicotine concentration of 1μM as reported by Dasgupta et al. [210]. Sun et al. reported that nicotine-induced migration and proliferation of A549 cells by binding to nicotinic acetylcholine receptors (nAChRs) [212]. Thus, our observations indicate significant increases in metastatic possibility, which are higher for heavy smokers and lower for light smokers.

Interleukin-6 (IL-6) is a well-established marker of lung fibrosis, with significant increases associated with the likelihood of metastasis in lung cancer cells as a result of EMT promotion[213], [214]. In the present study, the role of IL-6 in lung cancer metastasis was also validated by measuring it in both heavy and light smoking situations after 24, 48, and 72 hrs. of treatment with defined CSE concentrations (Figure 3.3M). A ~ 3-fold ($p = 0.0218$) and ~ 4-fold ($p = 0.0012$) increase in IL-6 secretion compared to the control was observed for light and heavy smoking conditions, respectively, after only 24 hrs of treatment. After 48 hrs, ~ 3.3-fold (p =

0.0029) and ~ 6-fold (p = 0.0010) increases in IL-6 secretion compared to control group were seen for light and heavy smoking conditions, respectively. In the case of 72 hrs. of CSE treatment, for light smoking, a ~ 5.6- fold increase in IL-6 secretion was observed, whereas only a ~ 2.2-fold increase in IL-6 secretion (considerably lower than after either 24 or 48 hrs treatment) was observed for the heavy smoking situation. This phenomenon might be attributed to the increase in cytotoxicity at higher concentrations of CSE after 72 hrs, which may reduce cell functional activity and then decrease IL-6 secretion [215], [216]. Thus, compared with the control, the IVM3DLCOC model showed a significant increase in IL-6 secretion upon treatment with CSE for both heavy and light smoking conditions. Again, it was previously reported that cancer-associated fibroblasts (CAFs) can secrete IL-6, enhancing the metastatic potential associated with the activation of the IL-6/STAT3 signalling pathway in lung cancer cells [192]. Thus, co-culture of A549 cells with HLFs and the gradual activation of HLFs in the dynamic co-culture may further influence the EMT and metastatic probability in A549 cells.

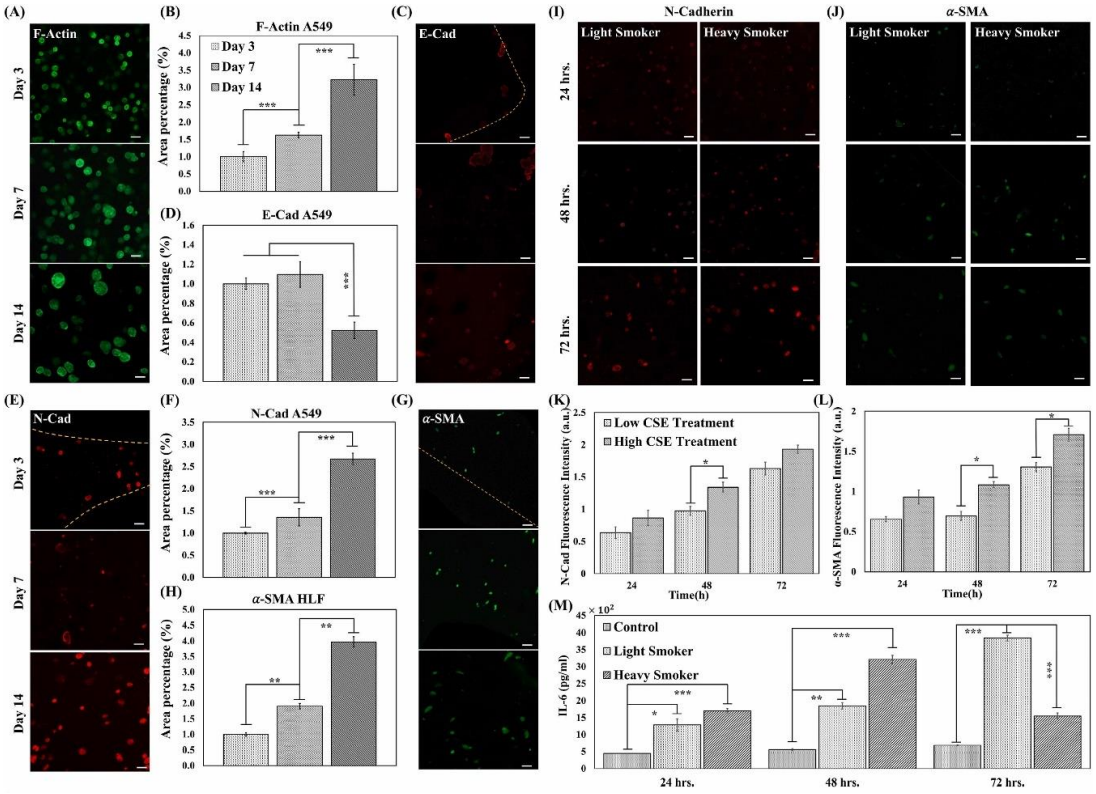

Figure 3.3 The IVM3DLCOC model's bioprinted A549 and HLF cells are maintained in dynamic culture for 14 days. Immunostaining is applied to visualize the metastatic markers of A549 (E-Cad, N-Cad), morphology of A549 (F-actin) spheroids, and activation marker of HLFs (α-SMA) in the cell-laden hydrogel on days 3, 7, and 14. As expected, over time, (A) F-actin expression increased from (B) day 3 to day 14 with increasing spheroid size; (C) E-Cad expression remained statistically consistent from (D) day 3 to day 7, but decreased significantly from day 7 to day 14. (E) A constant and significant increase in N-Cad expression is observed from (F) day 3 to day 14 as noted from immunostaining at different time points. In the case of HLFs (G) a gradual increase in α-SMA expression is observed in HLFs from (H) day 3 to day 14. n = 3; *p<0.05, **p<0.01, ***p<0.001. Scale Bar = 50 μm; Two different concentrations of CSE, to simulate 1-month exposure of nicotine within a 24-hr time frame for heavy and light smoking situations, are used to elicit the expression of N-Cad for A549 cells and α-SMA for HLFs. Immunostaining images of (I) N-Cad and (J) α-SMA indicate that increases in concentration and time of exposure of CSE resulted in upregulation of both (K) N-Cad, and (L) α-SMA. Scale bar: 50 μm. n = 3; *p<0.05; (M) IL-6 is quantified for different CSE concentrations after 24, 48 and 72 hrs. of exposure. *p<0.05; **p<0.01; ***p<0.001.

3.2.4 Drug Efficacy Study

The IVM3DLCOC model was further studied to assess the effect of

chemotherapeutic drugs and its effect on lung cancer cells (Figure 3.4). As a second model, 5,10, and 20 μM paclitaxel were applied to the culture media and circulated in the model for 48 hrs. As expected, there was a gradual decrease in cell viability with increasing concentrations of paclitaxel (Figure 3.4B). Thus, the proposed IVM3DLCOC model has proven efficient in reflecting variation in cell viability associated with changes in drug concentration, which is necessary to quantify the dose-dependent efficiency of chemotherapeutic drugs. Our observations complement previous reports that paclitaxel induces apoptosis and inhibits proliferation of A549 cells cultured in vitro 68. The reported IC50, i.e., the concentration of paclitaxel necessary to create cytotoxicity in 50% of a defined population of A549 cells, is 808.7 ng/mL [217]. Thus, in the present study, the applied drug concentration is higher than the IC50 value. Zheng et al. also reported that a significant decrease in viability of A549 cells was only evident for a paclitaxel concentration of 10 μg/mL and above for ~ 104 cells/well seeded in 96 well plates [218]. In our study a gradual decrease in cell viability was observed as the paclitaxel concentration increased from 0 (76.4 %) to 5 (59.6 %), 10 (48.7 %), and 20 μM (28.6 %).

The utility of the proposed IVM3DLCOC model for CSE-induced toxicity studies was demonstrated by investigating the effect of nicotine concentration on metastatic characteristics of human lung cells. In addition, the model is suitable for drug efficacy studies. Our model can be further modified by adapting one or more secondary organs, e.g., liver or bone, which are possible sites of lung cancer metastasis, to study extravasation and the formation of secondary tumors at distant organs. Furthermore, the inflammatory immune cells play an essential role in cancer-related inflammation

[219]. During cancer progression, every biological event cascade gets subjected to the immune response due to the presence of the mutated immunogenic cancer cells, e.g., CD8+ T cells and natural killer (NK) cells can potentially restrict the metastatic outgrowth of cancer cells[164]. In addition, myeloid cells e.g., macrophages participate actively in the cancer metastasis process. The macrophage activity can be manipulated by using different cytokine types, e.g., Toll-like receptor (TLR) and interferon-γ (IFNγ) activated macrophages can result in the elimination of pathogens and tumor cells to some extent, whereas, IL-13 and IL-4 activated macrophages can stimulate the tumor progression by participating in tissue remodeling [220]. Both in vivo and in vitro study suggests that the tumor microenvironment can modulate the immune cell response and results in a dynamic intra and intercellular cross-talk which may favor tumor cell invasion, survival during circulation, extravasation, and subsequent growth in the distant organ. In conclusion, the tumor microenvironment gives rise to the secretion of inflammatory cytokines by the immune cells, and the cytokine cocktail can further influence the inhibition and progression of metastatic lung cancer. Thus, to fabricate a more in-vivo mimicking cancer microenvironment, future work will be based on the inclusion of the immune cell response by co-printing macrophages which is a major cell type present as a stromal cell, along with the human lung fibroblasts. The proinflammatory markers (TNF-α, IL-12, IFN-γ) secreted by cancer-associated macrophages will be studied upon treatment with different external stimulus.

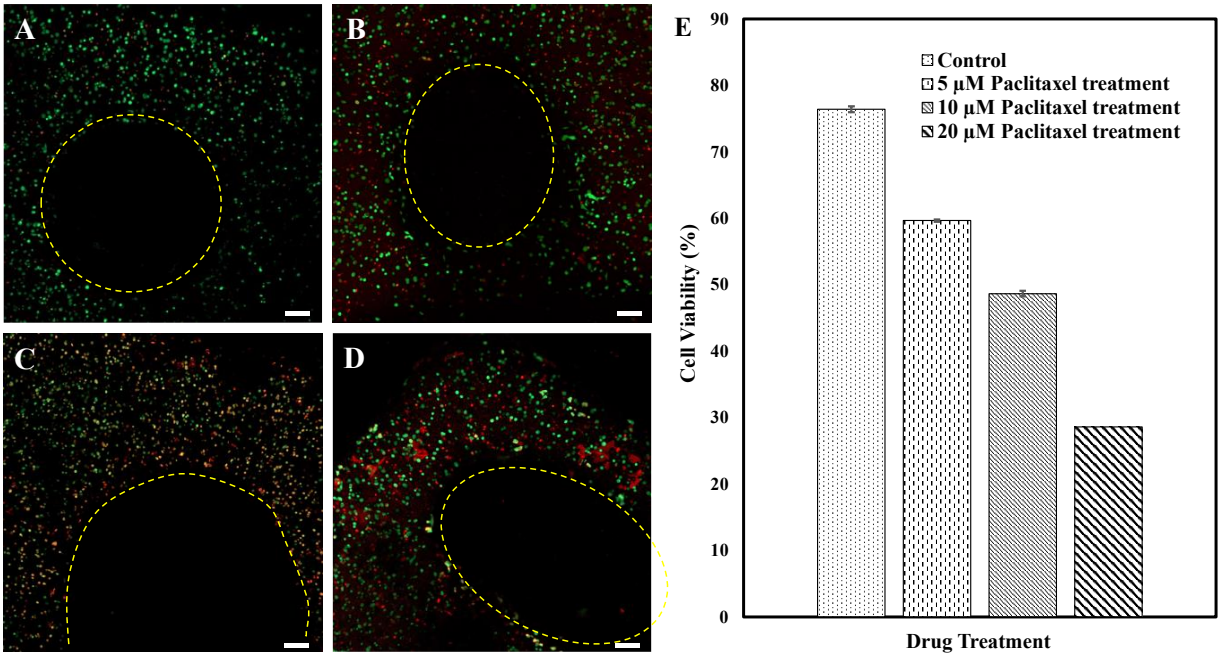

Figure 3.4 The IVM3DLCOC model was treated with (A) 0, (B) 5, (C) 10, and (D) 20 µM paclitaxel to visualize dose-dependent anti-cancer drug efficacy. The yellow dotted lines define the structure of bioprinted A549 cells. (E) A gradual drop in cell viability was observed with increasing concentrations as quantified using ImageJ software. Mag: 5x; Scale bar: 200 µm n=3.

3.3 Conclusion and Future directions

The development of the in-vivo mimicking 3D-lung-cancer-on-a-chip (IVM3DLCOC) model represents a significant advancement in lung cancer research, yet there are several potential avenues to further enhance its accuracy, relevance, and applicability. One of the key advancements for enhancing the physiological relevance of the IVM3DLCOC model is the incorporation of patient-derived cells. Utilizing primary cells obtained directly from lung cancer patients can provide a more accurate

representation of the tumor microenvironment[221]. This approach would enable the model to better mimic the genetic and phenotypic diversity observed in human cancers, thereby improving the predictive accuracy for clinical outcomes and personalized medicine applications.

To increase the physiological relevance of the model, future iterations should aim to more closely replicate the complex geometry of the human lung. This involves not only the accurate recreation of alveolar structures but also the integration of branching airway patterns. Advanced bioprinting techniques and computational modeling could be employed to achieve these intricate structures, thereby providing a more realistic environment for studying lung cancer progression and treatment.

The current model successfully mimics several aspects of the lung microenvironment, including the air-liquid interface and fluid flow. However, incorporating the dynamic mechanical forces associated with respiration would further enhance the model's relevance. Future developments should aim to replicate the expansion and contraction of the lung epithelium in response to inhalation and exhalation. This can be achieved through the integration of mechanical actuators or flexible materials that simulate the natural breathing cycle, providing critical insights into how mechanical forces influence cancer cell behavior and treatment responses.

While the current model includes lung cancer cells and fibroblasts, expanding the co-culture systems to incorporate other cell types found in the lung microenvironment, such as immune cells, endothelial cells, and additional stromal components, would provide a more comprehensive understanding of tumor-immune interactions and the role of the microenvironment in cancer progression[222]. This

approach can uncover new therapeutic targets and strategies for immunotherapy.

Enhancing the model's capacity for high-throughput screening of potential therapeutic agents and toxins would significantly benefit preclinical drug development. Integrating microfluidic systems and real-time monitoring technologies, such as live-cell imaging and biosensors, would allow for continuous observation of cellular responses to treatments, providing valuable data on drug efficacy and toxicity in a time-efficient manner[223], [224], [225].

Ultimately, the goal is to utilize the IVM3DLCOC model as a personalized medicine tool. By integrating patient-specific genetic information and clinical data, the model can be tailored to predict individual responses to therapies, enabling the development of customized treatment plans. Collaborations with clinical researchers and the incorporation of advanced genomic and proteomic analysis techniques will be crucial in achieving this objective.

By pursuing these future directions, the IVM3DLCOC model can evolve into an even more powerful and versatile platform for lung cancer research, offering new insights into disease mechanisms and facilitating the development of more effective and personalized therapeutic interventions.

3.4 Materials and Methods

Design of the lung-like-chip component of the IVM3DLCOC model

The microfluidic lung-like chip is designed to mimic physiologically relevant structural cues (Figure 3.1). The chip is composed of 3 layers: (i) media reservoir and cell chamber connected by microfluidic channels; (ii) porous layer; (iii) and an air channel, printed on a spin-coated PDMS top layer. Briefly, two rectangular media reservoirs of 300 μm in height, 10 mm in width, and 20 mm in length are fabricated in which the medium circulates through a connecting 3D printed channel of 300 μm in height and 1 mm in width. To create diffusion-controlled flow in the cell chamber, the medium is circulated between two reservoirs using programmable syringe pumps.

Fabrication of the lung-like-chip component of the IVM3DLCOC model

PDMS is used to print different layers of the lung-like-chip. Our lab has already optimized the protocol to 3D print PDMS ink [226]. Briefly, the ink is prepared by mixing SE 1700 (Dow Corning, MI) and Sylgard 184 base materials with their curing agents at a 10:1 ratio for 10 min followed by degassing in a vacuum for 20 minutes. The degassed SE1700 and Sylgard 184 are mixed at a ratio of 7:3 to achieve the final ink composition. The bottom layer, containing microchannels for fluid, media chamber, and cell chamber, are printed by applying extrusion printing. The porous layer between the air channel and the fluid channel is printed with the same PDMS ink. The pores are roughly 126.5 ± 27.3 μm in size, as shown in figure 3.1I. Finally, the sealed air channel assembled with a porous layer containing all the openings for the fluid and air inlets and outlets is sealed to the bottom fluid channel.

Synthesis of GelMA

Gelatin methacryloyl (GelMA) is synthesized by dissolving type A gelatin from porcine skin at 10% (w/v) in Dulbecco's phosphate buffered saline (DPBS) and stirring at 50°C and 300 rpm for 1 hour. Methacrylic acid is added dropwise with a syringe pump (0.5 mL/min) to the solution at 10% (v/v) and allowed to react for 1 h. The reaction is finished by adding 5x volumes of DPBS. The resulting solution is dialyzed for 7 days with distilled water at 37°C to remove unreacted methacrylic anhydride using dialysis membranes with 12-14 kDa cut off and changing the water twice per day. The resulting solution is frozen and lyophilized for five days and stored at -80°C for future use. Lyophilized GelMA is dissolved at 5% (w/v) in DPBS at 70°C in a water bath containing 0.1% (w/v) of lithium phenyl-2, 4, 6-trimethylbenzoylphosphinate (LAP) (ALEVY) as the photoinitiator. GelMA solutions are sterilized using 0.22 μm polyether sulfone (PES) filters before being applied for 3D bioprinting of the cell layers.

Bioprinting of lung cells

Bioink formulations are optimized to mimic the mechanical properties and long-term viability of human lung cells under 3D culture conditions. A549 cells, a human lung cancer line, is mixed with 10% GelMA Low and 0.2% Lithium phenyl-2,4,6-trimethylbenzoylphosphinate (LAP) at a concentration of 2x106 cells/ml to print grid structures at the centre of the organ chamber, whereas 10% GelMA High, 0.2% LAP is used to print human lung fibroblasts (HLFs) at a concentration of 0.5x106 cells/ml as a barrier to media movement to create diffusion control flow towards the printed epithelial cells.

Computational modeling

Laminar fluid flow and dilute species transport are simulated using COMSOL Multiphysics® 6 (COMSOL AB). To compute the velocity from convection, the incompressible Navier–Stokes model for Newtonian flow with the viscosity of 0.78 mPa·s and density of 1,000 kg/m^3 for the culture medium at 37°C [227]43 and boundary condition of no-slip on all media channel walls and membrane surfaces are employed. Diluted species (i.e., drug molecules) transport is simulated by the advection-diffusion equation, adjusting the laminar inflow rate specified at the media channel inlet; laminar outflow conditions at the outlet; and dilute species concentration specified at the inlet at a concentration of 1mol/m^3. A zero initial concentration in the device, a diffusion coefficient of 1.0 ×10^(-9) m^2/s in culture media, and no cell uptake and no flux through walls are applied.

Hydrogel mechanical property assessments

Compression testing

The GelMA hydrogel samples are prepared for compression testing, which is performed using an Instron 3365 UTS universal testing machine (Norwood, Massachusetts, United States) at room temperature under a compression rate of 200 μm/min. Compression samples are prepared and molded with a diameter of 15.6 mm and a height of 7 mm. Compression testing of GelMA samples is carried out at least 3 times, and the mechanical properties of compression are obtained from the averaged compression stress-strain curve. The compression modulus was calculated as the

slope of the linear region in the 0.1-0.15 strain range of the stress-strain curves.

Rheological properties

The rheology profile of GelMA inks was obtained using a TA DHR-2 Discovery series (TA instruments, United Kingdom) equipped with a Peltier for temperature control. Parallel plate geometry (25 mm) was used with a gap of 0.2 mm. GelMA ink was previously tempered at 37°C before each testing. The viscosity of GelMA was measured with a temperature ramping from 40-10 °C with a cooling rate of 1°C/min and a constant shear rate of 1/s. Dynamic modulus (Storage G' and Loss G``) were measured using an angular frequency of 10 rad/s and a shear rate between 0.01 and 10 Pa. Shear stress response was evaluated by varying shear rate between 0.01-1000 1/s in a rotational test.

Integration and assembly

After printing the cells on the pre-printed fluidic bottom layer, other layers are bound in a non-reversible manner by localized plasma treatment which is a simple, fast and cheap method, needs no special environment [228]44, performed at atmospheric pressure and temperature by using a corona discharge machine (BD-20AC LABORATORY CORONA TREATER- Electro-Technic Products). This proceduce gives a leakage-free device with localized bonding capabilities as tested for a time period of 14 days with circulating media by using a syringe pump. COMSOL simulation is used to optimize the media flow dynamics to achieve physiologically relevant fluid flow. An air flow rate of 120 µl 2.5 s inhalation, 2.5 s exhalation, and fluid flow rate of

80 µl/hr are applied to maintain the constructs in the fabricated perfusion culture model. After integrating the unit, it is maintained in a cell incubator at 37 °C in the presence of 5% carbon dioxide (CO2) under humidified conditions.

CSE-induced toxicity studies

The methods used to develop CSE are reported elsewhere [229]45 and adopted in the present work for preparing the stock solution. Briefly, the aqueous constituent of CSE was prepared by designing a home-made device to bubble the smoke of 8 commercially available cigarettes (Nicotine content = 10.2 mg/ cigarette) until only the butt remained (23 mm) in 1x PBS by imposing 2 seconds of puff time followed by 30 seconds of interval in series. This process produces the CSE stock solution, which is further diluted to achieve two different concentrations, i.e., 13 µl/ml and 6.7 µl/ml in the media stream to create physiologically relevant nicotine exposure per unit area of the printed lung model (50.4 mm2) for 30 days within 24 hrs. time for both a heavy smoker (based on 20 cigarettes/day) and a light smoker (based on 10 cigarettes/day) [230]46. The CSE exposure in both heavy and light smoking situations are maintained for 24, 48, and 72 hrs on the IVM3DLCOC model to study the exposure effect for 90 days. The CSE extract was prepared by using the current protocol is reported to remain stable till 24 hrs. Thus, the CSE extract was made everyday during the study to mix with freshly prepared culture media to the desired concentration to avoid concentration variation or additional toxicity which may arise from the CSE degradation product.

Gas Chromatography-Mass Spectroscopy (GC-MS)

GC-MS was performed to quantify the nicotine absorbed in the CSE extract. A nicotine standard is prepared by diluting nicotine (MilliporeSigma, Carlsbad, CA, USA) in GC grade Dichloromethane (DCM, MilliporeSigma) to the concentrations of 300 μM, 150 μM, 75 μM, 37.5 μM, and 18.8 μM to prepare the standard plot (Figure 3.5). The nicotine content in the stock CSE solution is evaluated from the standard concentration curve, followed by extraction from the aqueous solution. Briefly, 3 ml of CSE is mixed with 6 ml of DCM and 1.5 ml of 2 M sodium hydroxide (NaOH) solution for 1 minute by a vortex. The bottom organic layer is collected and mixed with 1.5 ml of 1 M hydrochloric acid (HCL), followed by further mixing of the aqueous layer with DCM and 2 (M) NaOH to finally separate the organic layer and quantify the nicotine content by GC-MS.

Drug efficacy studies

Paclitaxel is applied as an anti-cancer drug at 5, 10, and 20 μM concentrations to evaluate its effect on lung cancer cells in the IVM3DLCOC model. The bioprinted cells are maintained in culture for 5 days before being treated with a defined drug concentration for 48 hrs.

Live-dead assay

A live-dead viability assay is performed to visualize the cell viability of the printed constructs during culture and after treatment with 5, 10, and 20 μM paclitaxel over 48 hrs. Calcein-AM and ethidium homodimer (EthD-1) (Life Technologies, California, United States) are used to stain live (Green) and dead cells (Red),

respectively. Briefly, cells are incubated with 2 μM live and 4 μM dead reagent for 30 min followed by washing with 1x phosphate buffer saline (PBS) 3 times. After washing, the cell constructs are imaged by using a Confocal Microscope (ZEISS LSM 900, Jena, Germany).

Immunostaining

Immunostaining is performed before and after treatment with CSE extract to visualize the effect of CSE-induced toxicity on epithelial-to-mesenchymal transition markers. Briefly, at defined time points cells of the IVM3DLCOC model are fixed with 4% Paraformaldehyde (PFA) (Fisher Scientific, Waltham, Massachusetts, United States) for 10 mins, followed by washing with 1x PBS. Then the cells are permeabilized with 0.1% Triton-X-100 (Fisher Scientific, Waltham, Massachusetts, United States) solution in 1xPBS for 5 mins. After washing, the constructs are treated with 3% BSA (Fisher Scientific, Waltham, Massachusetts, United States) in PBS to prevent non-specific binding, followed by overnight incubation with primary antibodies for E-Cad (E-cadherin Mouse anti-Human, Clone: DH01 (DCS-266), Invitrogen™), N-Cad (N-cadherin Rabbit anti-Human, Invitrogen™), α- SMA (anti-alpha-Smooth Muscle Actin, Alexa Fluor 488, Clone: 1A4, R&D Systems™), and F-actin (Alexa FluorTM 488 Phalloidin, Thermo Fisher Scientific). After completing treatment with primary antibodies, the samples are further treated with species-specific secondary antibodies (IgG (H+L), Goat anti-Rabbit, Alexa Fluor™ 555, Superclonal™) and incubated for 2 hrs. All samples are washed thoroughly with PBS (3 times for 5 minutes each), and images are captured by using ZEISS LSM 900 confocal microscopy.

Statistical analysis

The two studies are compared using two-tail student's t-tests. For each treatment group, the standard deviation is calculated as mean ± SD. $p < 0.05$, $p < 0.01$ and $p < 0.001$ is used to determine the level of significance.

3.5 Supporting Information

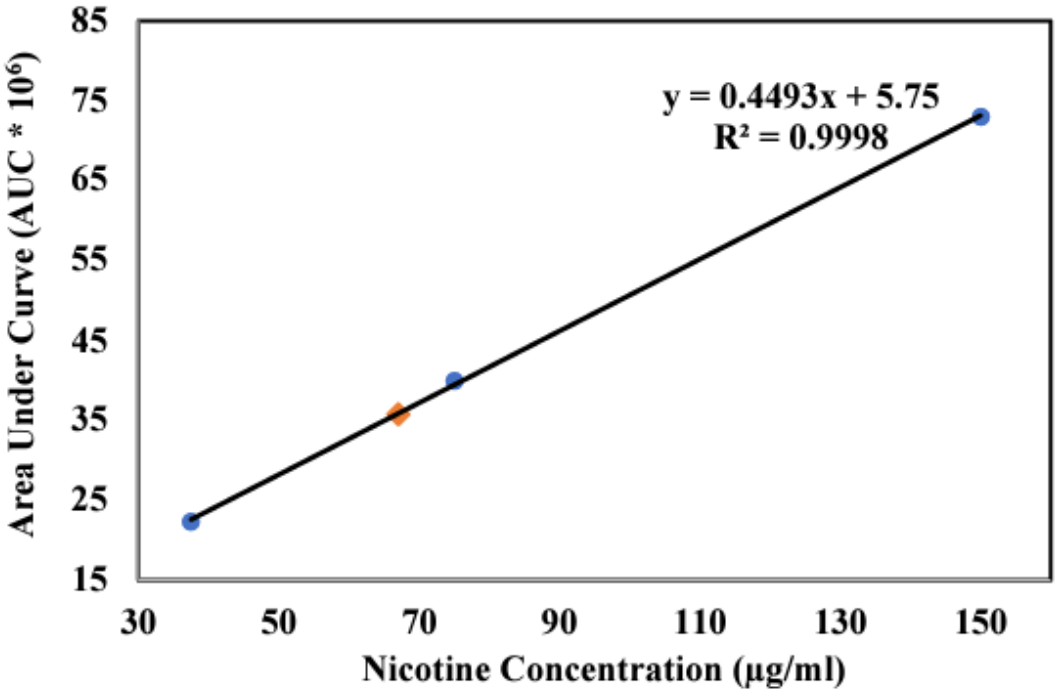

Figure 3.5 Standard curve obtain from GS-MS for known Nicotine concentrations in DCM.

Chapter 4

4.1 Conclusion

In vitro models have emerged as cornerstone innovations in medical research, offering profound insights into disease mechanisms and therapeutic efficacy. These models replicate human physiological conditions more accurately than traditional cell culture methods, providing a dynamic platform for disease study and drug testing. The relevance of such models is particularly pronounced in the study of complex diseases affecting organs like the colon and lungs, where the interplay of various cell types and the microenvironment plays a critical role in disease progression and response to treatment. The development of accurate in vitro models for the colon and lung is vital due to the high incidence of diseases affecting these organs, including colorectal and lung cancers. These conditions are among the leading causes of cancer-related mortality worldwide, necessitating innovative models that enable a deeper understanding of disease mechanisms and the development of effective treatments.

The advent of sophisticated 3D-bioprinted models has revolutionized our approach to studying complex diseases such as colorectal cancer, a leading cause of cancer-related mortality. Chapter 2 of this dissertation heralds a significant advancement with the introduction of a novel 3D-bioprinted colon model that not only replicates the intricate tissue architecture of the human colon but also its dynamic microenvironment. This model leverages the cutting-edge FRESH (Freeform Reversible Embedding of Suspended Hydrogels) 3D bioprinting technique to overcome previous biofabrication challenges, enabling the precise emulation of the colon's epithelial lining, stromal cells, and the three-dimensional luminal curvature

structures. Such fidelity in mimicking native tissue architecture is crucial for a granular exploration of disease mechanisms and the nuanced assessment of drug responses. Our model's design intricately simulates the luminal curvature and the layered complexity of the colon, enhancing cell viability, differentiation, and mechanical integrity beyond what conventional models have achieved. This leap in biofabrication not only sets a new benchmark in the creation of biomimetic structures but also amplifies the model's response to chemotherapeutic agents like 5-fluorouracil. The observed dose-dependent decrease in tumor cell metabolic activity within our model, resulting in an IC50 markedly higher than those seen in simpler 2D and 3D constructs, highlights the pivotal role of the microenvironment in influencing drug resistance. This discovery sheds light on the limitations of traditional drug screening methods and underscores the transformative potential of our 3D bioprinted colon model in advancing colorectal cancer research and therapeutic development by providing a more physiologically accurate representation of colorectal cancer treatment responses. These insights not only deepen our understanding of the complexities inherent in cancer progression but also pave the way for more effective and targeted treatment strategies, marking a new era in the fields of drug development and cancer research.

The second model of study in this dissertation is lung cancer on a chip. In the quest to combat lung cancer, which remains a leading cause of cancer-related fatalities globally, Chapter 3 introduces a lung cancer-on-a-chip model. This model stands as a pivotal advancement, meticulously crafted to simulate the lung's microenvironment, thereby offering a sophisticated platform for the study of cancer progression,

metastasis, and the evaluation of therapeutic interventions. By ingeniously incorporating both lung cancer cells and fibroblasts within a three-dimensional hydrogel matrix, this in vivo-mimicking construct not only facilitates an in-depth investigation of tumor dynamics but also provides a biologically relevant setting for assessing drug responses.

The model's sophistication lies in its co-culture system and the creation of an air-liquid interface, mimicking physiological inhalation-exhalation cycles and enabling studies on the effects of external stimuli like cigarette smoke extract on cancer progression. Demonstrating dose-dependent responses to chemotherapeutic agents, this lung cancer-on-a-chip model stands out for its potential in refining preclinical drug evaluations, offering a more accurate method for testing lung cancer therapies. By leveraging advanced 3D bioprinting techniques, this model not only enhances our understanding of lung cancer mechanisms but also sets a new benchmark for the development of targeted treatments, embodying a leap forward in lung cancer research.

The development and validation of the colon and lung in vitro models represent significant advancements in the field of biomedical engineering and disease modeling. These models not only enhance our understanding of disease pathophysiology but also offer a robust platform for drug discovery and development. Looking forward, the integration of these models with emerging technologies such as machine learning and artificial intelligence could further revolutionize the drug development process, enabling personalized medicine and reducing the reliance on animal testing.

In conclusion, this thesis contributes to the evolving landscape of in vitro disease modeling, offering novel insights and methodologies that promise to accelerate the pace of medical research and therapeutic innovation.

References

[1] J. Vanderburgh, J. A. Sterling, and S. A. Guelcher, "3D Printing of Tissue Engineered Constructs for In Vitro Modeling of Disease Progression and Drug Screening," *Ann Biomed Eng*, vol. 45, no. 1, pp. 164–179, Jan. 2017, doi: 10.1007/s10439-016-1640-4.

[2] A. Fatehullah, S. H. Tan, and N. Barker, "Organoids as an in vitro model of human development and disease," *Nature Cell Biology 2016 18:3*, vol. 18, no. 3, pp. 246–254, Feb. 2016, doi: 10.1038/ncb3312.

[3] J. Veldhuizen, R. Q. Migrino, and M. Nikkhah, "Three-dimensional microengineered models of human cardiac diseases," *J Biol Eng*, vol. 13, no. 1, pp. 1–12, Apr. 2019, doi: 10.1186/S13036-019-0155-6/FIGURES/3.

[4] J. Chen *et al.*, "Recent Progress in in vitro Models for Atherosclerosis Studies," *Front Cardiovasc Med*, vol. 8, p. 790529, Jan. 2021, doi: 10.3389/FCVM.2021.790529/BIBTEX.

[5] M. J. Waring *et al.*, "An analysis of the attrition of drug candidates from four major pharmaceutical companies," *Nature Reviews Drug Discovery 2015 14:7*, vol. 14, no. 7, pp. 475–486, Jun. 2015, doi: 10.1038/nrd4609.

[6] F. S. Collins, "Reengineering Translational Science: The Time Is Right," *Sci Transl Med*, vol. 3, no. 90, Jul. 2011, doi: 10.1126/SCITRANSLMED.3002747.

[7] D. Dunlap, E. F. McDonough, R. Mudambi, and T. Swift, "Making Up Is Hard to Do: Knowledge Acquisition Strategies and the Nature of New Product Innovation," *Journal of Product Innovation Management*, vol. 33, no. 4, pp. 472–491, Jul. 2016, doi: 10.1111/JPIM.12298.

[8] F. Peter Guengerich, "Mechanisms of Drug Toxicity and Relevance to Pharmaceutical Development," *Drug Metab Pharmacokinet*, vol. 26, no. 1, p. 3, 2011, doi: 10.2133/DMPK.DMPK-10-RV-062.

[9] D. Sun, W. Gao, H. Hu, and S. Zhou, "Why 90% of clinical drug development fails and how to improve it?," *Acta Pharm Sin B*, vol. 12, no. 7, p. 3049, Jul. 2022, doi: 10.1016/J.APSB.2022.02.002.

[10] M. K. Ediriweera, K. H. Tennekoon, and S. R. Samarakoon, "In vitro assays and techniques utilized in anticancer drug discovery," *Journal of Applied Toxicology*, vol. 39, no. 1, pp. 38–71, Jan. 2019, doi: 10.1002/JAT.3658.

[11] T. M. DesRochers, E. Palma, and D. L. Kaplan, "Tissue-engineered kidney disease models," *Adv Drug Deliv Rev*, vol. 69–70, pp. 67–80, Apr. 2014, doi: 10.1016/J.ADDR.2013.12.002.

[12] A. Monks *et al.*, "Feasibility of a High-Flux Anticancer Drug Screen Using a Diverse Panel of Cultured Human Tumor Cell Lines," *JNCI: Journal of the National Cancer Institute*, vol. 83, no. 11, pp. 757–766, Jun. 1991, doi: 10.1093/JNCI/83.11.757.

[13] V. Foglizzo, E. Cocco, and S. Marchiò, "Advanced Cellular Models for Preclinical Drug Testing: From 2D Cultures to Organ-on-a-Chip Technology," *Cancers (Basel)*, vol. 14, no. 15, Aug. 2022, doi: 10.3390/CANCERS14153692.

[14] M. Richter, O. Piwocka, M. Musielak, I. Piotrowski, W. M. Suchorska, and T. Trzeciak, "From Donor to the Lab: A Fascinating Journey of Primary Cell Lines," *Front Cell Dev Biol*, vol. 9, p. 711381, Jul. 2021, doi: 10.3389/FCELL.2021.711381/BIBTEX.

[15] “Comparison of 2D- and 3D-culture models as drug-testing platforms in breast cancer.” Accessed: Feb. 23, 2024. [Online]. Available: https://www.spandidos-publications.com/10.3892/or.2015.3767
[16] D. W. Shineman *et al.*, “Accelerating drug discovery for Alzheimer’s disease: Best practices for preclinical animal studies,” *Alzheimers Res Ther*, vol. 3, no. 5, pp. 1–13, Sep. 2011, doi: 10.1186/ALZRT90/TABLES/4.
[17] P. Bateson, “Robustness and plasticity in development,” *Wiley Interdiscip Rev Cogn Sci*, vol. 8, no. 1–2, p. e1386, Jan. 2017, doi: 10.1002/WCS.1386.
[18] L. L. Bischel, K. E. Sung, J. A. Jiménez-Torres, B. Mader, P. J. Keely, and D. J. Beebe, “The importance of being a lumen,” *The FASEB Journal*, vol. 28, no. 11, pp. 4583–4590, Nov. 2014, doi: 10.1096/FJ.13-243733.
[19] D. Huh *et al.*, “Microfabrication of human organs-on-chips,” *Nat Protoc*, vol. 8, no. 11, pp. 2135–2157, Nov. 2013, doi: 10.1038/nprot.2013.137.
[20] S. Caddeo, M. Boffito, and S. Sartori, “Tissue Engineering Approaches in the Design of Healthy and Pathological In Vitro Tissue Models,” *Front Bioeng Biotechnol*, vol. 5, no. AUG, Jul. 2017, doi: 10.3389/FBIOE.2017.00040.
[21] C. M. Moysidou, C. Barberio, and R. M. Owens, “Advances in Engineering Human Tissue Models,” *Front Bioeng Biotechnol*, vol. 8, p. 620962, Jan. 2020, doi: 10.3389/FBIOE.2020.620962.
[22] P. Occhetta, N. Sadr, F. Piraino, A. Redaelli, M. Moretti, and M. Rasponi, “Fabrication of 3D cell-laden hydrogel microstructures through photo-mold patterning,” *Biofabrication*, vol. 5, no. 3, p. 035002, May 2013, doi: 10.1088/1758-5082/5/3/035002.
[23] P. Occhetta, N. Sadr, F. Piraino, A. Redaelli, M. Moretti, and M. Rasponi, “Fabrication of 3D cell-laden hydrogel microstructures through photo-mold patterning,” *Biofabrication*, vol. 5, no. 3, p. 035002, May 2013, doi: 10.1088/1758-5082/5/3/035002.
[24] N. Gupta, J. R. Liu, B. Patel, D. E. Solomon, B. Vaidya, and V. Gupta, “Microfluidics-based 3D cell culture models: Utility in novel drug discovery and delivery research,” *Bioeng Transl Med*, vol. 1, no. 1, pp. 63–81, Mar. 2016, doi: 10.1002/btm2.10013.
[25] Y. Seon Kim, M. Majid, A. J. Melchiorri, A. G. Mikos, G. Mikos, and K. E. Y W O R D S bioink, “Applications of decellularized extracellular matrix in bone and cartilage tissue engineering,” *Bioeng Transl Med*, vol. 4, no. 1, pp. 83–95, Jan. 2019, doi: 10.1002/BTM2.10110.
[26] W. H. Abuwatfa, W. G. Pitt, and G. A. Husseini, “Scaffold-based 3D cell culture models in cancer research,” *Journal of Biomedical Science 2024 31:1*, vol. 31, no. 1, pp. 1–39, Jan. 2024, doi: 10.1186/S12929-024-00994-Y.
[27] N. Gjorevski *et al.*, “Tissue geometry drives deterministic organoid patterning,” *Science (1979)*, vol. 375, no. 6576, Jan. 2022, doi: 10.1126/science.aaw9021.
[28] A. Loewa, J. J. Feng, and S. Hedtrich, “Human disease models in drug development,” *Nature Reviews Bioengineering*, vol. 1, no. 8, pp. 545–559, May 2023, doi: 10.1038/s44222-023-00063-3.
[29] S. NajafiKhoshnoo *et al.*, “A 3D Nanomaterials-Printed Wearable, Battery-Free, Biocompatible, Flexible, and Wireless pH Sensor System for Real-Time Health Monitoring,” *Adv Mater Technol*, vol. 8, no. 8, Apr. 2023, doi: 10.1002/admt.202201655.

[30] W. H. 'Charles, T. S. 'Stuart, and W. L. 'Charles, "Stereolithographic Curl Reduction US, US 5772947 A 1998 ," 1998
[31] P. Wang, Y. Sun, X. Shi, H. Shen, H. Ning, and H. Liu, "3D printing of tissue engineering scaffolds: a focus on vascular regeneration," *Biodes Manuf*, vol. 4, no. 2, pp. 344–378, Jun. 2021, doi: 10.1007/s42242-020-00109-0.
[32] J. Zhang, E. Wehrle, M. Rubert, and R. Müller, "3D Bioprinting of Human Tissues: Biofabrication, Bioinks, and Bioreactors," *Int J Mol Sci*, vol. 22, no. 8, p. 3971, Apr. 2021, doi: 10.3390/ijms22083971.
[33] E. S. Bishop *et al.*, "3-D bioprinting technologies in tissue engineering and regenerative medicine: Current and future trends," *Genes Dis*, vol. 4, no. 4, pp. 185–195, Dec. 2017, doi: 10.1016/j.gendis.2017.10.002.
[34] N. Ashammakhi *et al.*, "Bioinks and bioprinting technologies to make heterogeneous and biomimetic tissue constructs," *Mater Today Bio*, vol. 1, p. 100008, Jan. 2019, doi: 10.1016/J.MTBIO.2019.100008.
[35] A. N. Leberfinger *et al.*, "Bioprinting functional tissues," *Acta Biomater*, vol. 95, pp. 32–49, Sep. 2019, doi: 10.1016/j.actbio.2019.01.009.
[36] P. S. Gungor-Ozkerim, I. Inci, Y. S. Zhang, A. Khademhosseini, and M. R. Dokmeci, "Bioinks for 3D bioprinting: an overview," *Biomater Sci*, vol. 6, no. 5, pp. 915–946, 2018, doi: 10.1039/C7BM00765E.
[37] S. B. Gugulothu, S. Asthana, S. Homer-Vanniasinkam, and K. Chatterjee, "Trends in Photopolymerizable Bioinks for 3D Bioprinting of Tumor Models," *JACS Au*, vol. 3, no. 8, pp. 2086–2106, Aug. 2023, doi: 10.1021/jacsau.3c00281.
[38] X. B. Chen *et al.*, "Biomaterials / bioinks and extrusion bioprinting," *Bioact Mater*, vol. 28, pp. 511–536, Oct. 2023, doi: 10.1016/J.BIOACTMAT.2023.06.006.
[39] M. Askari, M. Afzali Naniz, M. Kouhi, A. Saberi, A. Zolfagharian, and M. Bodaghi, "Recent progress in extrusion 3D bioprinting of hydrogel biomaterials for tissue regeneration: a comprehensive review with focus on advanced fabrication techniques," *Biomater Sci*, vol. 9, no. 3, pp. 535–573, Feb. 2021, doi: 10.1039/D0BM00973C.
[40] A. Malekpour and X. Chen, "Printability and Cell Viability in Extrusion-Based Bioprinting from Experimental, Computational, and Machine Learning Views," *Journal of Functional Biomaterials 2022, Vol. 13, Page 40*, vol. 13, no. 2, p. 40, Apr. 2022, doi: 10.3390/JFB13020040.
[41] D. Huang *et al.*, "Reversed-engineered human alveolar lung-on-a-chip model," *Proc Natl Acad Sci U S A*, vol. 118, no. 19, May 2021, doi: 10.1073/PNAS.2016146118/VIDEO-4.
[42] Y. Huo *et al.*, "Functional Trachea Reconstruction Using 3D-Bioprinted Native-Like Tissue Architecture Based on Designable Tissue-Specific Bioinks," *Advanced Science*, vol. 9, no. 29, p. 2202181, Oct. 2022, doi: 10.1002/ADVS.202202181.
[43] D. B. Kolesky, K. A. Homan, M. A. Skylar-Scott, and J. A. Lewis, "Three-dimensional bioprinting of thick vascularized tissues," *Proc Natl Acad Sci U S A*, vol. 113, no. 12, pp. 3179–3184, Mar. 2016, doi: 10.1073/PNAS.1521342113/SUPPL_FILE/PNAS.1521342113.SM04.MP4.
[44] D. B. Kolesky, R. L. Truby, A. S. Gladman, T. A. Busbee, K. A. Homan, and J. A. Lewis, "3D Bioprinting of Vascularized, Heterogeneous Cell-Laden Tissue Constructs," *Advanced Materials*, vol. 26, no. 19, pp. 3124–3130, May 2014, doi: 10.1002/adma.201305506.

[45] A. Lee *et al.*, “3D bioprinting of collagen to rebuild components of the human heart,” *Science (1979)*, vol. 365, no. 6452, pp. 482–487, Aug. 2019, doi: 10.1126/SCIENCE.AAV9051/SUPPL_FILE/AAV9051S9.MP4.
[46] E. R. Mears, F. Modabber, R. Don, and G. E. Johnson, “A Review: The Current In Vivo Models for the Discovery and Utility of New Anti-leishmanial Drugs Targeting Cutaneous Leishmaniasis,” *PLoS Negl Trop Dis*, vol. 9, no. 9, p. e0003889, Sep. 2015, doi: 10.1371/JOURNAL.PNTD.0003889.
[47] M. Kapałczyńska *et al.*, “2D and 3D cell cultures – a comparison of different types of cancer cell cultures,” *Arch Med Sci*, vol. 14, no. 4, p. 910, 2018, doi: 10.5114/AOMS.2016.63743.
[48] M. Zoetemelk, M. Rausch, D. J. Colin, O. Dormond, and P. Nowak-Sliwinska, “Short-term 3D culture systems of various complexity for treatment optimization of colorectal carcinoma,” *Scientific Reports 2019 9:1*, vol. 9, no. 1, pp. 1–14, May 2019, doi: 10.1038/s41598-019-42836-0.
[49] C. Jubelin *et al.*, “Three-dimensional in vitro culture models in oncology research,” *Cell & Bioscience 2022 12:1*, vol. 12, no. 1, pp. 1–28, Sep. 2022, doi: 10.1186/S13578-022-00887-3.
[50] C. Corrò, L. Novellasdemunt, and V. S. W. Li, “Making Cell Culture More Physiological: A brief history of organoids,” *Am J Physiol Cell Physiol*, vol. 319, no. 1, p. C151, Jul. 2020, doi: 10.1152/AJPCELL.00120.2020.
[51] S. Yang *et al.*, “Organoids: The current status and biomedical applications,” *MedComm (Beijing)*, vol. 4, no. 3, Jun. 2023, doi: 10.1002/MCO2.274.
[52] S. Pun, L. C. Haney, and R. Barrile, “Modelling Human Physiology on-Chip: Historical Perspectives and Future Directions,” *Micromachines 2021, Vol. 12, Page 1250*, vol. 12, no. 10, p. 1250, Oct. 2021, doi: 10.3390/MI12101250.
[53] S. F. Berlanda, M. Breitfeld, C. L. Dietsche, and P. S. Dittrich, “Recent Advances in Microfluidic Technology for Bioanalysis and Diagnostics,” *Anal Chem*, vol. 93, no. 1, pp. 311–331, Jan. 2021, doi: 10.1021/ACS.ANALCHEM.0C04366/ASSET/IMAGES/LARGE/AC0C04366_0006.JPEG.
[54] J. M. Ayuso, M. Virumbrales-Muñoz, J. M. Lang, and D. J. Beebe, “A role for microfluidic systems in precision medicine,” *Nat Commun*, vol. 13, no. 1, Dec. 2022, doi: 10.1038/S41467-022-30384-7.
[55] A. Loewa, J. J. Feng, and S. Hedtrich, “Human disease models in drug development,” *Nature Reviews Bioengineering 2023 1:8*, vol. 1, no. 8, pp. 545–559, May 2023, doi: 10.1038/s44222-023-00063-3.
[56] D. Ho *et al.*, “Enabling technologies for personalized and precision medicine,” *Trends Biotechnol*, vol. 38, no. 5, p. 497, May 2020, doi: 10.1016/J.TIBTECH.2019.12.021.
[57] A. Mazzocchi, S. Soker, and A. Skardal, “3D bioprinting for high-throughput screening: Drug screening, disease modeling, and precision medicine applications,” *Appl Phys Rev*, vol. 6, no. 1, Mar. 2019, doi: 10.1063/1.5056188.
[58] I. Marei *et al.*, “3D Tissue-Engineered Vascular Drug Screening Platforms: Promise and Considerations,” *Front Cardiovasc Med*, vol. 9, p. 847554, Mar. 2022, doi: 10.3389/FCVM.2022.847554.

[59] D. D. Shah, N. R. Raghani, M. R. Chorawala, S. Singh, and B. G. Prajapati, “Harnessing three-dimensional (3D) cell culture models for pulmonary infections: State of the art and future directions,” *Naunyn-Schmiedeberg’s Archives of Pharmacology 2023 396:11*, vol. 396, no. 11, pp. 2861–2880, Jun. 2023, doi: 10.1007/S00210-023-02541-2.
[60] J. Pusch *et al.*, “The physiological performance of a three-dimensional model that mimics the microenvironment of the small intestine,” *Biomaterials*, vol. 32, no. 30, pp. 7469–7478, Oct. 2011, doi: 10.1016/J.BIOMATERIALS.2011.06.035.
[61] V. Bosáková *et al.*, “Lung Organoids—The Ultimate Tool to Dissect Pulmonary Diseases?,” *Front Cell Dev Biol*, vol. 10, p. 899368, Jul. 2022, doi: 10.3389/FCELL.2022.899368/BIBTEX.
[62] C. M. Leung *et al.*, “A guide to the organ-on-a-chip,” *Nature Reviews Methods Primers 2022 2:1*, vol. 2, no. 1, pp. 1–29, May 2022, doi: 10.1038/s43586-022-00118-6.
[63] M. Hofer and M. P. Lutolf, “Engineering organoids,” *Nat Rev Mater*, vol. 6, no. 5, p. 402, May 2021, doi: 10.1038/S41578-021-00279-Y.
[64] S. Yang *et al.*, “Organoids: The current status and biomedical applications,” *MedComm (Beijing)*, vol. 4, no. 3, Jun. 2023, doi: 10.1002/MCO2.274.
[65] E. Suarez-Martinez, I. Suazo-Sanchez, M. Celis-Romero, and A. Carnero, “3D and organoid culture in research: physiology, hereditary genetic diseases and cancer,” *Cell Biosci*, vol. 12, no. 1, pp. 1–19, Dec. 2022, doi: 10.1186/S13578-022-00775-W/TABLES/1.
[66] G. Kaushik, M. P. Ponnusamy, and S. K. Batra, “Concise Review: Current Status of Three-Dimensional Organoids as Preclinical Models,” *Stem Cells*, vol. 36, no. 9, pp. 1329–1340, Sep. 2018, doi: 10.1002/STEM.2852.
[67] M. R. Blatchley and K. S. Anseth, “Middle-out methods for spatiotemporal tissue engineering of organoids,” *Nature Reviews Bioengineering 2023 1:5*, vol. 1, no. 5, pp. 329–345, Mar. 2023, doi: 10.1038/s44222-023-00039-3.
[68] J. M. Unagolla and A. C. Jayasuriya, “Recent advances in organoid engineering: A comprehensive review,” *Appl Mater Today*, vol. 29, Dec. 2022, doi: 10.1016/J.APMT.2022.101582.
[69] R. E. Ajalik *et al.*, “Human Organ-on-a-Chip Microphysiological Systems to Model Musculoskeletal Pathologies and Accelerate Therapeutic Discovery,” *Front Bioeng Biotechnol*, vol. 10, p. 846230, Mar. 2022, doi: 10.3389/FBIOE.2022.846230/BIBTEX.
[70] C. M. Leung *et al.*, “A guide to the organ-on-a-chip,” *Nature Reviews Methods Primers 2022 2:1*, vol. 2, no. 1, pp. 1–29, May 2022, doi: 10.1038/s43586-022-00118-6.
[71] A. Jurj, S. Pasca, C. Braicu, I. Rusu, S. S. Korban, and I. Berindan-Neagoe, “Focus on organoids: cooperation and interconnection with extracellular vesicles – Is this the future of in vitro modeling?,” *Semin Cancer Biol*, vol. 86, pp. 367–381, Nov. 2022, doi: 10.1016/J.SEMCANCER.2021.12.002.
[72] Z. Zhao *et al.*, “Organoids,” *Nature reviews. Methods primers*, vol. 2, no. 1, Dec. 2022, doi: 10.1038/S43586-022-00174-Y.
[73] M. Rodrigues, N. Kosaric, C. A. Bonham, and G. C. Gurtner, “Wound healing: A cellular perspective,” *Physiol Rev*, vol. 99, no. 1, pp. 665–706, Jan. 2019, doi: 10.1152/PHYSREV.00067.2017/ASSET/IMAGES/LARGE/Z9J0041828900006.JPEG.

[74] M. Chehelgerdi *et al.*, "Progressing nanotechnology to improve targeted cancer treatment: overcoming hurdles in its clinical implementation," *Mol Cancer*, vol. 22, no. 1, pp. 1–103, Dec. 2023, doi: 10.1186/S12943-023-01865-0/TABLES/15.

[75] M. J. Mitchell, M. M. Billingsley, R. M. Haley, M. E. Wechsler, N. A. Peppas, and R. Langer, "Engineering precision nanoparticles for drug delivery," *Nature Reviews Drug Discovery 2020 20:2*, vol. 20, no. 2, pp. 101–124, Dec. 2020, doi: 10.1038/s41573-020-0090-8.

[76] K. Perera, R. Ivone, E. Natekin, C. A. Wilga, J. Shen, and J. U. Menon, "3D Bioprinted Implants for Cartilage Repair in Intervertebral Discs and Knee Menisci," *Front Bioeng Biotechnol*, vol. 9, p. 754113, Oct. 2021, doi: 10.3389/FBIOE.2021.754113/BIBTEX.

[77] E. Murphy *et al.*, "Mitochondrial Function, Biology, and Role in Disease," *Circ Res*, vol. 118, no. 12, pp. 1960–1991, Jun. 2016, doi: 10.1161/RES.0000000000000104.

[78] G. Bassi, M. A. Grimaudo, S. Panseri, and M. Montesi, "Advanced Multi-Dimensional Cellular Models as Emerging Reality to Reproduce In Vitro the Human Body Complexity," *Int J Mol Sci*, vol. 22, no. 3, pp. 1–28, Feb. 2021, doi: 10.3390/IJMS22031195.

[79] T. Ahmed, "Organ-on-a-chip microengineering for bio-mimicking disease models and revolutionizing drug discovery," *Biosens Bioelectron X*, vol. 11, p. 100194, Sep. 2022, doi: 10.1016/J.BIOSX.2022.100194.

[80] A. Dozzo, A. Galvin, J. W. Shin, S. Scalia, C. M. O'Driscoll, and K. B. Ryan, "Modelling acute myeloid leukemia (AML): What's new? A transition from the classical to the modern," *Drug Delivery and Translational Research 2022 13:8*, vol. 13, no. 8, pp. 2110–2141, Aug. 2022, doi: 10.1007/S13346-022-01189-4.

[81] E. M. Dehne, T. Hasenberg, and U. Marx, "The ascendance of microphysiological systems to solve the drug testing dilemma," *Future Sci OA*, vol. 3, no. 2, May 2017, doi: 10.4155/FSOA-2017-0002/ASSET/IMAGES/LARGE/FIGURE3.JPEG.

[82] D. J. Shiwarski, A. R. Hudson, J. W. Tashman, and A. W. Feinberg, "Emergence of FRESH 3D printing as a platform for advanced tissue biofabrication," *APL Bioeng*, vol. 5, no. 1, p. 10904, Mar. 2021, doi: 10.1063/5.0032777.

[83] H. G. Yi, H. Kim, J. Kwon, Y. J. Choi, J. Jang, and D. W. Cho, "Application of 3D bioprinting in the prevention and the therapy for human diseases," *Signal Transduction and Targeted Therapy 2021 6:1*, vol. 6, no. 1, pp. 1–17, May 2021, doi: 10.1038/s41392-021-00566-8.

[84] J. Yu *et al.*, "Current Advances in 3D Bioprinting Technology and Its Applications for Tissue Engineering," *Polymers 2020, Vol. 12, Page 2958*, vol. 12, no. 12, p. 2958, Dec. 2020, doi: 10.3390/POLYM12122958.

[85] Ž. P. Kačarević *et al.*, "An Introduction to 3D Bioprinting: Possibilities, Challenges and Future Aspects," *Materials*, vol. 11, no. 11, Nov. 2018, doi: 10.3390/MA11112199.

[86] B. Zhang, L. Gao, L. Ma, Y. Luo, H. Yang, and Z. Cui, "3D Bioprinting: A Novel Avenue for Manufacturing Tissues and Organs," *Engineering*, vol. 5, no. 4, pp. 777–794, Aug. 2019, doi: 10.1016/J.ENG.2019.03.009.

[87] Z. Gu, J. Fu, H. Lin, and Y. He, "Development of 3D bioprinting: From printing methods to biomedical applications," *Asian J Pharm Sci*, vol. 15, no. 5, pp. 529–557, Sep. 2020, doi: 10.1016/J.AJPS.2019.11.003.

[88] S. NajafiKhoshnoo *et al.*, "A 3D Nanomaterials-Printed Wearable, Battery-Free, Biocompatible, Flexible, and Wireless pH Sensor System for Real-Time Health Monitoring," *Adv Mater Technol*, vol. 8, no. 8, 2023, doi: 10.1002/admt.202201655.

[89] P. Das, S. Najafikhoshnoo, J. A. Tavares-Negrete, Q. Yi, and R. Esfandyarpour, "An in-vivo-mimicking 3D lung cancer-on-a-chip model to study the effect of external stimulus on the progress and inhibition of cancer metastasis," *Bioprinting*, vol. 28, 2022, doi: 10.1016/j.bprint.2022.e00243.

[90] A. Schwab, R. Levato, M. D'Este, S. Piluso, D. Eglin, and J. Malda, "Printability and Shape Fidelity of Bioinks in 3D Bioprinting," *Chem Rev*, vol. 120, no. 19, pp. 11028–11055, Oct. 2020, doi: 10.1021/ACS.CHEMREV.0C00084/ASSET/IMAGES/LARGE/CR0C00084_0009.JPEG.

[91] H. Mao *et al.*, "Recent advances and challenges in materials for 3D bioprinting," *Progress in Natural Science: Materials International*, vol. 30, no. 5, pp. 618–634, Oct. 2020, doi: 10.1016/J.PNSC.2020.09.015.

[92] J. Zhang, E. Wehrle, M. Rubert, and R. Müller, "3D Bioprinting of Human Tissues: Biofabrication, Bioinks, and Bioreactors," *Int J Mol Sci*, vol. 22, no. 8, Apr. 2021, doi: 10.3390/IJMS22083971.

[93] N. Ashammakhi *et al.*, "Bioinks and bioprinting technologies to make heterogeneous and biomimetic tissue constructs," *Mater Today Bio*, vol. 1, p. 100008, Jan. 2019, doi: 10.1016/J.MTBIO.2019.100008.

[94] T. J. Hinton *et al.*, "Three-dimensional printing of complex biological structures by freeform reversible embedding of suspended hydrogels," *Sci Adv*, vol. 1, no. 9, Oct. 2015, doi: 10.1126/sciadv.1500758.

[95] A. Lee *et al.*, "3D bioprinting of collagen to rebuild components of the human heart," *Science (1979)*, vol. 365, no. 6452, pp. 482–487, Aug. 2019, doi: 10.1126/SCIENCE.AAV9051/SUPPL_FILE/AAV9051S9.MP4.

[96] D. Huang *et al.*, "Reversed-engineered human alveolar lung-on-a-chip model," *Proc Natl Acad Sci U S A*, vol. 118, no. 19, May 2021, doi: 10.1073/PNAS.2016146118/-/DCSUPPLEMENTAL.

[97] Y. Huo *et al.*, "Functional Trachea Reconstruction Using 3D-Bioprinted Native-Like Tissue Architecture Based on Designable Tissue-Specific Bioinks," *Advanced Science*, vol. 9, no. 29, p. 2202181, Oct. 2022, doi: 10.1002/ADVS.202202181.

[98] J. A. Brassard and M. P. Lutolf, "Engineering Stem Cell Self-organization to Build Better Organoids," *Cell Stem Cell*, vol. 24, no. 6, pp. 860–876, Jun. 2019, doi: 10.1016/j.stem.2019.05.005.

[99] C. M. Moysidou, C. Barberio, and R. M. Owens, "Advances in Engineering Human Tissue Models," *Front Bioeng Biotechnol*, vol. 8, p. 620962, Jan. 2020, doi: 10.3389/FBIOE.2020.620962.

[100] J. C. Rose and L. De Laporte, "Hierarchical Design of Tissue Regenerative Constructs," *Adv Healthc Mater*, vol. 7, no. 6, p. 1701067, Mar. 2018, doi: 10.1002/ADHM.201701067.

[101] Z. Zhao *et al.*, "Organoids," *Nature Reviews Methods Primers 2022 2:1*, vol. 2, no. 1, pp. 1–21, Dec. 2022, doi: 10.1038/s43586-022-00174-y.

[102] J. A. Brassard and M. P. Lutolf, "Engineering Stem Cell Self-organization to Build Better Organoids," *Cell Stem Cell*, vol. 24, no. 6, pp. 860–876, Jun. 2019, doi: 10.1016/J.STEM.2019.05.005.

[103] J. E. Bayne and M. A. Edmondson, "Diseases of the gastrointestinal system," *Sheep, Goat, and Cervid Medicine*, p. 63, Jan. 2021, doi: 10.1016/B978-0-323-62463-3.00014-1.

[104] “Anatomy of Colon and Rectum | SEER Training.” Accessed: Mar. 01, 2024. [Online]. Available: https://training.seer.cancer.gov/colorectal/anatomy/
[105] L. L. Azzouz and S. Sharma, “Physiology, Large Intestine,” *StatPearls*, Jul. 2023, Accessed: Mar. 01, 2024. [Online]. Available: https://www.ncbi.nlm.nih.gov/books/NBK507857/
[106] “NIH 3D - Large Intestine.” Accessed: Mar. 01, 2024. [Online]. Available: https://3d.nih.gov/entries/3dpx-002736
[107] C. Hu, W. Lu, C. Sun, Y. Zhao, Y. Zhang, and Y. Fang, “Gelation behavior and mechanism of alginate with calcium: Dependence on monovalent counterions,” *Carbohydr Polym*, vol. 294, p. 119788, Oct. 2022, doi: 10.1016/J.CARBPOL.2022.119788.
[108] S. I. Somo, J. M. Brown, and E. M. Brey, “Dual Crosslinking of Alginate Outer Layer Increases Stability of Encapsulation System,” *Front Chem*, vol. 8, p. 575278, Nov. 2020, doi: 10.3389/FCHEM.2020.575278.
[109] H. rae Cho, B. Y. Kim, K. Kim, D. Lee, S. K. Eo, and Y. Son, “27-Hydroxycholesterol induces expression of zonula occludens-1 in monocytic cells via multiple kinases pathways,” *Scientific Reports 2022 12:1*, vol. 12, no. 1, pp. 1–10, May 2022, doi: 10.1038/s41598-022-12416-w.
[110] E. McNeil, C. T. Capaldo, and I. G. Macara, “Zonula Occludens-1 Function in the Assembly of Tight Junctions in Madin-Darby Canine Kidney Epithelial Cells,” *Mol Biol Cell*, vol. 17, no. 4, p. 1922, Apr. 2006, doi: 10.1091/MBC.E05-07-0650.
[111] W. T. Kuo *et al.*, “The tight junction protein ZO-1 is dispensable for barrier function but critical for effective mucosal repair,” *Gastroenterology*, vol. 161, no. 6, p. 1924, Dec. 2021, doi: 10.1053/J.GASTRO.2021.08.047.
[112] N. J. Darling, C. L. Mobbs, A. L. González-Hau, M. Freer, and S. Przyborski, “Bioengineering Novel in vitro Co-culture Models That Represent the Human Intestinal Mucosa With Improved Caco-2 Structure and Barrier Function,” *Front Bioeng Biotechnol*, vol. 8, p. 538834, Aug. 2020, doi: 10.3389/FBIOE.2020.00992/BIBTEX.
[113] W. Shin and H. J. Kim, “3D in vitro morphogenesis of human intestinal epithelium in a gut-on-a-chip or a hybrid chip with a cell culture insert,” *Nature Protocols 2022 17:3*, vol. 17, no. 3, pp. 910–939, Feb. 2022, doi: 10.1038/s41596-021-00674-3.
[114] H. Y. Tan, S. Trier, U. L. Rahbek, M. Dufva, J. P. Kutter, and T. L. Andresen, “A multi-chamber microfluidic intestinal barrier model using Caco-2 cells for drug transport studies,” *PLoS One*, vol. 13, no. 5, p. e0197101, May 2018, doi: 10.1371/JOURNAL.PONE.0197101.
[115] B. Srinivasan, A. R. Kolli, M. B. Esch, H. E. Abaci, M. L. Shuler, and J. J. Hickman, “TEER Measurement Techniques for In Vitro Barrier Model Systems,” *J Lab Autom*, vol. 20, no. 2, pp. 107–126, Apr. 2015, doi: 10.1177/2211068214561025/ASSET/IMAGES/LARGE/10.1177_2211068214561025-FIG6.JPEG.
[116] B. Srinivasan, A. R. Kolli, M. B. Esch, H. E. Abaci, M. L. Shuler, and J. J. Hickman, “TEER measurement techniques for in vitro barrier model systems,” *J Lab Autom*, vol. 20, no. 2, p. 107, Apr. 2015, doi: 10.1177/2211068214561025.
[117] B. Srinivasan, A. R. Kolli, M. B. Esch, H. E. Abaci, M. L. Shuler, and J. J. Hickman, “TEER Measurement Techniques for In Vitro Barrier Model Systems,” *SLAS Technol*, vol. 20, no. 2, pp. 107–126, Apr. 2015, doi: 10.1177/2211068214561025.

[118] M. Devarasetty, A. Dominijanni, S. Herberg, E. Shelkey, A. Skardal, and S. Soker, "Simulating the human colorectal cancer microenvironment in 3D tumor-stroma co-cultures in vitro and in vivo," *Scientific Reports 2020 10:1*, vol. 10, no. 1, pp. 1–14, Jun. 2020, doi: 10.1038/s41598-020-66785-1.
[119] L. B. Weiswald, D. Bellet, and V. Dangles-Marie, "Spherical Cancer Models in Tumor Biology," *Neoplasia*, vol. 17, no. 1, pp. 1–15, Jan. 2015, doi: 10.1016/J.NEO.2014.12.004.
[120] A. Mehta, M. Goswami, R. Sinha, and A. Dogra, "Histopathological Significance and Prognostic Impact of Tumor Budding in Colorectal Cancer," *Asian Pac J Cancer Prev*, vol. 19, no. 9, pp. 2447–2453, Sep. 2018, doi: 10.22034/APJCP.2018.19.9.2447.
[121] D. R. RUDY and M. J. ZDON, "Update on Colorectal Cancer," *Am Fam Physician*, vol. 61, no. 6, pp. 1759–1770, Mar. 2000, Accessed: Mar. 01, 2024. [Online]. Available: https://www.aafp.org/pubs/afp/issues/2000/0315/p1759.html
[122] Y. J. Lee *et al.*, "5-Fluorouracil as a Tumor-Treating Field-Sensitizer in Colon Cancer Therapy," *Cancers 2019, Vol. 11, Page 1999*, vol. 11, no. 12, p. 1999, Dec. 2019, doi: 10.3390/CANCERS11121999.
[123] C. Adam *et al.*, "A 5-FU Precursor Designed to Evade Anabolic and Catabolic Drug Pathways and Activated by Pd Chemistry in Vitro and in Vivo," *J Med Chem*, vol. 65, no. 1, pp. 552–561, Jan. 2022, doi: 10.1021/ACS.JMEDCHEM.1C01733/SUPPL_FILE/JM1C01733_SI_005.PDB.
[124] Y. Chen *et al.*, "Bi-Layered Tubular Microfiber Scaffolds as Functional Templates for Engineering Human Intestinal Smooth Muscle Tissue," *Adv Funct Mater*, vol. 30, no. 17, p. 2000543, Apr. 2020, doi: 10.1002/ADFM.202000543.
[125] S. E. Rudolph *et al.*, "Crypt-Villus Scaffold Architecture for Bioengineering Functional Human Intestinal Epithelium," *ACS Biomater Sci Eng*, vol. 8, no. 11, pp. 4942–4955, Nov. 2022, doi: 10.1021/ACSBIOMATERIALS.2C00851/ASSET/IMAGES/LARGE/AB2C00851_0007.JPEG.
[126] L. Cheng *et al.*, "A 3D Bioprinted Gut Anaerobic Model for Studying Bacteria–Host Interactions," *Research*, vol. 6, Jan. 2023, doi: 10.34133/RESEARCH.0058/SUPPL_FILE/RESEARCH.0058.F2.ZIP.
[127] H. Han *et al.*, "A Bioprinted Tubular Intestine Model Using a Colon-Specific Extracellular Matrix Bioink," *Adv Healthc Mater*, vol. 11, no. 2, Jan. 2022, doi: 10.1002/ADHM.202101768.
[128] Y. Chen *et al.*, "Bioengineered 3D Tissue Model of Intestine Epithelium with Oxygen Gradients to Sustain Human Gut Microbiome," *Adv Healthc Mater*, vol. 11, no. 16, p. 2200447, Aug. 2022, doi: 10.1002/ADHM.202200447.
[129] N. Torras, J. Zabalo, E. Abril, A. Carré, M. García-Díaz, and E. Martínez, "A bioprinted 3D gut model with crypt-villus structures to mimic the intestinal epithelial-stromal microenvironment," *Biomaterials Advances*, vol. 153, p. 213534, Oct. 2023, doi: 10.1016/J.BIOADV.2023.213534.
[130] W. Kim and G. Kim, "Intestinal Villi Model with Blood Capillaries Fabricated Using Collagen-Based Bioink and Dual-Cell-Printing Process," *ACS Appl Mater Interfaces*, vol. 10, no. 48, pp. 41185–41196, Dec. 2018, doi: 10.1021/ACSAMI.8B17410.

[131] P. Rougerie *et al.*, "Topographical curvature is sufficient to control epithelium elongation," *Scientific Reports 2020 10:1*, vol. 10, no. 1, pp. 1–14, Sep. 2020, doi: 10.1038/s41598-020-70907-0.
[132] A. Marín-Llauradó *et al.*, "Mapping mechanical stress in curved epithelia of designed size and shape," *Nature Communications 2023 14:1*, vol. 14, no. 1, pp. 1–11, Jul. 2023, doi: 10.1038/s41467-023-38879-7.
[133] S. J. P. Callens, R. J. C. Uyttendaele, L. E. Fratila-Apachitei, and A. A. Zadpoor, "Substrate curvature as a cue to guide spatiotemporal cell and tissue organization," *Biomaterials*, vol. 232, p. 119739, Feb. 2020, doi: 10.1016/J.BIOMATERIALS.2019.119739.
[134] C. Pérez-González, G. Ceada, M. Matejčić, and X. Trepat, "Digesting the mechanobiology of the intestinal epithelium," *Curr Opin Genet Dev*, vol. 72, pp. 82–90, Feb. 2022, doi: 10.1016/J.GDE.2021.10.005.
[135] H. J. Kim and D. E. Ingber, "Gut-on-a-Chip microenvironment induces human intestinal cells to undergo villus differentiation," *Integrative Biology*, vol. 5, no. 9, p. 1130, 2013, doi: 10.1039/c3ib40126j.
[136] B. Pinto, A. C. Henriques, P. M. A. Silva, and H. Bousbaa, "Three-Dimensional Spheroids as In Vitro Preclinical Models for Cancer Research," *Pharmaceutics*, vol. 12, no. 12, pp. 1–38, Dec. 2020, doi: 10.3390/PHARMACEUTICS12121186.
[137] R. Edmondson, J. J. Broglie, A. F. Adcock, and L. Yang, "Three-Dimensional Cell Culture Systems and Their Applications in Drug Discovery and Cell-Based Biosensors," *Assay Drug Dev Technol*, vol. 12, no. 4, p. 207, May 2014, doi: 10.1089/ADT.2014.573.
[138] N. E. Ryu, S. H. Lee, and H. Park, "Spheroid Culture System Methods and Applications for Mesenchymal Stem Cells," *Cells*, vol. 8, no. 12, Dec. 2019, doi: 10.3390/CELLS8121620.
[139] M. Zoetemelk, M. Rausch, D. J. Colin, O. Dormond, and P. Nowak-Sliwinska, "Short-term 3D culture systems of various complexity for treatment optimization of colorectal carcinoma," *Sci Rep*, vol. 9, no. 1, Dec. 2019, doi: 10.1038/S41598-019-42836-0.
[140] P. S. Thakuri, C. Liu, G. D. Luker, and H. Tavana, "Biomaterials-Based Approaches to Tumor Spheroid and Organoid Modeling," *Adv Healthc Mater*, vol. 7, no. 6, Mar. 2018, doi: 10.1002/ADHM.201700980.
[141] Z. Zhao *et al.*, "Organoids," *Nature Reviews Methods Primers 2022 2:1*, vol. 2, no. 1, pp. 1–21, Dec. 2022, doi: 10.1038/s43586-022-00174-y.
[142] O. Habanjar, M. Diab-Assaf, F. Caldefie-Chezet, and L. Delort, "3D Cell Culture Systems: Tumor Application, Advantages, and Disadvantages," *Int J Mol Sci*, vol. 22, no. 22, Nov. 2021, doi: 10.3390/IJMS222212200.
[143] M. Blaschke *et al.*, "Measurements of 5-FU Plasma Concentrations in Patients with Gastrointestinal Cancer: 5-FU Levels Reflect the 5-FU Dose Applied," *J Cancer Ther*, vol. 3, no. 1, pp. 28–36, Feb. 2012, doi: 10.4236/JCT.2012.31004.
[144] M. Li *et al.*, "Drug monitoring detects under- and overdosing in patients receiving 5-fluorouracil-containing chemotherapy—results of a prospective, multicenter German observational study," *ESMO Open*, vol. 8, no. 2, p. 101201, Apr. 2023, doi: 10.1016/J.ESMOOP.2023.101201.
[145] B. Wang, M. Yao, L. Lv, Z. Ling, and L. Li, "The Human Microbiota in Health and Disease," *Engineering*, vol. 3, no. 1, pp. 71–82, 2017, doi: https://doi.org/10.1016/J.ENG.2017.01.008.

[146] D. Zheng, T. Liwinski, and E. Elinav, “Interaction between microbiota and immunity in health and disease,” *Cell Res*, vol. 30, no. 6, pp. 492–506, 2020, doi: 10.1038/s41422-020-0332-7.
[147] A. Thomas, Y. Chen, T. Yu, M. Jakopovic, and G. Giaccone, “Trends and characteristics of young non-small cell lung cancer patients in the United States,” *Front Oncol*, vol. 5, p. 113, 2015.
[148] K. C. Arbour and G. J. Riely, “Systemic therapy for locally advanced and metastatic non–small cell lung cancer: a review,” *JAMA*, vol. 322, no. 8, pp. 764–774, 2019.
[149] Q. Tingting *et al.*, “CHIP involves in non-small cell lung cancer prognosis through VEGF pathway,” *Biomedicine & Pharmacotherapy*, vol. 83, pp. 271–276, 2016.
[150] N. Del Piccolo *et al.*, “Tumor-on-chip modeling of organ-specific cancer and metastasis,” *Adv Drug Deliv Rev*, vol. 175, p. 113798, 2021.
[151] H. G. Thompson, D. T. Truong, C. K. Griffith, and S. C. George, “A three-dimensional in vitro model of angiogenesis in the airway mucosa,” *Pulm Pharmacol Ther*, vol. 20, no. 2, pp. 141–148, 2007.
[152] N. K. Malavia, J. D. Mih, C. B. Raub, B. T. Dinh, and S. C. George, “IL-13 induces a bronchial epithelial phenotype that is profibrotic,” *Respir Res*, vol. 9, no. 1, pp. 1–12, 2008.
[153] A. Spira *et al.*, “Effects of cigarette smoke on the human airway epithelial cell transcriptome,” *Proceedings of the National Academy of Sciences*, vol. 101, no. 27, pp. 10143–10148, 2004.
[154] E. Li *et al.*, “Continual exposure to cigarette smoke extracts induces tumor-like transformation of human nontumor bronchial epithelial cells in a microfluidic chip,” *Journal of Thoracic Oncology*, vol. 9, no. 8, pp. 1091–1100, 2014.
[155] K. H. Benam *et al.*, “Matched-Comparative Modeling of Normal and Diseased Human Airway Responses Using a Microengineered Breathing Lung Chip.,” *Cell Syst*, vol. 3 5, pp. 456-466.e4, 2016, [Online]. Available: https://api.semanticscholar.org/CorpusID:20821077
[156] A. T. Stratmann *et al.*, “Establishment of a human 3D lung cancer model based on a biological tissue matrix combined with a Boolean in silico model,” *Mol Oncol*, vol. 8, no. 2, pp. 351–365, 2014.
[157] C. Kniebs *et al.*, “Establishment of a pre-vascularized 3D lung cancer model in fibrin gel—influence of hypoxia and cancer-specific therapeutics,” *Front Bioeng Biotechnol*, vol. 9, p. 761846, 2021.
[158] Z. Xu *et al.*, “Design and construction of a multi-organ microfluidic chip mimicking the in vivo microenvironment of lung cancer metastasis,” *ACS Appl Mater Interfaces*, vol. 8, no. 39, pp. 25840–25847, 2016.
[159] X. Yang *et al.*, “Nanofiber membrane supported lung-on-a-chip microdevice for anti-cancer drug testing,” *Lab Chip*, vol. 18, no. 3, pp. 486–495, 2018.
[160] S. N. Bhatia and D. E. Ingber, “Microfluidic organs-on-chips,” *Nat Biotechnol*, vol. 32, no. 8, pp. 760–772, 2014.
[161] D. Huh, Y. Torisawa, G. A. Hamilton, H. J. Kim, and D. E. Ingber, “Microengineered physiological biomimicry: organs-on-chips,” *Lab Chip*, vol. 12, no. 12, pp. 2156–2164, 2012.

[162] R. Edmondson, J. J. Broglie, A. F. Adcock, and L. Yang, “Three-dimensional cell culture systems and their applications in drug discovery and cell-based biosensors,” *Assay Drug Dev Technol*, vol. 12, no. 4, pp. 207–218, 2014.
[163] F. Saleh, A. Harb, N. Soudani, and H. Zaraket, “A three-dimensional A549 cell culture model to study respiratory syncytial virus infections,” *J Infect Public Health*, vol. 13, no. 8, pp. 1142–1147, 2020.
[164] T. Kitamura, B. Qian, and J. W. Pollard, “Immune cell promotion of metastasis,” *Nat Rev Immunol*, vol. 15, pp. 73–86, 2015, [Online]. Available: https://api.semanticscholar.org/CorpusID:13952658
[165] B. Bigdelou *et al.*, “COVID-19 and preexisting comorbidities: Risks, synergies, and clinical outcomes,” *Front Immunol*, vol. 13, p. 890517, 2022.
[166] V. Velasco, S. A. Shariati, and R. Esfandyarpour, “Microtechnology-based methods for organoid models,” *Microsyst Nanoeng*, vol. 6, no. 1, p. 76, 2020.
[167] V. Velasco, K. Joshi, J. Chen, and R. Esfandyarpour, “Personalized drug efficacy monitoring chip,” *Anal Chem*, vol. 91, no. 23, pp. 14927–14935, 2019.
[168] R. Esfandyarpour, M. J. DiDonato, Y. Yang, N. G. Durmus, J. S. Harris, and R. W. Davis, “Multifunctional, inexpensive, and reusable nanoparticle-printed biochip for cell manipulation and diagnosis,” *Proceedings of the national academy of sciences*, vol. 114, no. 8, pp. E1306–E1315, 2017.
[169] N. Chaicharoenaudomrung, P. Kunhorm, and P. Noisa, “Three-dimensional cell culture systems as an in vitro platform for cancer and stem cell modeling,” *World J Stem Cells*, vol. 11, no. 12, p. 1065, 2019.
[170] D. Huang *et al.*, “Reversed-engineered human alveolar lung-on-a-chip model,” *Proceedings of the National Academy of Sciences*, vol. 118, no. 19, p. e2016146118, 2021.
[171] T. J. Hinton, A. Hudson, K. Pusch, A. Lee, and A. W. Feinberg, “3D printing PDMS elastomer in a hydrophilic support bath via freeform reversible embedding,” *ACS Biomater Sci Eng*, vol. 2, no. 10, pp. 1781–1786, 2016.
[172] J. Liu, H. Zheng, X. Dai, P. S. P. Poh, H.-G. Machens, and A. F. Schilling, “Transparent PDMS Bioreactors for the Fabrication and Analysis of Multi-Layer Pre-vascularized Hydrogels Under Continuous Perfusion,” *Front Bioeng Biotechnol*, vol. 8, 2020, [Online]. Available: https://api.semanticscholar.org/CorpusID:229356579
[173] R. Mazrouei, V. Velasco, and R. Esfandyarpour, “3D-bioprinted all-inclusive bioanalytical platforms for cell studies,” *Sci Rep*, vol. 10, 2020, [Online]. Available: https://api.semanticscholar.org/CorpusID:221502481
[174] L. Ouyang, J. P. K. Armstrong, Q. Chen, Y. Lin, and M. M. Stevens, “Void-free 3D Bioprinting for In-situ Endothelialization and Microfluidic Perfusion.,” *Adv Funct Mater*, vol. 30 26, p. 1909009, 2020, [Online]. Available: https://api.semanticscholar.org/CorpusID:249521332
[175] T. Kim, Q. Yi, E. Hoang, and R. Esfandyarpour, “A 3D Printed Wearable Bioelectronic Patch for Multi-Sensing and In Situ Sweat Electrolyte Monitoring,” *Adv Mater Technol*, vol. 6, 2021, [Online]. Available: https://api.semanticscholar.org/CorpusID:234110833
[176] Z. Galliger, C. D. Vogt, and A. Panoskaltsis-Mortari, “3D bioprinting for lungs and hollow organs.,” *Transl Res*, 2019, [Online]. Available: https://api.semanticscholar.org/CorpusID:172136988

[177] E. Taioli, “Gene-environment interaction in tobacco-related cancers.,” *Carcinogenesis*, vol. 29 8, pp. 1467–74, 2008, [Online]. Available: https://api.semanticscholar.org/CorpusID:16188303
[178] N. S. Nagathihalli, P. P. Massion, A. L. Gonzalez, P. Lu, and P. K. Datta, “Smoking Induces Epithelial-to-Mesenchymal Transition in Non–Small Cell Lung Cancer through HDAC-Mediated Downregulation of E-Cadherin,” *Mol Cancer Ther*, vol. 11, pp. 2362–2372, 2012, [Online]. Available: https://api.semanticscholar.org/CorpusID:11819698
[179] C. Xie *et al.*, “TAp63α Is Involved in Tobacco Smoke-Induced Lung Cancer EMT and the Anti-cancer Activity of Curcumin via miR-19 Transcriptional Suppression,” *Front Cell Dev Biol*, vol. 9, 2021, [Online]. Available: https://api.semanticscholar.org/CorpusID:232106951
[180] S. Zheng, A. K. El-Naggar, E. S. Kim, J. M. Kurie, and G. Lozano, “A genetic mouse model for metastatic lung cancer with gender differences in survival,” *Oncogene*, vol. 26, pp. 6896–6904, 2007, [Online]. Available: https://api.semanticscholar.org/CorpusID:41573893
[181] M. Shen *et al.*, “Inhibition of ATM reverses EMT and decreases metastatic potential of cisplatin-resistant lung cancer cells through JAK/STAT3/PD-L1 pathway,” *J Exp Clin Cancer Res*, vol. 38, 2019, [Online]. Available: https://api.semanticscholar.org/CorpusID:104295634
[182] N. J. Rothenberger and L. P. Stabile, “Induction of Lung Tumors and Mutational Analysis in FVB/N Mice Treated with the Tobacco Carcinogen 4-(Methylnitrosamino)-1-(3-Pyridyl)-1-Butanone.,” *Methods in molecular biology*, vol. 2102, pp. 149–160, 2020, [Online]. Available: https://api.semanticscholar.org/CorpusID:210935526
[183] F.-L. Chung, “The prevention of lung cancer induced by a tobacco-specific carcinogen in rodents by green and black Tea.,” *Proceedings of the Society for Experimental Biology and Medicine. Society for Experimental Biology and Medicine*, vol. 220 4, pp. 244–8, 1999, [Online]. Available: https://api.semanticscholar.org/CorpusID:21606985
[184] A. Jousset, B. Schmid, S. Scheu, N. Eisenhauer, and N. Eisenhauer, “Genotypic richness and dissimilarity opposingly affect ecosystem functioning.,” *Ecol Lett*, vol. 14 6, pp. 537–45, 2011, [Online]. Available: https://api.semanticscholar.org/CorpusID:30870813
[185] P. N. Fonkwo, “Pricing infectious disease,” *EMBO Rep*, vol. 9, no. S1, pp. S13–S17, 2008, doi: https://doi.org/10.1038/embor.2008.110.
[186] G. A. Van Norman, “Limitations of Animal Studies for Predicting Toxicity in Clinical Trials: Is it Time to Rethink Our Current Approach?,” *JACC Basic Transl Sci*, vol. 4, no. 7, pp. 845–854, 2019, doi: https://doi.org/10.1016/j.jacbts.2019.10.008.
[187] K. A. Foster, C. G. Oster, M. M. Mayer, M. L. Avery, and K. L. Audus, “Characterization of the A549 Cell Line as a Type II Pulmonary Epithelial Cell Model for Drug Metabolism,” *Exp Cell Res*, vol. 243, no. 2, pp. 359–366, 1998, doi: https://doi.org/10.1006/excr.1998.4172.
[188] S. M. Ehsan, K. M. Welch-Reardon, M. L. Waterman, C. C. W. Hughes, and S. George, “A three-dimensional in vitro model of tumor cell intravasation.,” *Integr Biol (Camb)*, vol. 6 6, pp. 603–10, 2014, [Online]. Available: https://api.semanticscholar.org/CorpusID:13753746
[189] M. M. Lieber, G. J. Todaro, B. H. Smith, A. Szakal, and W. A. Nelson-Rees, “A continuous tumor-cell line from a human lung carcinoma with properties of type II alveolar epithelial

cells," *Int J Cancer*, vol. 17, 1976, [Online]. Available: https://api.semanticscholar.org/CorpusID:11096734
[190] D. J. Giard *et al.*, "In vitro cultivation of human tumors: establishment of cell lines derived from a series of solid tumors.," *J Natl Cancer Inst*, vol. 51 5, pp. 1417–23, 1973, [Online]. Available: https://api.semanticscholar.org/CorpusID:26567648
[191] A. F. Irvine, S. Waise, E. Green, B. Stuart, and G. J. Thomas, "Characterising cancer-associated fibroblast heterogeneity in non-small cell lung cancer: a systematic review and meta-analysis," *Sci Rep*, vol. 11, 2021, [Online]. Available: https://api.semanticscholar.org/CorpusID:231911468
[192] L. Wang *et al.*, "Cancer-associated fibroblasts enhance metastatic potential of lung cancer cells through IL-6/STAT3 signaling pathway," *Oncotarget*, vol. 8, pp. 76116–76128, 2017, [Online]. Available: https://api.semanticscholar.org/CorpusID:27501634
[193] J.-P. Coppé *et al.*, "A Role for Fibroblasts in Mediating the Effects of Tobacco-Induced Epithelial Cell Growth and Invasion," *Molecular Cancer Research*, vol. 6, pp. 1085–1098, 2008, [Online]. Available: https://api.semanticscholar.org/CorpusID:1192458
[194] Z.-Z. Cao, Y. Ao, and S. Zhou, "The role of cancer stromal fibroblasts in mediating the effects of tobacco-induced cancer cell growth," *Cancer Cell Int*, vol. 21, 2021, [Online]. Available: https://api.semanticscholar.org/CorpusID:245476049
[195] B. A. Weaver, "How Taxol/paclitaxel kills cancer cells," *Mol Biol Cell*, vol. 25, pp. 2677–2681, 2014, [Online]. Available: https://api.semanticscholar.org/CorpusID:11342439
[196] C. D. Scripture, W. D. Figg, and A. Sparreboom, "Paclitaxel chemotherapy: from empiricism to a mechanism-based formulation strategy," *Ther Clin Risk Manag*, vol. 1, pp. 107–114, 2005, [Online]. Available: https://api.semanticscholar.org/CorpusID:13968165
[197] W. L. Akerley, "Paclitaxel in advanced non-small cell lung cancer : an alternative high-dose weekly schedule.," *Chest*, vol. 117 4 Suppl 1, pp. 152S-155S, 2000, [Online]. Available: https://api.semanticscholar.org/CorpusID:25496880
[198] J. Lee *et al.*, "A Heart-Breast Cancer-on-a-Chip Platform for Disease Modeling and Monitoring of Cardiotoxicity Induced by Cancer Chemotherapy.," *Small*, p. e2004258, 2020, [Online]. Available: https://api.semanticscholar.org/CorpusID:225051526
[199] B. M. Koeppen, "1 – Physiology of Body Fluids," 2013. [Online]. Available: https://api.semanticscholar.org/CorpusID:89273402
[200] R. J. McMurtrey, "Analytic Models of Oxygen and Nutrient Diffusion, Metabolism Dynamics, and Architecture Optimization in Three-Dimensional Tissue Constructs with Applications and Insights in Cerebral Organoids," *Tissue Eng Part C Methods*, vol. 22, pp. 221–249, 2015, [Online]. Available: https://api.semanticscholar.org/CorpusID:10435617
[201] D. Baldassi, B. Gabold, and O. M. Merkel, "Air-liquid interface cultures of the healthy and diseased human respiratory tract: promises, challenges and future directions.," *Adv Nanobiomed Res*, vol. 1 6, 2021, [Online]. Available: https://api.semanticscholar.org/CorpusID:236617782
[202] M. W. Toepke and D. J. Beebe, "PDMS absorption of small molecules and consequences in microfluidic applications.," *Lab Chip*, vol. 6 12, pp. 1484–6, 2006, [Online]. Available: https://api.semanticscholar.org/CorpusID:40391819

[203] B. van Meer *et al.*, “Small molecule absorption by PDMS in the context of drug response bioassays,” *Biochem Biophys Res Commun*, vol. 482, pp. 323–328, 2017, [Online]. Available: https://api.semanticscholar.org/CorpusID:26466692
[204] S. R. Polio *et al.*, “Cross-platform mechanical characterization of lung tissue,” *PLoS One*, vol. 13, 2018, [Online]. Available: https://api.semanticscholar.org/CorpusID:52988936
[205] J. Prakash, “The Tumor Stroma: Key Component of Solid Tumors,” *The Tumor Stroma*, 2021, [Online]. Available: https://api.semanticscholar.org/CorpusID:245201878
[206] C. C. Tièche *et al.*, “Tumor Initiation Capacity and Therapy Resistance Are Differential Features of EMT-Related Subpopulations in the NSCLC Cell Line A5491,” *Neoplasia*, vol. 21, pp. 185–196, 2018, [Online]. Available: https://api.semanticscholar.org/CorpusID:57375526
[207] A. Prina-Mello *et al.*, “Culturing substrates influence the morphological, mechanical and biochemical features of lung adenocarcinoma cells cultured in 2D or 3D.,” *Tissue Cell*, vol. 50, pp. 15–30, 2018, [Online]. Available: https://api.semanticscholar.org/CorpusID:46763479
[208] A. Klein, K. Yarbrough, and J. W. Cole, “Stroke, Smoking and Vaping: The No-Good, the Bad and the Ugly.,” *Ann Public Health Res*, vol. 8 1, 2021, [Online]. Available: https://api.semanticscholar.org/CorpusID:232238955
[209] X. Su *et al.*, “FERMT3 mediates cigarette smoke-induced epithelial–mesenchymal transition through Wnt/β-catenin signaling,” *Respir Res*, vol. 22, 2021, [Online]. Available: https://api.semanticscholar.org/CorpusID:237910295
[210] P. Dasgupta *et al.*, “Nicotine induces cell proliferation, invasion and epithelial-mesenchymal transition in a variety of human cancer cell lines,” *Int J Cancer*, vol. 124, 2009, [Online]. Available: https://api.semanticscholar.org/CorpusID:34317118
[211] H. Li *et al.*, “Nicotine Induces Progressive Properties of Lung Adenocarcinoma A549 Cells by Inhibiting Cystic Fibrosis Transmembrane Conductance Regulator (CFTR) Expression and Plasma Membrane Localization,” *Technol Cancer Res Treat*, vol. 17, 2018, [Online]. Available: https://api.semanticscholar.org/CorpusID:54089510
[212] H. Sun and X. Ma, “α5-nAChR modulates nicotine-induced cell migration and invasion in A549 lung cancer cells.,” *Exp Toxicol Pathol*, vol. 67 9, pp. 477–82, 2015, [Online]. Available: https://api.semanticscholar.org/CorpusID:23013216
[213] Z. Qu, F. Sun, J. Zhou, L. Li, S. D. Shapiro, and G. Xiao, “Interleukin-6 Prevents the Initiation but Enhances the Progression of Lung Cancer.,” *Cancer Res*, vol. 75 16, pp. 3209–15, 2015, [Online]. Available: https://api.semanticscholar.org/CorpusID:15055635
[214] A. Dutkowska *et al.*, “Expression of inflammatory interleukins and selected miRNAs in non-small cell lung cancer,” *Sci Rep*, vol. 11, 2021, [Online]. Available: https://api.semanticscholar.org/CorpusID:232111425
[215] H. Lee, J. Lee, S.-H. Hong, I. Rahman, and S.-R. Yang, “Inhibition of RAGE Attenuates Cigarette Smoke-Induced Lung Epithelial Cell Damage via RAGE-Mediated Nrf2/DAMP Signaling,” *Front Pharmacol*, vol. 9, 2018, [Online]. Available: https://api.semanticscholar.org/CorpusID:54524192
[216] T. Sanner and T. K. Grimsrud, “Nicotine: Carcinogenicity and Effects on Response to Cancer Treatment – A Review,” *Front Oncol*, vol. 5, 2015, [Online]. Available: https://api.semanticscholar.org/CorpusID:7011387

[217] J. Pu, J. Shen, Z. Zhong, M. Yanling, and J. Gao, “KANK1 regulates paclitaxel resistance in lung adenocarcinoma A549 cells,” *Artif Cells Nanomed Biotechnol*, vol. 48, pp. 639–647, 2020, [Online]. Available: https://api.semanticscholar.org/CorpusID:211134839
[218] W. Zheng and S. Xu, “Analysis of Differential Expression Proteins of Paclitaxel-Treated Lung Adenocarcinoma Cell A549 Using Tandem Mass Tag-Based Quantitative Proteomics,” *Onco Targets Ther*, vol. 13, pp. 10297–10313, 2020, [Online]. Available: https://api.semanticscholar.org/CorpusID:225076654
[219] H. Gonzalez, C. Hagerling, and Z. Werb, “Roles of the immune system in cancer: from tumor initiation to metastatic progression,” *Genes Dev*, vol. 32, pp. 1267–1284, 2018, [Online]. Available: https://api.semanticscholar.org/CorpusID:52903879
[220] M. De Palma and C. E. Lewis, “Macrophage regulation of tumor responses to anticancer therapies.,” *Cancer Cell*, vol. 23 3, pp. 277–86, 2013, [Online]. Available: https://api.semanticscholar.org/CorpusID:206540619
[221] S. Mun, H. J. Lee, and P. Kim, “Rebuilding the microenvironment of primary tumors in humans: a focus on stroma,” *Exp Mol Med*, vol. 56, no. 3, pp. 527–548, 2024, doi: 10.1038/s12276-024-01191-5.
[222] A. J. Gentles *et al.*, “A human lung tumor microenvironment interactome identifies clinically relevant cell-type cross-talk,” *Genome Biol*, vol. 21, no. 1, p. 107, 2020, doi: 10.1186/s13059-020-02019-x.
[223] M. Kumari, V. Gupta, N. Kumar, and R. K. Arun, “Microfluidics-Based Nanobiosensors for Healthcare Monitoring,” *Mol Biotechnol*, vol. 66, no. 3, pp. 378–401, 2024, doi: 10.1007/s12033-023-00760-9.
[224] J. Song *et al.*, “Microfluidic platform for single cell analysis under dynamic spatial and temporal stimulation,” *Biosens Bioelectron*, vol. 104, pp. 58–64, 2018, doi: https://doi.org/10.1016/j.bios.2017.12.038.
[225] X. Liu, M. H. Maktoomi, M. Alesheikh, P. Heydari, and H. Aghasi, “A 49-63 GHz Phase-locked FMCW Radar Transceiver for High Resolution Applications,” in *ESSCIRC 2023- IEEE 49th European Solid State Circuits Conference (ESSCIRC)*, 2023, pp. 509–512. doi: 10.1109/ESSCIRC59616.2023.10268798.
[226] Q. Yi *et al.*, “All-3D-Printed, Flexible, and Hybrid Wearable Bioelectronic Tactile Sensors Using Biocompatible Nanocomposites for Health Monitoring,” *Adv Mater Technol*, vol. 7, no. 5, 2022, doi: 10.1002/admt.202101034.
[227] A. Mathur *et al.*, “Human iPSC-based Cardiac Microphysiological System For Drug Screening Applications,” *Sci Rep*, vol. 5, 2015, [Online]. Available: https://api.semanticscholar.org/CorpusID:17036125
[228] A. Borók, K. Laboda, and A. Bonyár, “PDMS Bonding Technologies for Microfluidic Applications: A Review,” *Biosensors (Basel)*, vol. 11, 2021, [Online]. Available: https://api.semanticscholar.org/CorpusID:237306135
[229] C. A. Gellner, D. D. Reynaga, and F. M. Leslie, “Cigarette Smoke Extract: A Preclinical Model of Tobacco Dependence,” *Curr Protoc Neurosci*, vol. 77, pp. 9.54.1-9.54.10, 2016, [Online]. Available: https://api.semanticscholar.org/CorpusID:28698784
[230] K. Bjartveit and A. Tverdal, “Health consequences of smoking 1–4 cigarettes per day,” *Tob Control*, vol. 14, pp. 315–320, 2005, [Online]. Available: https://api.semanticscholar.org/CorpusID:22523722